

RESTRICTED CONTRACT REPORT
SCK•CEN-R-5352

**Finite element calculations in respect
of radiation-induced segregation**

SCK•CEN contribution to Perform60 D2-4.3
“Segregation and RIS”

Marc Vankeerberghen

**European Union 7th Framework Program,
Perform60, Grant Agreement N° FP7-232612.**

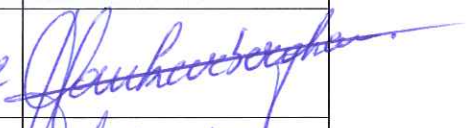
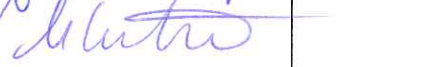
August, 2012

StructuralMaterials SMR
SCK•CEN
Boeretang 200
BE-2400 Mol
Belgium

Belgium

Distribution list

Name	Expert Group	Number
Marc Vankeerberghen	SMR	2
Serguei Gavrilov	SMR	1
Milan Konstantinovic	SMA	1
Marc Scibetta	NMS	1
Secretary	NMS	3
Lorenzo Malerba	SMM	1

		Date	Approval
Author:	Marc Vankeerberghen	20/08/2012	
Verified by:	Milan Konstantinovic	21/08/2012	
Approved by:	Milan Konstantinovic	21/08/2012	

RESTRICTED

All property rights and copyright are reserved. Any communication or reproduction of this document, and any communication or use of its content without explicit authorization is prohibited. Any infringement to this rule is illegal and entitles to claim damages from the infringer, without prejudice to any other right in case of granting a patent or registration in the field of intellectual property.

SCK•CEN, Studiecentrum voor Kernenergie/Centre d'Etude de l'Energie Nucléaire
 Stichting van Openbaar Nut – Fondation d'Utilité Publique - Foundation of Public Utility
 Registered Office: Avenue Herrmann Debroux 40 – BE-1160 BRUSSEL
 Operational Office: Boeretang 200 – BE-2400 MOL

Finite element calculations in respect of radiation-induced segregation

SCK•CEN contribution to Perform60 D2-4.3
“Segregation and RIS”

Marc Vankeerberghen

**European Union 7th Framework Program,
Perform60, Grant Agreement N° FP7-232612.**

August, 2012
Status: Confidential

StructuralMaterials SMR
SCK•CEN
Boeretang 200
BE-2400 Mol
Belgium

Abstract

Radiation-induced segregation to internal and external surfaces plays an important role in many technological phenomena such as void swelling, phase stability and embrittlement. In particular the change in grain boundary chemistry arising from major element segregation during irradiation may affect both the failure and corrosion behaviour. Segregation occurs when the flux of specific alloying elements are preferentially coupled to a persistent flux of point defects which is set up, inter alia, by irradiation or film growth.

A mathematical model description is given for the Perks and Modified Inverse Kirkendall models for radiation induced segregation. The models were successfully implemented in Comsol Multiphysics.

Trend calculations have been performed with the Perks and Modified Inverse Kirkendall models. The influence of mesh size, alloy composition, temperature, dislocation density and flux on grain boundary segregation has been investigated.

Additionally a comparison with literature published radiation-induced segregation data was attempted. Hitherto, post-processing features were added to the Comsol Multiphysics models for comparison with AES and STEM obtained results. The comparison shows that trends of radiation induced segregation with temperature and dpa are relatively well predicted and that the predictions seem to be better with the as-published Perks- than with the as-published MIK-model.

The results have been obtained with a reduced set of coupled partial differentials equations by eliminating the equation for iron on the basis that elemental fractions must add up to one. This made the calculations more stable.

Two-dimensional calculations of radiation-induced segregation are shown and were verified to be in agreement with the one-dimensional calculations.

Table of contents

1	Introduction	3
2	The Perks and MIK models.....	4
2.1	Introduction.....	4
2.2	Transport equations.....	4
2.2.1	Concentrations and fractional concentrations.....	4
2.2.2	Continuity equations.....	4
2.2.3	Atom and defect flux equations.....	4
2.2.4	Atom and defect diffusion coefficients and diffusivities	5
2.3	Diffusivities and jump frequencies	6
2.3.1	Perks model	6
2.3.2	MIK model	7
2.4	Defect production rates	8
2.5	Boundary conditions	8
2.5.1	Grain boundary	8
2.5.2	Centre of grain	8
2.6	Matrix notation	9
2.7	Calculation results.....	10
2.7.1	Perks model - data	10
2.7.2	Perks model - results	11
2.7.3	MIK model - data	17
2.7.4	MIK model - results.....	18
2.7.5	Comparison Perks and MIK results.....	24
3	Trend calculations.....	33
3.1	Mesh size dependence	33
3.1.1	Concentration exactly at the grain boundary	33
3.1.2	Averaged concentration at the grain boundary.....	36
3.1.3	Conclusion in respect of grain boundary mesh size	37
3.2	The effect of temperature on grain boundary segregation	38
3.3	The effect of alloy composition on grain boundary segregation	43
3.4	The effect of dislocation density on grain boundary segregation	46
3.5	The effect of neutron flux on grain boundary segregation	50
4	Comparison with literature	55
4.1	Comparison with STEM measurements	55
4.2	Comparison with AES measurements	56
4.3	Comparison with experimental data	57
4.4	Conclusion on literature comparison	68
5	Two-dimensional calculations with the Perks model	69
5.1	The 1D Perks model	69
5.2	The 1D reduced Perks model.....	70
5.3	The 2D reduced Perks model.....	70
5.4	Results with the 2D reduced Perks model	71
6	Conclusions	76
7	Nomenclature.....	77
9	Acknowledgements	78
10	References	78

1 Introduction

Radiation-induced segregation to internal and external surfaces plays an important role in many technological phenomena such as void swelling, phase stability and embrittlement. In particular the change in grain boundary chemistry arising from major element segregation during irradiation may affect both the failure and corrosion behaviour [2].

Segregation occurs when the flux of specific alloying elements are preferentially coupled to a persistent flux of point defects which is set up, inter alia, by irradiation or film growth. First, a mathematical model description will be given for the Perks and the Modified Inverse Kirkendall (MIK) models for radiation induced segregation. This includes matrix derivations for implementation into a finite element code, Comsol Multiphysics. Then, trend calculations are made and discussed. Subsequently, a comparison of calculated and measured grain boundary fractions is made and discussed. Finally the results of a two-dimensional implementation are shown.

2 The Perks and MIK models

2.1 Introduction

The Perks and Modified Inverse Kirkendall models [1-4] for radiation-induced segregation assume that segregation occurs due to preferential atom interchanges with vacancies via the inverse Kirkendall effect, that interstitial jumps are independent of the atom species and that no binding is allowed. Also excluded from the model is the effect of the migration of bound clusters of atoms and point defects.

Net atom migration occurs in point defect concentration gradients when the vacancy-atom exchange frequency differs for each alloying component so that the atomic migration rate away from the sink varies for each element. Since the vacancy flux is set up towards a sink (e.g. a grain boundary) it is expected that the slowest diffusing species will accumulate at the sink while the fastest diffusing species will be depleted.

The models calculate the concentrations of major elements by considering the fluxes of each species caused by the migration of point defects created thermally and by irradiation. Point defect losses occur due to mutual recombination and annihilation at fixed sinks, the boundary surfaces and a uniform and time independent distribution of dislocations.

2.2 Transport equations

2.2.1 Concentrations and fractional concentrations

$$C_{Fe} = N \cdot X_{Fe} \quad \text{or} \quad X_{Fe} = \Omega \cdot C_{Fe} \quad (1)$$

$$C_{Cr} = N \cdot X_{Cr} \quad \text{or} \quad X_{Cr} = \Omega \cdot C_{Cr} \quad (2)$$

$$C_{Ni} = N \cdot X_{Ni} \quad \text{or} \quad X_{Ni} = \Omega \cdot C_{Ni} \quad (3)$$

2.2.2 Continuity equations

$$\frac{dC_{Fe}}{dt} = -\nabla J_{Fe} \quad \frac{dX_{Fe}}{dt} = -\Omega \cdot \nabla J_{Fe} \quad (4)$$

$$\frac{dC_{Cr}}{dt} = -\nabla J_{Cr} \quad \frac{dX_{Cr}}{dt} = -\Omega \cdot \nabla J_{Cr} \quad (5)$$

$$\frac{dC_{Ni}}{dt} = -\nabla J_{Ni} \quad \frac{dX_{Ni}}{dt} = -\Omega \cdot \nabla J_{Ni} \quad (6)$$

$$\frac{dC_v}{dt} = -\nabla J_v + N \cdot G_v - R \cdot \Omega \cdot C_v C_i \quad \frac{dX_v}{dt} = -\Omega \cdot \nabla J_v + G_v - R \cdot X_v X_i \quad (7)$$

$$\frac{dC_i}{dt} = -\nabla J_i + N \cdot G_i - R \cdot \Omega \cdot C_v C_i \quad \frac{dX_i}{dt} = -\Omega \cdot \nabla J_i + G_i - R \cdot X_v X_i \quad (8)$$

2.2.3 Atom and defect flux equations

$$J_{Fe}^* = -\alpha D_{Fe} \nabla C_{Fe} + \Omega \cdot C_{Fe} (d_{Fe}^v \nabla C_v - d_{Fe}^i \nabla C_i) \\ \text{or} \quad \Omega \cdot J_{Fe}^* = -\alpha D_{Fe} \nabla X_{Fe} + X_{Fe} (d_{Fe}^v \nabla X_v - d_{Fe}^i \nabla X_i) \quad (9)$$

$$J_{Cr}^* = -\alpha D_{Cr} \nabla C_{Cr} + \Omega \cdot C_{Cr} (d_{Cr}^v \nabla C_v - d_{Cr}^i \nabla C_i) \\ \text{or} \quad \Omega \cdot J_{Cr}^* = -\alpha D_{Cr} \nabla X_{Cr} + X_{Cr} (d_{Cr}^v \nabla X_v - d_{Cr}^i \nabla X_i) \quad (10)$$

$$J_{Ni}^* = -\alpha D_{Ni} \nabla C_{Ni} + \Omega \cdot C_{Ni} (d_{Ni}^v \nabla C_v - d_{Ni}^i \nabla C_i) \\ \text{or} \quad \Omega \cdot J_{Ni}^* = -\alpha D_{Ni} \nabla X_{Ni} + X_{Ni} (d_{Ni}^v \nabla X_v - d_{Ni}^i \nabla X_i) \quad (11)$$

$$J_v = -D_v \nabla C_v + \alpha \cdot \Omega \cdot C_v (d_{Fe}^v \nabla C_{Fe} + d_{Cr}^v \nabla C_{Cr} + d_{Ni}^v \nabla C_{Ni})$$

or $\Omega \cdot J_v = -D_v \nabla X_v + \alpha \cdot X_v (d_{Fe}^v \nabla X_{Fe} + d_{Cr}^v \nabla X_{Cr} + d_{Ni}^v \nabla X_{Ni})$ (12)

$$J_i = -D_i \nabla C_i - \alpha \cdot \Omega \cdot C_i (d_{Fe}^i \nabla C_{Fe} + d_{Cr}^i \nabla C_{Cr} + d_{Ni}^i \nabla C_{Ni})$$

or $\Omega \cdot J_i = -D_i \nabla X_i - \alpha \cdot X_i (d_{Fe}^i \nabla X_{Fe} + d_{Cr}^i \nabla X_{Cr} + d_{Ni}^i \nabla X_{Ni})$ (13)

$$J_{Fe} = J_{Fe}^* - (J_i - J_v) X_{Fe}$$

$$J_{Cr} = J_{Cr}^* - (J_i - J_v) X_{Cr}$$

$$J_{Ni} = J_{Ni}^* - (J_i - J_v) X_{Ni}$$

yielding

$$\Omega \cdot J_{Fe} = -\alpha D_{Fe} (1 - X_{Fe}) \nabla X_{Fe}$$

$+ [\alpha D_{Cr} \nabla X_{Cr} + \alpha D_{Ni} \nabla X_{Ni} + (d_{Fe}^v - D_v) \nabla X_v + (D_i - d_{Fe}^i) \nabla X_i] X_{Fe}$ (14)

$$\Omega \cdot J_{Cr} = -\alpha D_{Cr} (1 - X_{Cr}) \nabla X_{Cr}$$

$+ [\alpha D_{Fe} \nabla X_{Fe} + \alpha D_{Ni} \nabla X_{Ni} + (d_{Cr}^v - D_v) \nabla X_v + (D_i - d_{Cr}^i) \nabla X_i] X_{Cr}$ (15)

$$\Omega \cdot J_{Ni} = -\alpha D_{Ni} (1 - X_{Ni}) \nabla X_{Ni}$$

$+ [\alpha D_{Cr} \nabla X_{Cr} + \alpha D_{Fe} \nabla X_{Fe} + (d_{Ni}^v - D_v) \nabla X_v + (D_i - d_{Ni}^i) \nabla X_i] X_{Ni}$ (16)

2.2.4 Atom and defect diffusion coefficients and diffusivities

$$D_{Fe} = d_{Fe}^v X_v + d_{Fe}^i X_i$$
 (17)

$$D_{Cr} = d_{Cr}^v X_v + d_{Cr}^i X_i$$
 (18)

$$D_{Ni} = d_{Ni}^v X_v + d_{Ni}^i X_i$$
 (19)

$$D_v = d_{Fe}^v X_{Fe} + d_{Cr}^v X_{Cr} + d_{Ni}^v X_{Ni}$$
 (20)

$$D_i = d_{Fe}^i X_{Fe} + d_{Cr}^i X_{Cr} + d_{Ni}^i X_{Ni}$$
 (21)

2.3 Diffusivities and jump frequencies

$$d_{Fe}^v = \nu_{Fe}^v (\lambda_a^v)^2 = d_{Fe}^{v,0} \exp\left(-\frac{E_{Fe}^{v,m}}{k_b T}\right) \quad \lambda_a^v = \lambda \quad (22)$$

$$d_{Cr}^v = \nu_{Cr}^v (\lambda_a^v)^2 = d_{Cr}^{v,0} \exp\left(-\frac{E_{Cr}^{v,m}}{k_b T}\right) \quad (23)$$

$$d_{Ni}^v = \nu_{Ni}^v (\lambda_a^v)^2 = d_{Ni}^{v,0} \exp\left(-\frac{E_{Ni}^{v,m}}{k_b T}\right) \quad (24)$$

$$d_{Fe}^i = \nu_{Fe}^i (\lambda_a^i)^2 = d_{Fe}^{i,0} \exp\left(-\frac{E_{Fe}^{i,m}}{k_b T}\right) \quad \lambda_a^i = \sqrt{\frac{2}{3}}\lambda \quad (25)$$

$$d_{Cr}^i = \nu_{Cr}^i (\lambda_a^i)^2 = d_{Cr}^{i,0} \exp\left(-\frac{E_{Cr}^{i,m}}{k_b T}\right) \quad (26)$$

$$d_{Ni}^i = \nu_{Ni}^i (\lambda_a^i)^2 = d_{Ni}^{i,0} \exp\left(-\frac{E_{Ni}^{i,m}}{k_b T}\right) \quad (27)$$

2.3.1 Perks model

$$\nu_{Fe}^v = f_{Fe}^v \cdot \nu_{Fe}^{v,0} \exp\left(-\frac{E_{Fe}^{v,m}}{k_b T}\right) \quad d_{Fe}^{v,0} = (\lambda_a^v)^2 \cdot f_{Fe}^v \cdot \nu_{Fe}^{v,0} \quad (28)$$

$$\nu_{Cr}^v = f_{Cr}^v \cdot \nu_{Cr}^{v,0} \exp\left(-\frac{E_{Cr}^{v,m}}{k_b T}\right) \quad d_{Cr}^{v,0} = (\lambda_a^v)^2 \cdot f_{Cr}^v \cdot \nu_{Cr}^{v,0} \quad (29)$$

$$\nu_{Ni}^v = f_{Ni}^v \cdot \nu_{Ni}^{v,0} \exp\left(-\frac{E_{Ni}^{v,m}}{k_b T}\right) \quad d_{Ni}^{v,0} = (\lambda_a^v)^2 \cdot f_{Ni}^v \cdot \nu_{Ni}^{v,0} \quad (30)$$

$$\nu_{Fe}^i = f^i \cdot \nu^{i,0} \exp\left(-\frac{E_{Fe}^{i,m}}{k_b T}\right) \quad d_{Fe}^{i,0} = (\lambda_a^i)^2 \cdot f^i \cdot \nu^{i,0} \quad (31)$$

$$\nu_{Cr}^i = f^i \cdot \nu^{i,0} \exp\left(-\frac{E_{Cr}^{i,m}}{k_b T}\right) \quad d_{Cr}^{i,0} = (\lambda_a^i)^2 \cdot f^i \cdot \nu^{i,0} \quad (32)$$

$$\nu_{Ni}^i = f^i \cdot \nu^{i,0} \exp\left(-\frac{E_{Ni}^{i,m}}{k_b T}\right) \quad d_{Ni}^{i,0} = (\lambda_a^i)^2 \cdot f^i \cdot \nu^{i,0} \quad (33)$$

2.3.2 MIK model

$$\nu_{Fe}^v = \nu_{Fe}^{v,0} \exp\left(-\frac{E_{Fe}^{v,m}}{k_b T}\right) \quad d_{Fe}^{v,0} = (\lambda_a^v)^2 \cdot \nu_{Fe}^{v,0} \quad (34)$$

$$\nu_{Cr}^v = \nu_{Cr}^{v,0} \exp\left(-\frac{E_{Cr}^{v,m}}{k_b T}\right) \quad d_{Cr}^{v,0} = (\lambda_a^v)^2 \cdot \nu_{Cr}^{v,0} \quad (35)$$

$$\nu_{Ni}^v = \nu_{Ni}^{v,0} \exp\left(-\frac{E_{Ni}^{v,m}}{k_b T}\right) \quad d_{Ni}^{v,0} = (\lambda_a^v)^2 \cdot \nu_{Ni}^{v,0} \quad (36)$$

$$\nu_{Fe}^i = f^i \cdot \nu^{i,0} \exp\left(-\frac{E_{Fe}^{i,m}}{k_b T}\right) \quad d_{Fe}^{i,0} = (\lambda_a^i)^2 \cdot f^i \cdot \nu^{i,0} \quad (37)$$

$$\nu_{Cr}^i = f^i \cdot \nu^{i,0} \exp\left(-\frac{E_{Cr}^{i,m}}{k_b T}\right) \quad d_{Cr}^{i,0} = (\lambda_a^i)^2 \cdot f^i \cdot \nu^{i,0} \quad (38)$$

$$\nu_{Ni}^i = f^i \cdot \nu^{i,0} \exp\left(-\frac{E_{Ni}^{i,m}}{k_b T}\right) \quad d_{Ni}^{i,0} = (\lambda_a^i)^2 \cdot f^i \cdot \nu^{i,0} \quad (39)$$

where

$$\begin{aligned} E_{Fe}^{v,m} &= C_{Fe} \left(-\frac{3}{2} E_{Fe}^{coh} + \frac{1}{2} E_{Fe,pure}^{v,m} - \frac{1}{2} E_{Fe}^{v,f} \right) + \\ &\quad C_{Cr} \left(-E_{Fe}^{coh} - \frac{1}{2} E_{Cr}^{coh} + \frac{1}{2} E_{Cr,pure}^{v,m} - \frac{1}{2} E_{Cr}^{v,f} - ZE_{FeCr}^{ord} \right) + \\ &\quad C_{Ni} \left(-E_{Fe}^{coh} - \frac{1}{2} E_{Ni}^{coh} + \frac{1}{2} E_{Ni,pure}^{v,m} - \frac{1}{2} E_{Ni}^{v,f} - ZE_{NiFe}^{ord} \right) + \\ &\quad C_v \left(-E_{Fe}^{coh} - E_{Fe}^{v,f} \right) + \left(\frac{3}{2} E_{Fe}^{coh} + \frac{1}{2} E_{Fe,pure}^{v,m} + \frac{1}{2} E_{Fe}^{v,f} \right) \end{aligned} \quad (40)$$

$$\begin{aligned} E_{Cr}^{v,m} &= C_{Cr} \left(-\frac{3}{2} E_{Cr}^{coh} + \frac{1}{2} E_{Cr,pure}^{v,m} - \frac{1}{2} E_{Cr}^{v,f} \right) + \\ &\quad C_{Fe} \left(-E_{Cr}^{coh} - \frac{1}{2} E_{Fe}^{coh} + \frac{1}{2} E_{Fe,pure}^{v,m} - \frac{1}{2} E_{Fe}^{v,f} - ZE_{FeCr}^{ord} \right) + \\ &\quad C_{Ni} \left(-E_{Cr}^{coh} - \frac{1}{2} E_{Ni}^{coh} + \frac{1}{2} E_{Ni,pure}^{v,m} - \frac{1}{2} E_{Ni}^{v,f} - ZE_{NiCr}^{ord} \right) + \\ &\quad C_v \left(-E_{Cr}^{coh} - E_{Cr}^{v,f} \right) + \left(\frac{3}{2} E_{Cr}^{coh} + \frac{1}{2} E_{Cr,pure}^{v,m} + \frac{1}{2} E_{Cr}^{v,f} \right) \end{aligned} \quad (41)$$

$$\begin{aligned} E_{Ni}^{v,m} &= C_{Ni} \left(-\frac{3}{2} E_{Ni}^{coh} + \frac{1}{2} E_{Ni,pure}^{v,m} - \frac{1}{2} E_{Ni}^{v,f} \right) + \\ &\quad C_{Fe} \left(-E_{Ni}^{coh} - \frac{1}{2} E_{Fe}^{coh} + \frac{1}{2} E_{Fe,pure}^{v,m} - \frac{1}{2} E_{Fe}^{v,f} - ZE_{FeNi}^{ord} \right) + \\ &\quad C_{Cr} \left(-E_{Ni}^{coh} - \frac{1}{2} E_{Cr}^{coh} + \frac{1}{2} E_{Cr,pure}^{v,m} - \frac{1}{2} E_{Cr}^{v,f} - ZE_{NiCr}^{ord} \right) + \\ &\quad C_v \left(-E_{Ni}^{coh} - E_{Ni}^{v,f} \right) + \left(\frac{3}{2} E_{Ni}^{coh} + \frac{1}{2} E_{Ni,pure}^{v,m} + \frac{1}{2} E_{Ni}^{v,f} \right) \end{aligned} \quad (42)$$

and

$$E_{Fe}^{coh} = E_{Fe,pure}^{coh} + \Delta G_{Fe}^{bcc \rightarrow fcc} \quad (43)$$

$$E_{Cr}^{coh} = E_{Cr,pure}^{coh} + \Delta G_{Cr}^{bcc \rightarrow fcc} \quad (44)$$

2.4 Defect production rates

$$G_v = \eta\phi + \rho D_v (X_v^{th} - X_v) \quad X_v^{th} = \exp\left(\frac{S^{v,f}}{k_b}\right) \exp\left(-\frac{E^{v,f}}{k_b T}\right) \quad (45)$$

$$G_i = \eta\phi + \rho D_i (X_i^{th} - X_i) \quad X_i^{th} = small \quad (46)$$

$$R = \left[(\nu_{Fe}^v + \nu_{Fe}^i) X_{Fe} + (\nu_{Cr}^v + \nu_{Cr}^i) X_{Cr} + (\nu_{Ni}^v + \nu_{Ni}^i) X_{Ni} \right] Z \quad (47)$$

2.5 Boundary conditions

2.5.1 Grain boundary

- Absorbing boundary for point defects. Perfect sink → defect concentrations remain at thermal equilibrium

$$\text{interstitials } X_i = X_i^{th} \quad (48)$$

$$\text{vacancies } X_v = X_v^{th} \quad (49)$$

- Atomic fluxes ?

$$J_{Fe} = J_{Cr} = J_{Ni} = 0 \quad \text{Perks \& MIK model} \quad (50)$$

2.5.2 Centre of grain

- Symmetry boundary condition

2.6 Matrix notation

$$\{X\}_{5x1} = \begin{bmatrix} X_{Fe} \\ X_{Cr} \\ X_{Ni} \\ X_v \\ X_i \end{bmatrix} \quad \{J\}_{5x1} = \Omega \begin{bmatrix} J_{Fe} \\ J_{Cr} \\ J_{Ni} \\ J_v \\ J_i \end{bmatrix} \quad [X]_{5x1} = \begin{bmatrix} X_{Fe} & 0 & 0 & 0 & 0 \\ 0 & X_{Cr} & 0 & 0 & 0 \\ 0 & 0 & X_{Ni} & 0 & 0 \\ 0 & 0 & 0 & X_v & 0 \\ 0 & 0 & 0 & 0 & X_i \end{bmatrix} \quad (51)$$

$$\frac{d\{X\}_{5x1}}{dt} = -\nabla\{J\}_{5x1} + \{S\}_{5x1} \quad (52)$$

$$\{J\}_{5x1} = (-[A]_{5x5} + [X]_{5x5}[B]_{5x5})\nabla\{X\}_{5x1} \quad (53)$$

$$[A]_{5x5} = \begin{bmatrix} \alpha D_{Fe} & 0 & 0 & 0 & 0 \\ 0 & \alpha D_{Cr} & 0 & 0 & 0 \\ 0 & 0 & \alpha D_{Ni} & 0 & 0 \\ 0 & 0 & 0 & D_v & 0 \\ 0 & 0 & 0 & 0 & D_i \end{bmatrix} \quad (54)$$

$$[B]_{5x5} = \begin{bmatrix} \alpha D_{Fe} & \alpha D_{Cr} & \alpha D_{Ni} & -D_v + d_{Fe}^v & D_i - d_{Fe}^i \\ \alpha D_{Fe} & \alpha D_{Cr} & \alpha D_{Ni} & -D_v + d_{Cr}^v & D_i - d_{Cr}^i \\ \alpha D_{Fe} & \alpha D_{Cr} & \alpha D_{Ni} & -D_v + d_{Ni}^v & D_i - d_{Ni}^i \\ \alpha d_{Fe}^v & \alpha d_{Cr}^v & \alpha d_{Ni}^v & 0 & 0 \\ -\alpha d_{Fe}^i & -\alpha d_{Cr}^i & -\alpha d_{Ni}^i & 0 & 0 \end{bmatrix} \quad (55)$$

$$\{S\}_{5x1} = \begin{bmatrix} 0 \\ 0 \\ 0 \\ G_v - RX_v X_i \\ G_i - RX_v X_i \end{bmatrix} \quad (56)$$

2.7 Calculation results

2.7.1 Perks model - data

Input parameter	Notation	Value	Ref.
Standard vacancy jump frequency for Fe	$v_{Fe}^{v,0}$	$2.8 \cdot 10^{13} /s$	1
Standard vacancy jump frequency for Cr	$v_{Cr}^{v,0}$	$5.0 \cdot 10^{13} /s$	1
Standard vacancy jump frequency for Ni	$v_{Ni}^{v,0}$	$1.5 \cdot 10^{13} /s$	1
Fe-vacancy correlation factor	f_{Fe}^v	0.785	1
Cr-vacancy correlation factor	f_{Cr}^v	0.668	1
Ni-vacancy correlation factor	f_{Ni}^v	0.872	1
Vacancy migration energy for Fe	$E_{Fe}^{v,m}$	1.3 eV	1
Vacancy migration energy for Cr	$E_{Cr}^{v,m}$	1.3 eV	1
Vacancy migration energy for Ni	$E_{Ni}^{v,m}$	1.3 eV	1
Standard interstitial jump frequency	$v^{i,0}$	$1.5 \cdot 10^{12} /s$	1
Interstitial correlation factor	f^i	0.44	1
Interstitial migration energy	$E^{i,m}$	0.9 eV	1
Vacancy formation energy	$E^{v,f}$	1.9 eV	1
Vacancy formation entropy	$S^{v,f}$	$2*k_b$	
Dislocation density	ρ	$1 \cdot 10^{14} \#/m^2$	1
Number of recombination volume	Z	12	FCC lattice
Unit cell size	λ	$3.5 \cdot 10^{-10} m$	1
Atomic density	N	$9.1 \cdot 10^{28} \#/m^3$	
Flux	Φ	$7 \cdot 10^{-6} dpa/s$	1
Damage efficiency	η	0.1 /dpa	1
Thermodynamic factor	α	1	1
Temperature	T	300°C	

Table 1 Inputs to the Perks model.

2.7.2 Perks model - results

The Perks model documented in 2 has been implemented in Comsol Multiphysics using the data shown in Table 1. A grain of radius 1 μm has been analysed. It is assumed that this geometry can be treated as one-dimensional. Figure 1 to Figure 8 show the results of the calculation. An x-coordinate of 0 corresponds to the centre of the grain and a x-coordinate of 1×10^{-6} to the grain boundary. Figure 1 to Figure 5 respectively show the iron, chromium, nickel, vacancy and interstitial concentration fraction profiles across the grain. The profiles are shown for four different times 1×10^5 , 1×10^6 , 1×10^7 and 1×10^8 seconds which, at a flux of 7×10^{-6} dpa/s, respectively correspond to 0.7, 7, 70 and, oops, 700 dpa. Note that chromium is depleted at the grain boundary but shows a slight enrichment close to the grain boundary in order to keep the total number of chromium atoms in the grain constant. Similarly, as nickel is enriched at the grain boundary there is a slight depletion close to the grain boundary in order to keep the total number of nickel atoms in the grain constant. Figure 6 to Figure 8 respectively show the time evolution for the iron, chromium and nickel concentration at the grain boundary; the top figure shows the evolution against time, the bottom figure against the logarithm of time. As time goes on and dpa is accumulated chromium is depleted and nickel enriched at the grain boundary. Iron is first enriched but as chromium becomes depleted iron takes over the role of chromium and starts depleting. Later it will be shown that these grain boundary concentration fractions cannot be immediately compared to measured grain boundary concentration fractions.

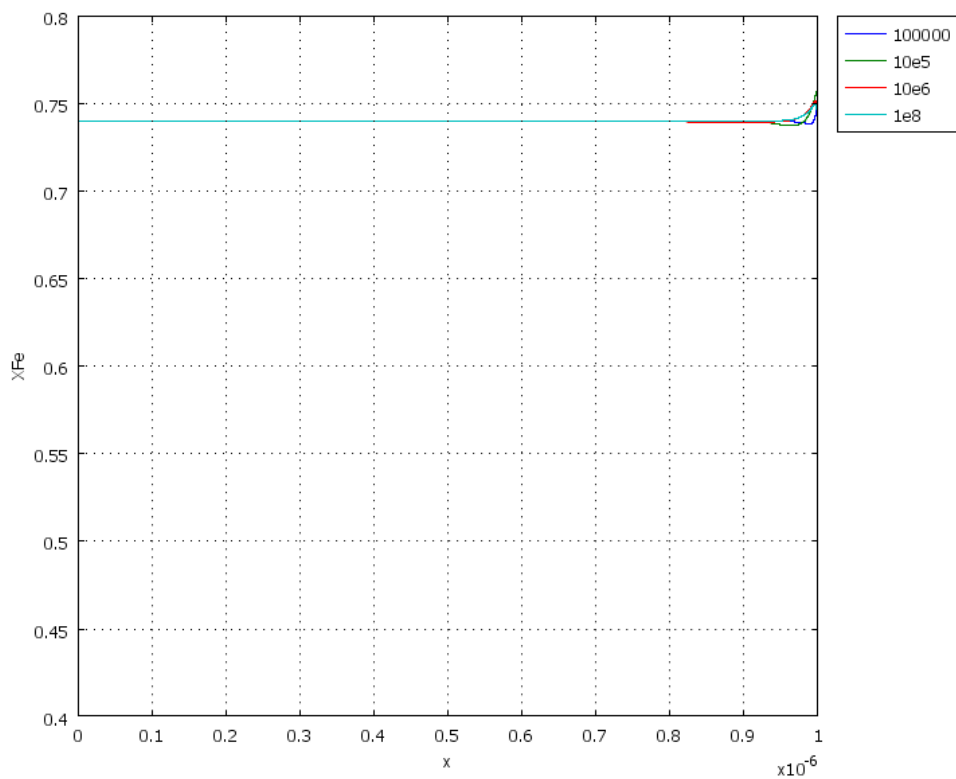


Figure 1 Iron concentration fraction across the grain at different times (seconds). Perks model. Data of Table 1.

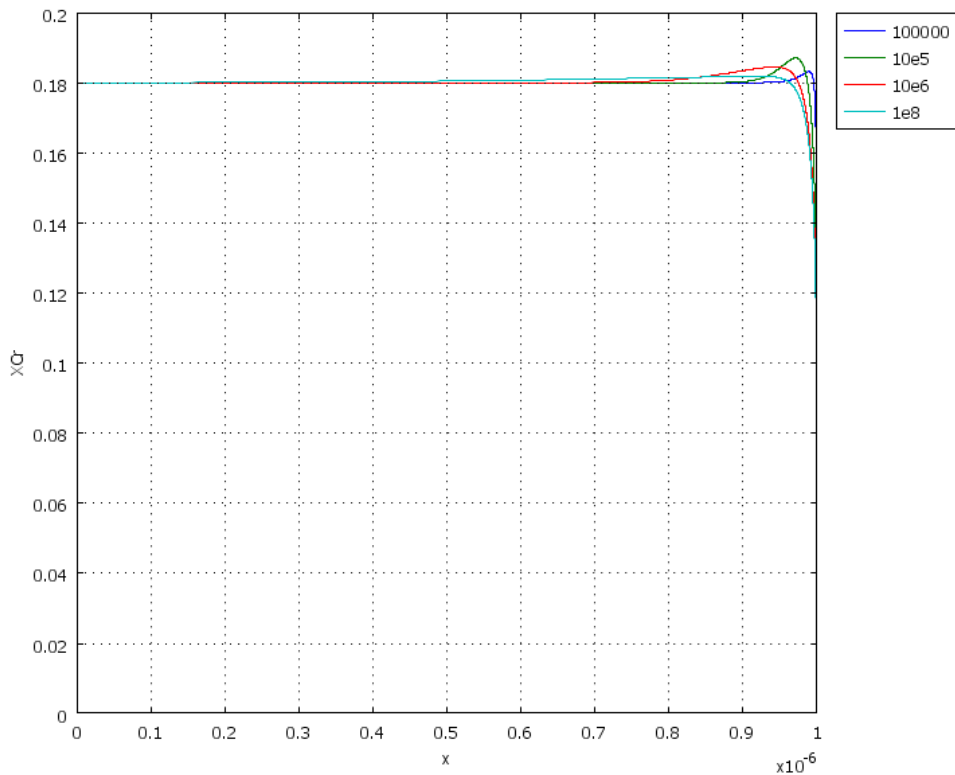


Figure 2 Chromium concentration fraction across the grain at different times (seconds). Perks model. Data of Table 1.

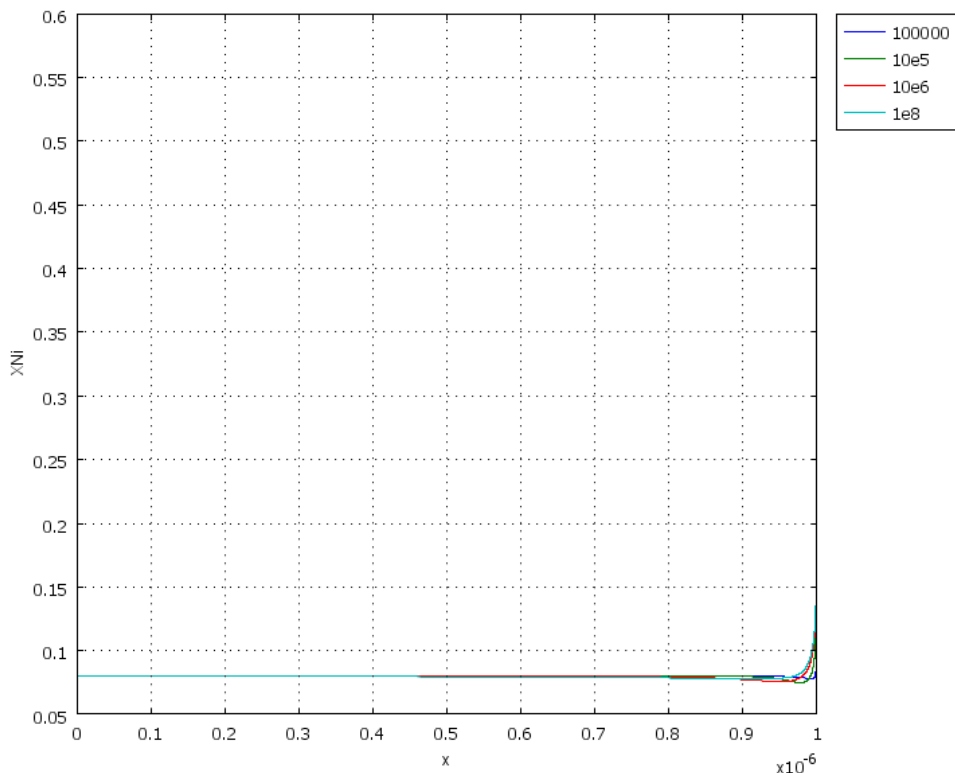


Figure 3 Nickel concentration fraction across the grain at different times (seconds). Perks model. Data of Table 1.

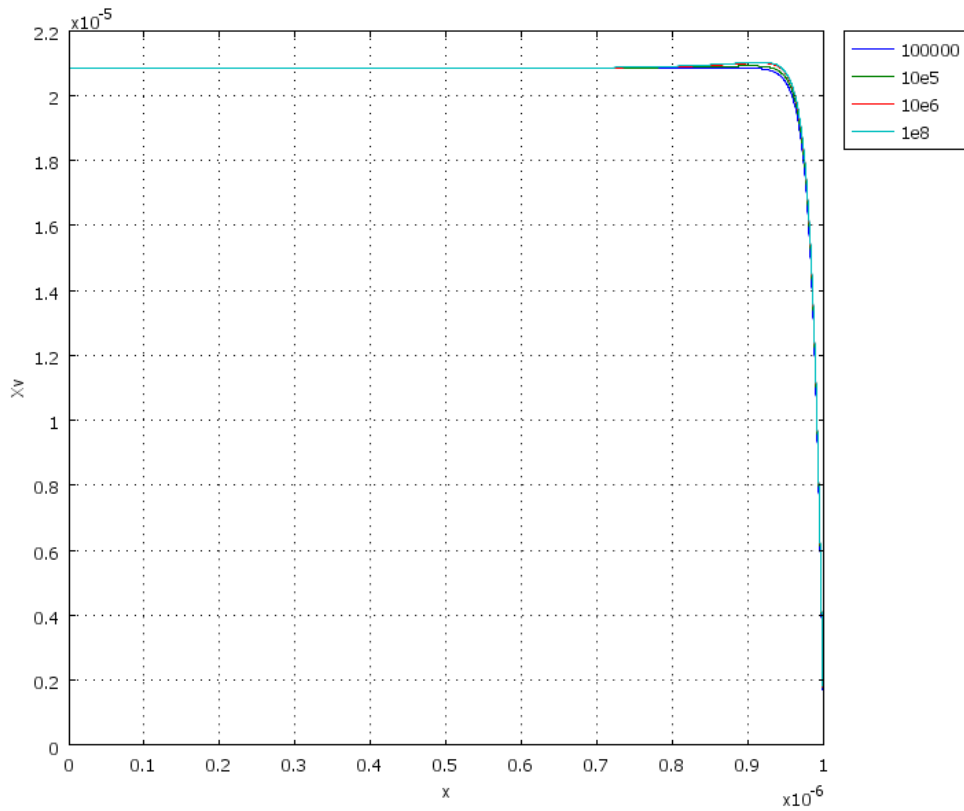


Figure 4 Vacancy concentration fraction across the grain at different times (seconds). Perks model. Data of Table 1.

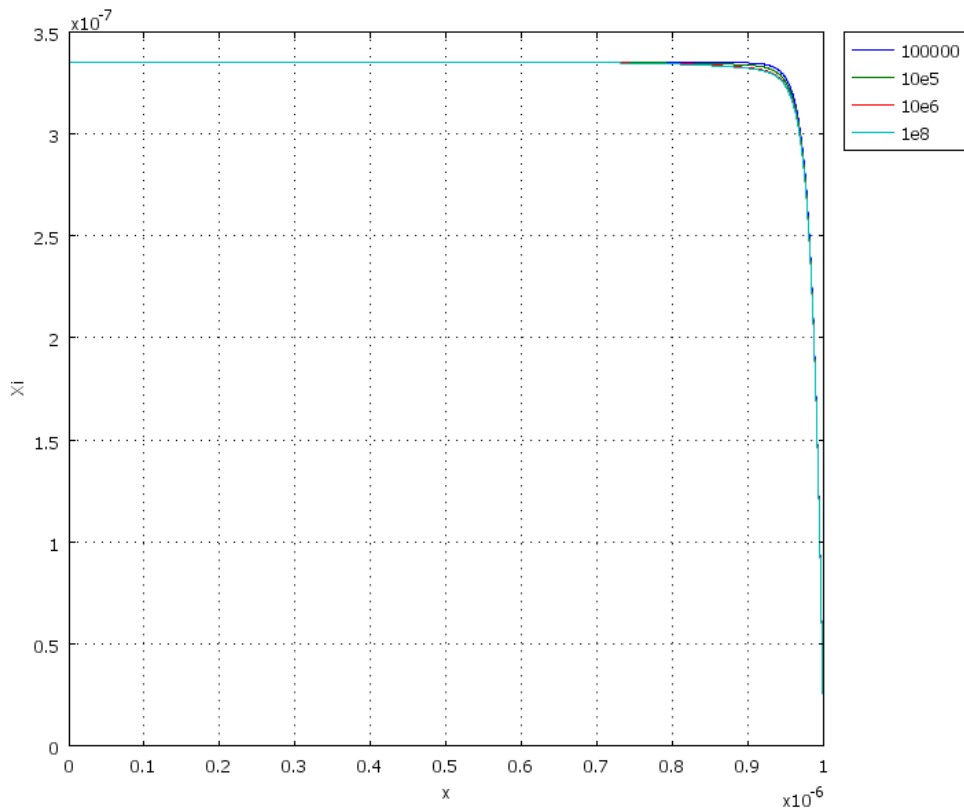


Figure 5 Interstitial concentration fraction across the grain at different times (seconds). Perks model. Data of Table 1.

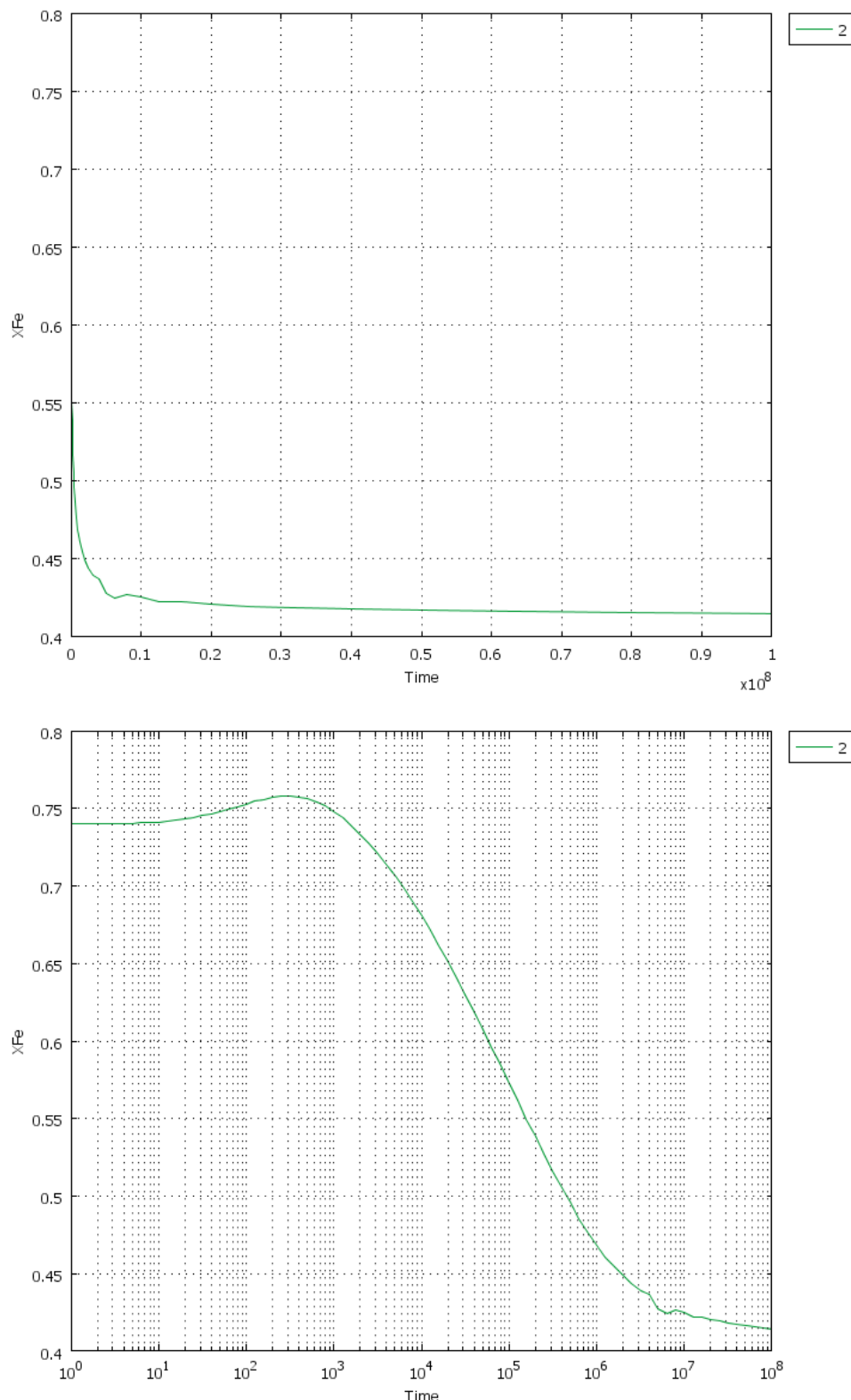


Figure 6 Time evolution of the iron concentration fraction at the grain boundary. Perks model. Data of Table 1.

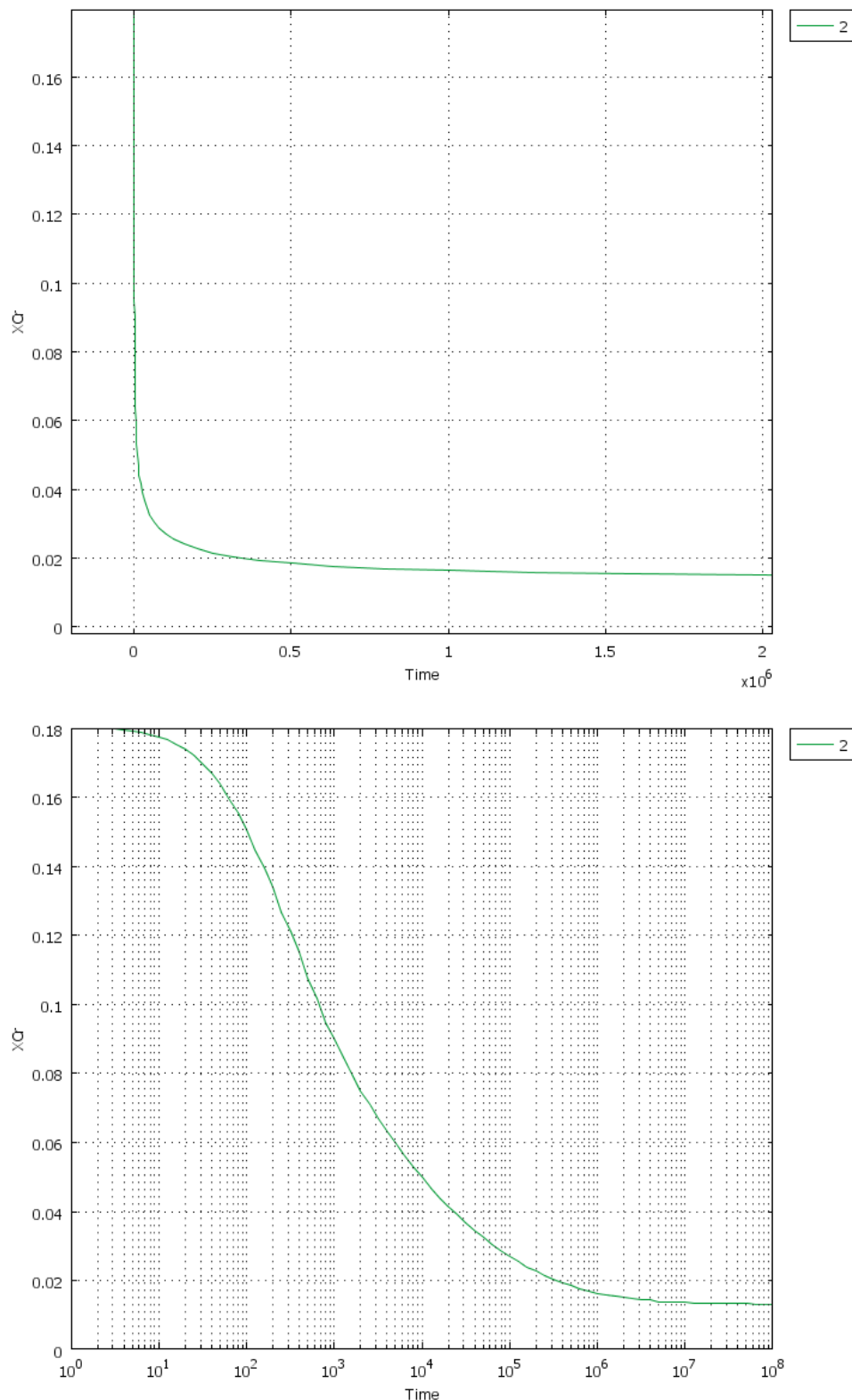


Figure 7 Time evolution of the chromium concentration fraction at the grain boundary. Perks model. Data of Table 1.

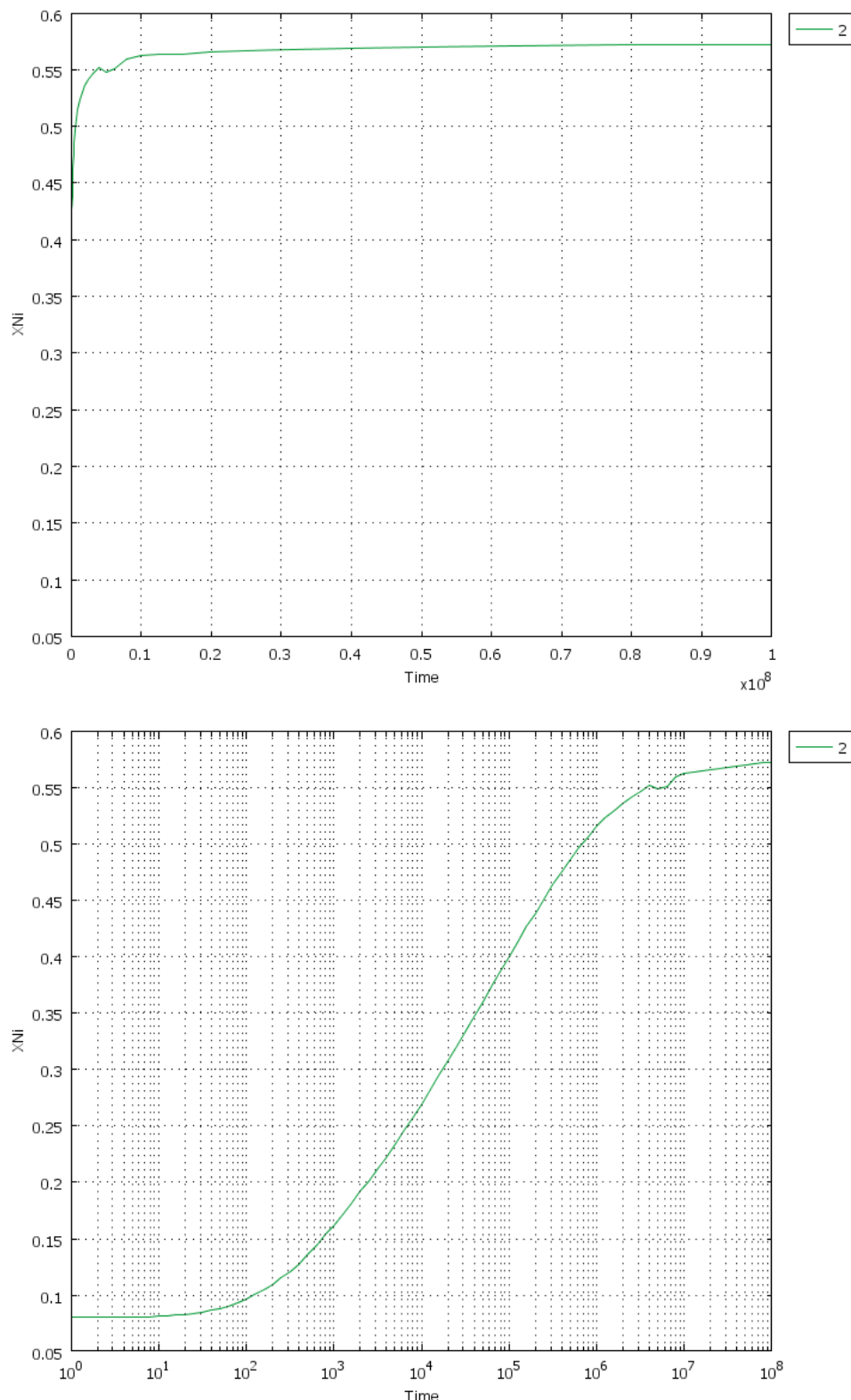


Figure 8 Time evolution of the nickel concentration fraction at the grain boundary. Perks model. Data of Table 1.

2.7.3 MIK model - data

Input parameter	Notation	Value	Ref.
Standard vacancy jump frequency for Fe	$\nu_{Fe}^{v,0}$	$1.6 \cdot 10^{13} /s$	4
Standard vacancy jump frequency for Cr	$\nu_{Cr}^{v,0}$	$2.4 \cdot 10^{13} /s$	4
Standard vacancy jump frequency for Ni	$\nu_{Ni}^{v,0}$	$1.0 \cdot 10^{13} /s$	4
Cohesive energy for pure Fe	E_{Fe}^{coh}	-4.28 eV	4
Cohesive energy for pure Cr	E_{Cr}^{coh}	-4.10 eV	4
Cohesive energy for pure Ni	E_{Ni}^{coh}	-4.44 eV	4
Vacancy migration energy for pure Fe	$E_{Fe,pure}^{v,m}$	1.28 eV	4
Vacancy migration energy for pure Cr	$E_{Cr,pure}^{v,m}$	0.97 eV	4
Vacancy migration energy for pure Ni	$E_{Ni,pure}^{v,m}$	1.04 eV	4
Vacancy formation energy of pure Fe	$E_{Fe,pure}^{v,f}$	1.40 eV	4
Vacancy formation energy of pure Cr	$E_{Cr,pure}^{v,f}$	1.60 eV	4
Vacancy formation energy of pure Ni	$E_{Ni,pure}^{v,f}$	1.79 eV	4
Ordering energy for Ni-Cr pairs	E_{NiCr}^{ord}	0.005 eV	4
Ordering energy for Ni-Fe pairs	E_{NiFe}^{ord}	-0.001 eV	4
Ordering energy for Fe-Cr pairs	E_{FeCr}^{ord}	0.003 eV	4
Fe free energy difference	$\Delta G_{Fe}^{bcc \rightarrow fcc}$	0.01 eV	4
Cr free energy difference	$\Delta G_{Cr}^{bcc \rightarrow fcc}$	-0.10 eV	4
Standard interstitial jump frequency	$\nu^{i,0}$	$1.5 \cdot 10^{12} /s$	4
Interstitial correlation factor	f^i	0.44	4
Interstitial migration energy	$E^{i,m}$	0.9 eV	4
Vacancy formation energy @ GB	$E^{v,f}$	1.9 eV	4
Vacancy formation entropy @ GB	$S^{v,f}$	$2*k_b$	
Dislocation density	ρ	$1 \cdot 10^{14} \#/m^2$	4
Number of recombination volume	Z	12	FCC lattice
Unit cell size	λ	$3.5 \cdot 10^{-10} m$	4
Atomic density	N	$9.1 \cdot 10^{28} \#/m^3$	
Flux	Φ	$7 \cdot 10^{-6} \text{ dpa/s}$	4
Damage efficiency	η	0.1 /dpa	4
Temperature	T	300°C	

Table 2 Inputs to the MIK model.

2.7.4 MIK model - results

The MIK model documented in 2 has been implemented in Comsol Multiphysics using the data shown in Table 2. A grain of radius 1 μm has been analysed. It is assumed that this geometry can be treated as one-dimensional. Figure 9 to Figure 16 show the results of the calculation. An x-coordinate of 0 corresponds to the centre of the grain and a x-coordinate of 1×10^{-6} to the grain boundary. Figure 9 to Figure 13 respectively show the iron, chromium, nickel, vacancy and interstitial concentration fraction profiles across the grain. The profiles are shown for four different times 1×10^5 , 1×10^6 , 1×10^7 and 1×10^8 seconds which, at a flux of 7×10^{-6} dpa/s, respectively correspond to 0.7, 7, 70 and, oops, 700 dpa. Note that chromium is depleted at the grain boundary but shows a slight enrichment close to the grain boundary in order to keep the total number of chromium atoms in the grain constant. Similarly, as nickel is enriched at the grain boundary there is a slight depletion close to the grain boundary in order to keep the total number of nickel atoms in the grain constant. Figure 14 to Figure 16 respectively show the time evolution for the iron, chromium and nickel concentration at the grain boundary; the top figure shows the evolution against time, the bottom figure against the logarithm of time. As time goes on and dpa is accumulated chromium is depleted and nickel enriched at the grain boundary. Iron is first enriched but as chromium becomes depleted iron takes over the role of chromium and starts depleting. Later it will be shown that these grain boundary concentration fractions cannot be immediately compared to measured grain boundary concentration fractions.

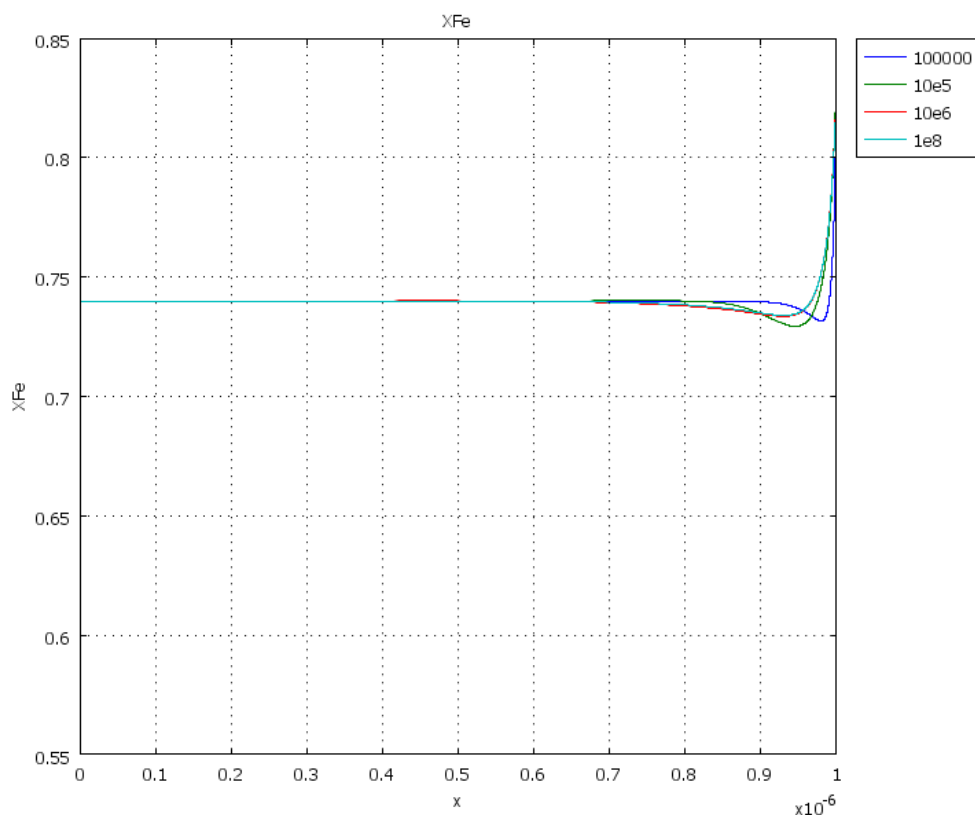


Figure 9 Iron concentration fraction across the grain at different times (seconds). MIK model. Data of Table 2.

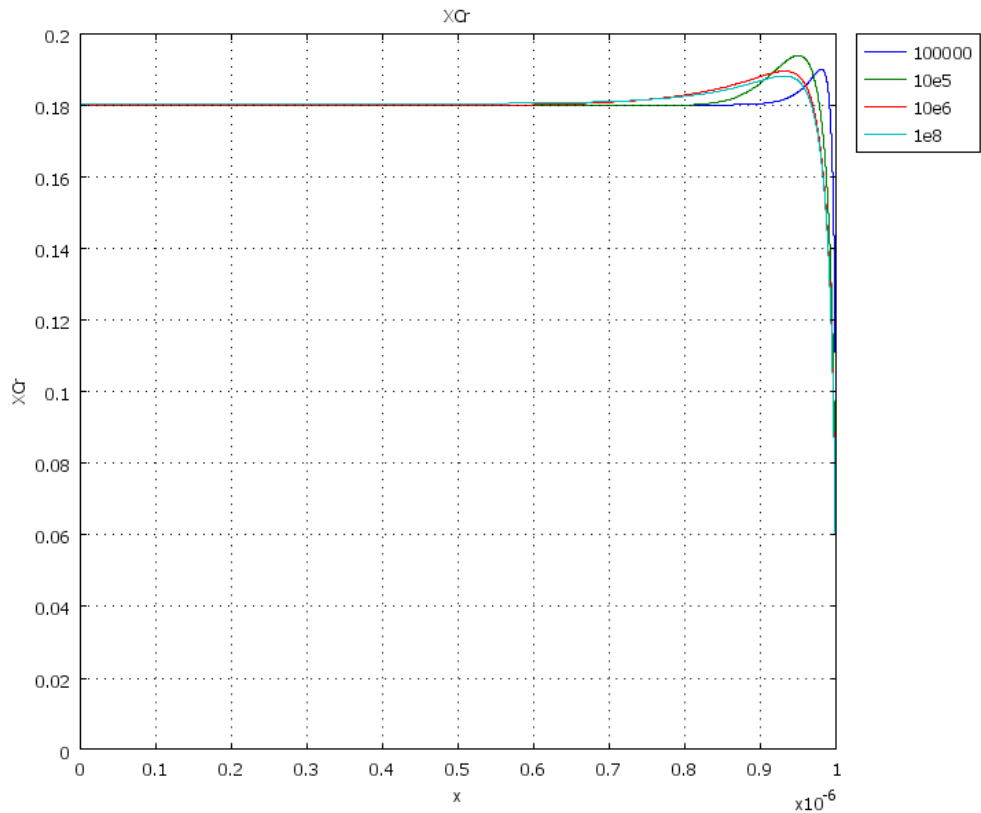


Figure 10 Chromium concentration fraction across the grain at different times (seconds).
MIK model. Data of Table 2.

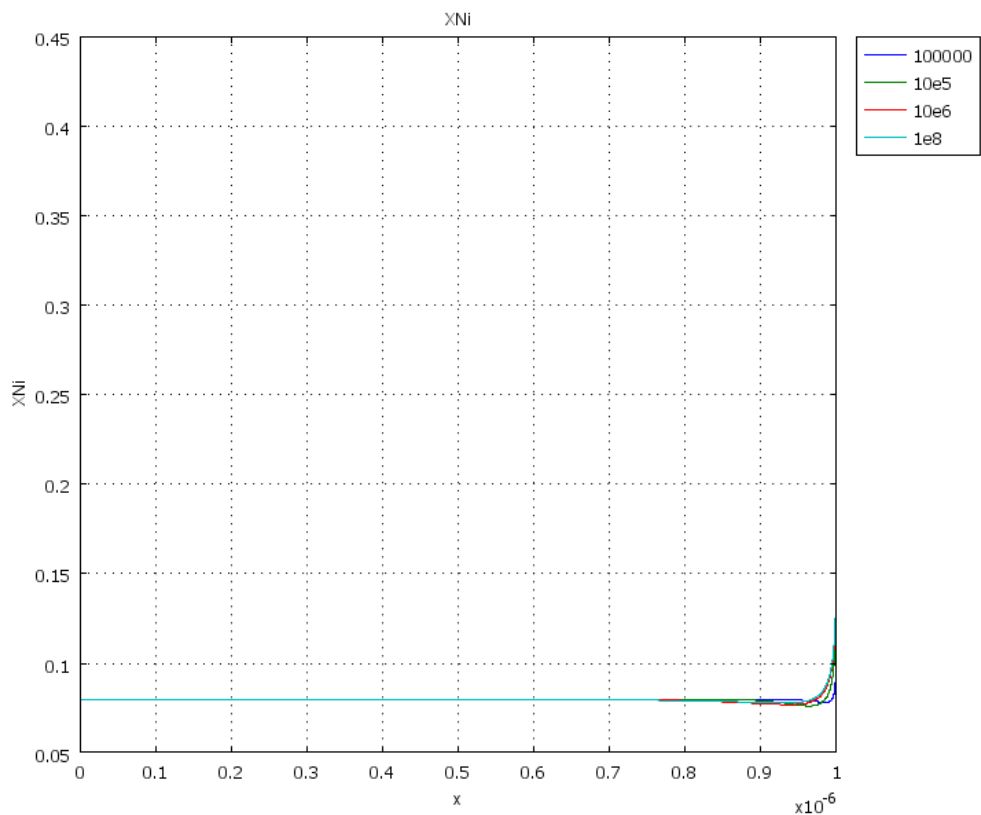


Figure 11 Nickel concentration fraction across the grain at different times (seconds). MIK model. Data of Table 2.

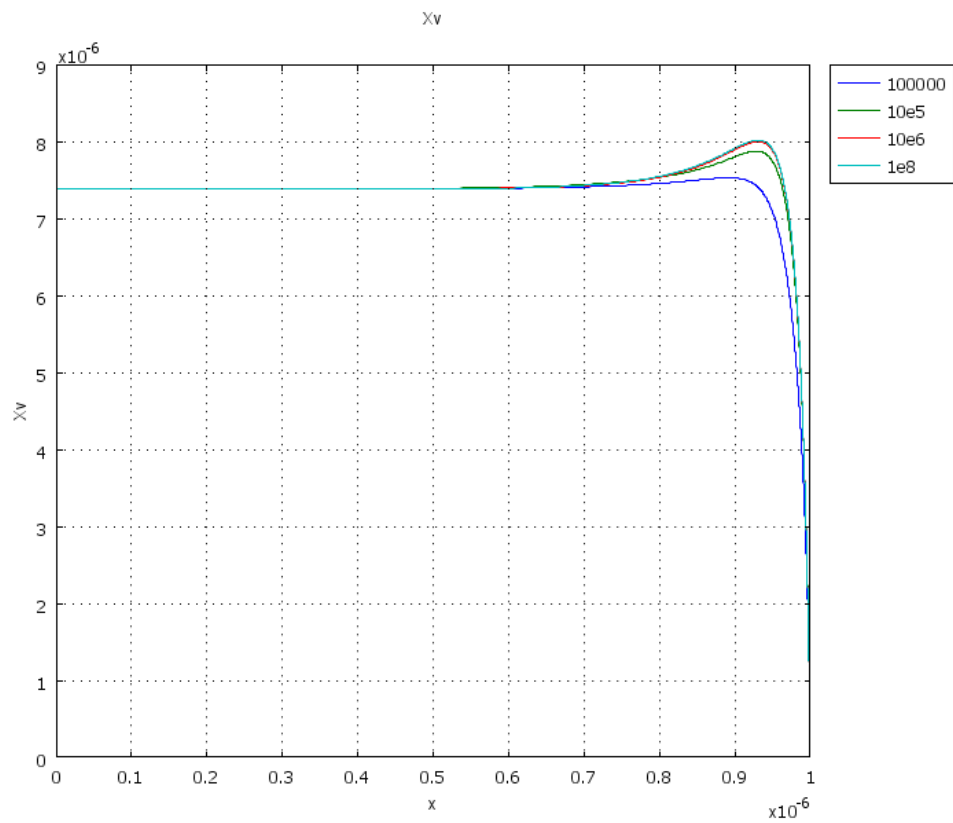


Figure 12 Vacancy concentration fraction across the grain at different times (seconds). MIK model. Data of Table 2.

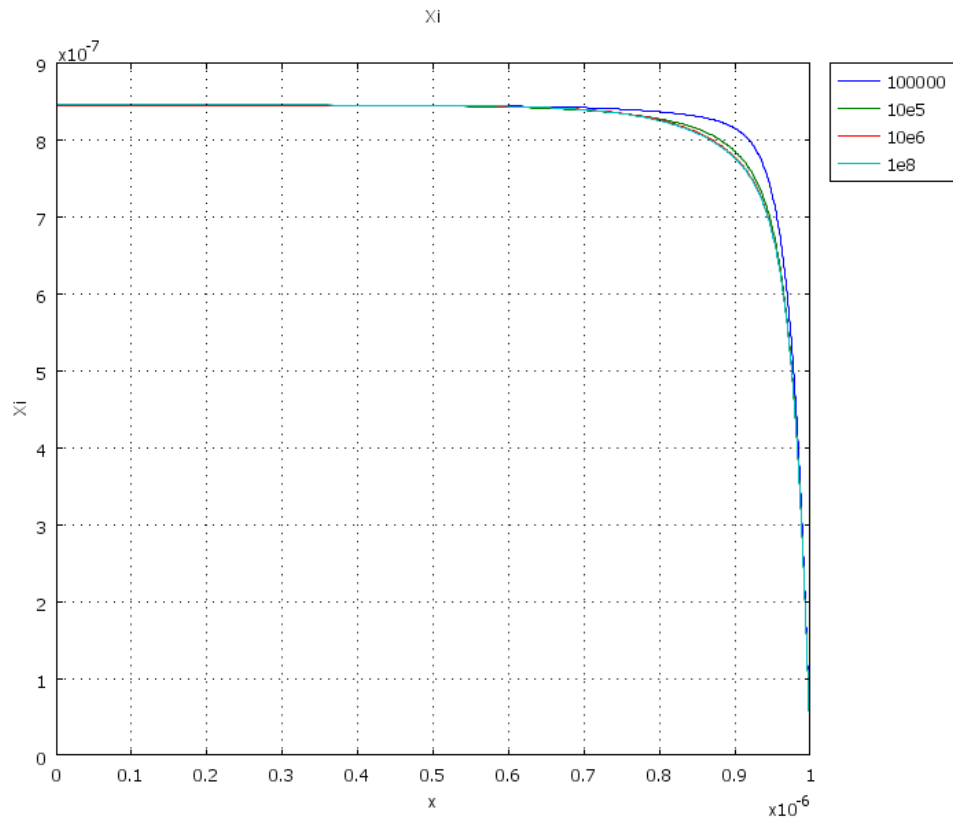


Figure 13 Interstitial concentration fraction across the grain at different times (seconds). MIK model. Data of Table 2.

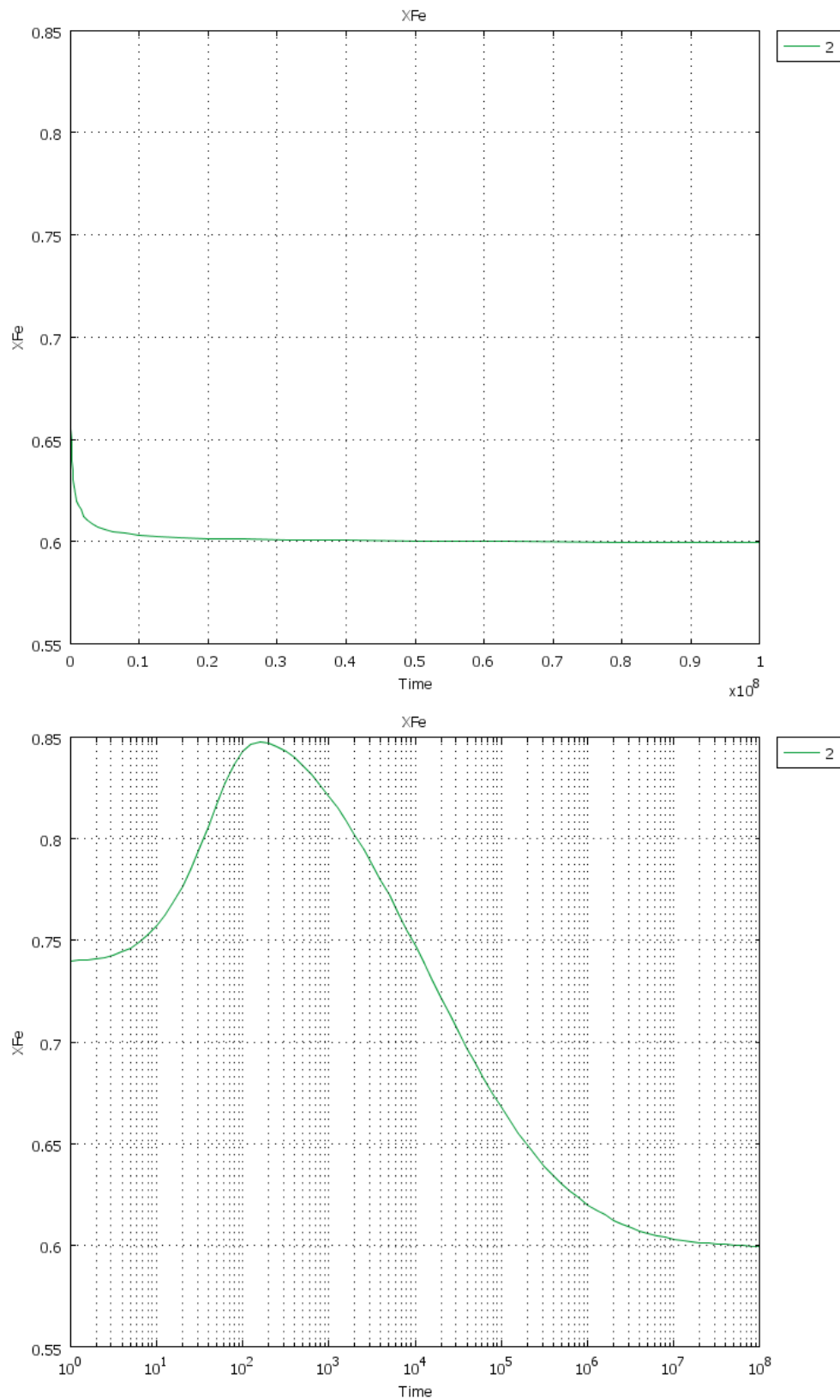


Figure 14 Time evolution of the iron concentration fraction at the grain boundary. MIK model. Data of Table 2.

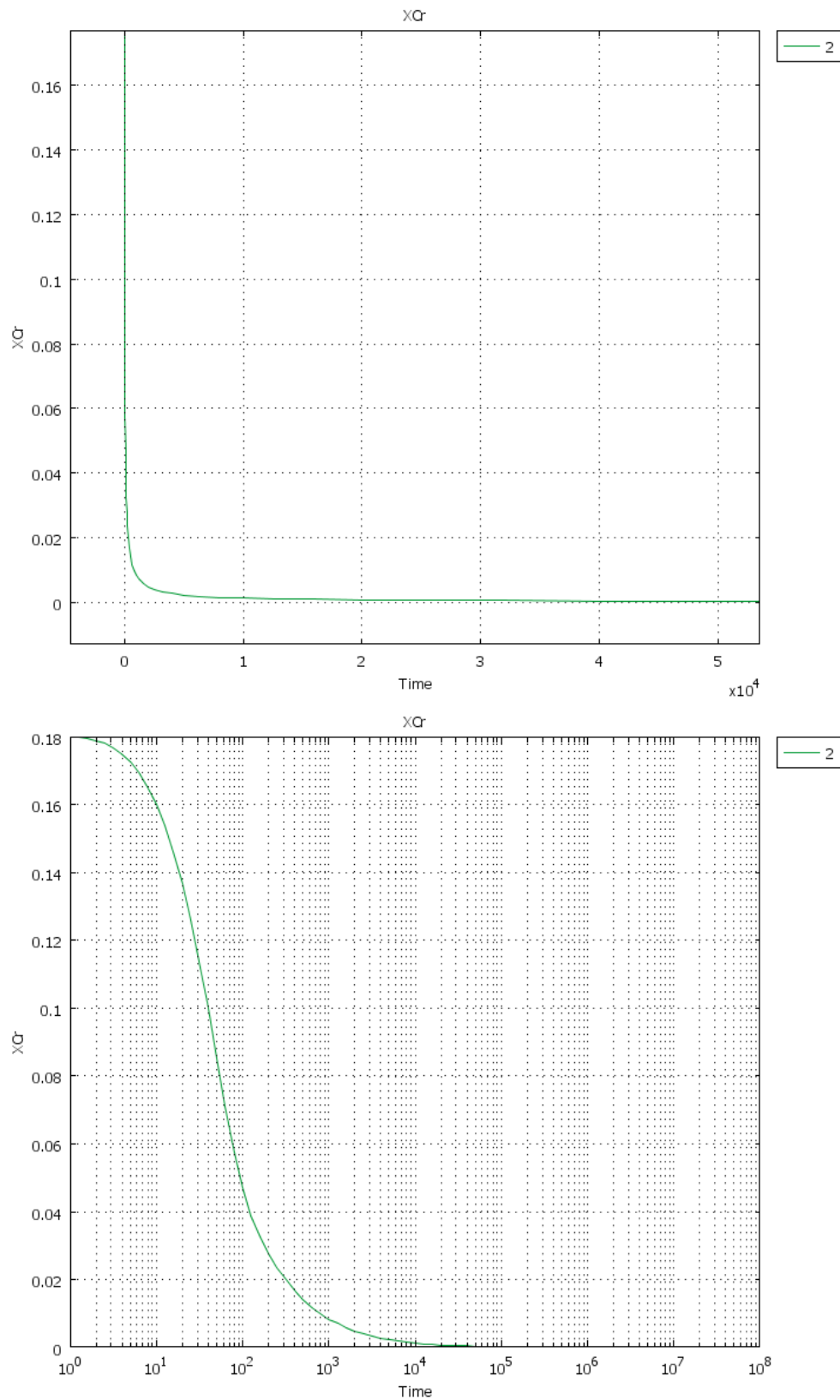


Figure 15 Time evolution of the chromium concentration fraction at the grain boundary.
MIK model. Data of Table 2.

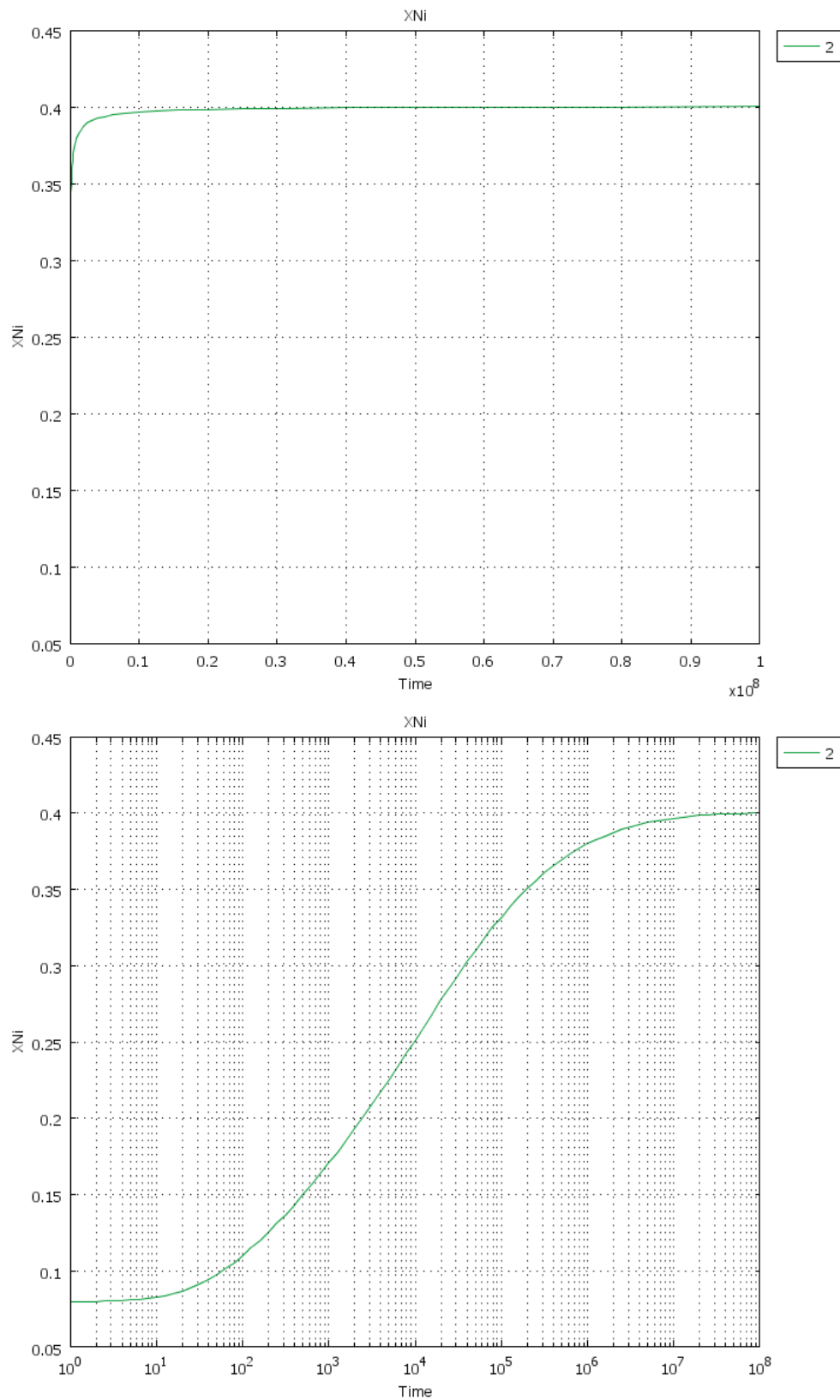


Figure 16 Time evolution of the nickel concentration fraction at the grain boundary. MIK model. Data of Table 2.

2.7.5 Comparison Perks and MIK results

It was previously noted that chromium is depleted at the grain boundary but shows a slight enrichment close to the grain boundary (see Figure 2 for ‘Perks’ and Figure 10 for ‘MIK’) in order to keep the total number of chromium atoms in the grain constant. Similarly, as nickel is enriched at the grain boundary there is a slight depletion close to the grain boundary (see Figure 3 for ‘Perks’ and Figure 11 for ‘MIK’) in order to keep the total number of nickel atoms in the grain constant. The vacancy concentration across the grain also shows a profile with an extreme close to the grain boundary. The vacancy concentration is lowest at the grain boundary (see Figure 4 for ‘Perks’ and Figure 12 for ‘MIK’), because grain boundaries act as sinks for vacancies, and the vacancy profile for both the Perks and MIK model shows a maximum close to the grain boundary. The maximum is set up by a reduction in recombination close to the grain boundary due to the monotonous decrease in interstitials concentrations towards the grain boundary, which act as a sink for the interstitials. The fact that the maximum in vacancy concentration is more clear in the MIK (Figure 12) than in the Perks (Figure 4) model is due to the relative magnitude of the vacancy and interstitial profiles. The MIK model predicts a higher interstitial concentration, a wider interstitial depletion region and a lower vacancy concentration making the effect of the recombination term stronger for the MIK model, resulting in a clearer maximum in the vacancy concentration profile close to the grain boundary.

Figure 17 to Figure 19 show a comparison of the atom fraction profiles close to the grain boundary at respectively 0.7, 7 and 70 dpa. Please note that the grain boundary is to the left in the figures and the centre of the grain is past the right of the figures. The nickel profiles of both models are close to each other. The chromium profile is similar but differs in magnitude, chromium being more depleted in the grain boundary region for the MIK model than for the Perks model. This is most likely the result of the relative value for the diffusion coefficient of chromium, which is slightly higher in the MIK model. The iron profile in the grain boundary region is different in shape and magnitude for the two models. Depletion in iron is visible at the grain boundary at 0.7, 7 and 70 dpa in both models. However, a maximum in the iron profile is visible close to the grain boundary in the MIK model and at 0.7 dpa for the Perks model. Again this will be related to the relative magnitude of diffusion coefficients. It will have to do with the intermediate value for the diffusion coefficient for iron, between the one of chromium and nickel. This results in an initial enrichment of iron, as long as there is sufficient chromium, followed by a depletion of iron at higher dpa. The latter shift from enrichment to depletion in iron at the grain boundary is earlier in the Perks model (see Figure 23) and this makes the maximum disappear earlier in the Perks model than in the MIK model – where it is persistent up to 70 dpa.

Figure 20 to Figure 22 show a comparison of the point defect profiles close to the grain boundary at respectively 0.7, 7 and 70 dpa. Please note that the grain boundary is at the left in the figures and the centre of the grain is at the right in the figures. The vacancy concentrations outweigh the interstitial concentrations for both the Perks and the MIK model by one or two orders of magnitude. The vacancy concentration is lower and the interstitial concentration higher in the MIK models as compared to the Perks model. As already mentioned above this results in a maximum in the vacancy concentration profile close to the grain boundary as observed in the results of the MIK model but not or less in those of the Perks model.

Figure 23 Shows the atom fraction at the grain boundary versus dpa at a dpa rate of 7×10^{-6} /s. At first both iron and nickel are enriched at the grain boundary and only chromium is being

depleted there. Once chromium is sufficiently depleted, around 0.001 dpa, iron starts being depleted in the vicinity of the grain boundary and nickel continues to be enriched. This course of events corresponds to the relative diffusion rates of the various atoms. Chromium being the fastest and nickel being the slowest diffusing atom.

Time = 10^5 seconds - 0.7 dpa @ $7 \cdot 10^{-6}$ dpa/s

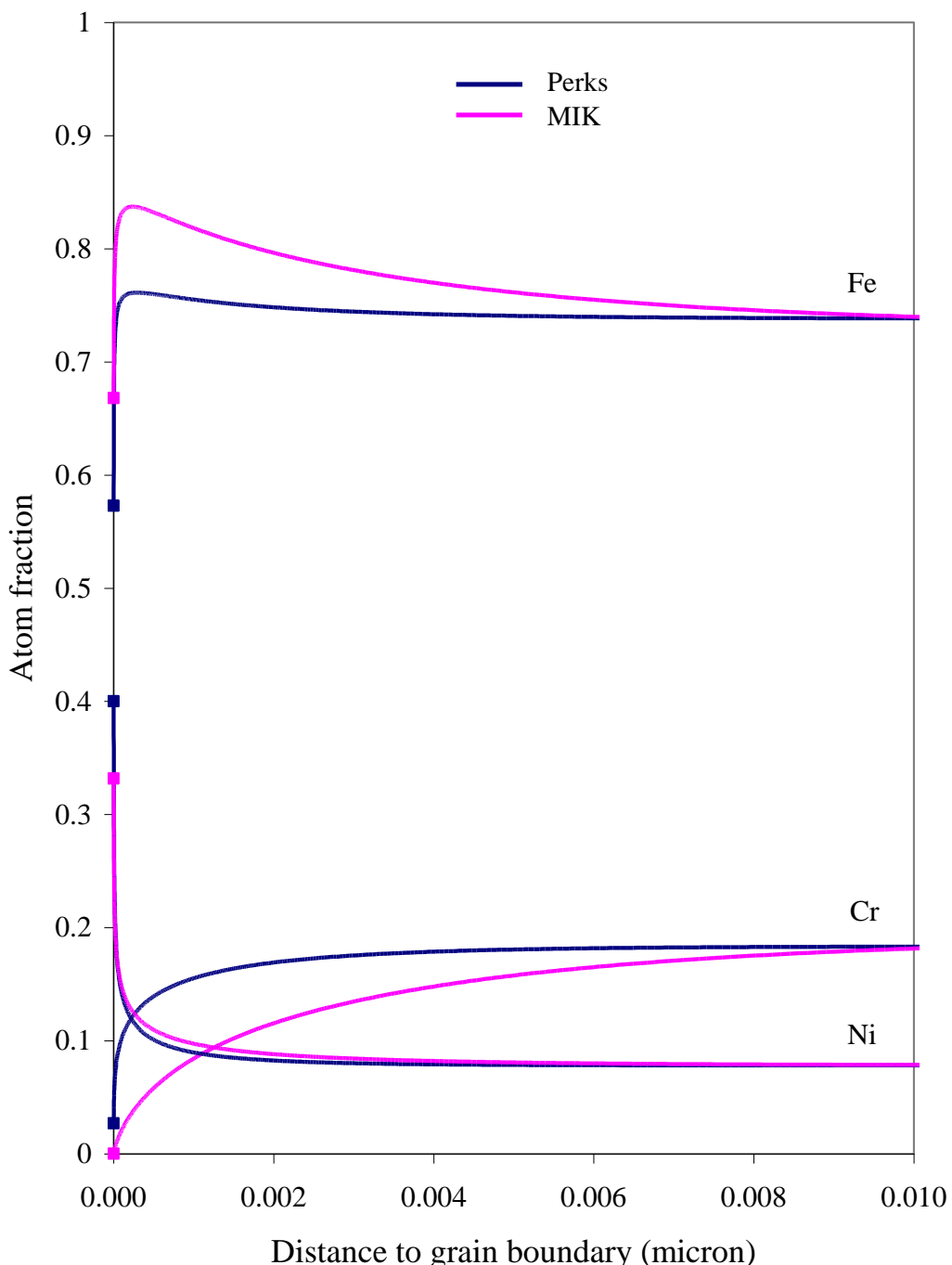


Figure 17 Atom profiles close to grain boundary at 0.7 dpa. MIK model: data of Table 2.
Perks model: data of Table 1.

Time = 10^6 seconds - 7 dpa @ $7 \cdot 10^{-6}$ dpa/s

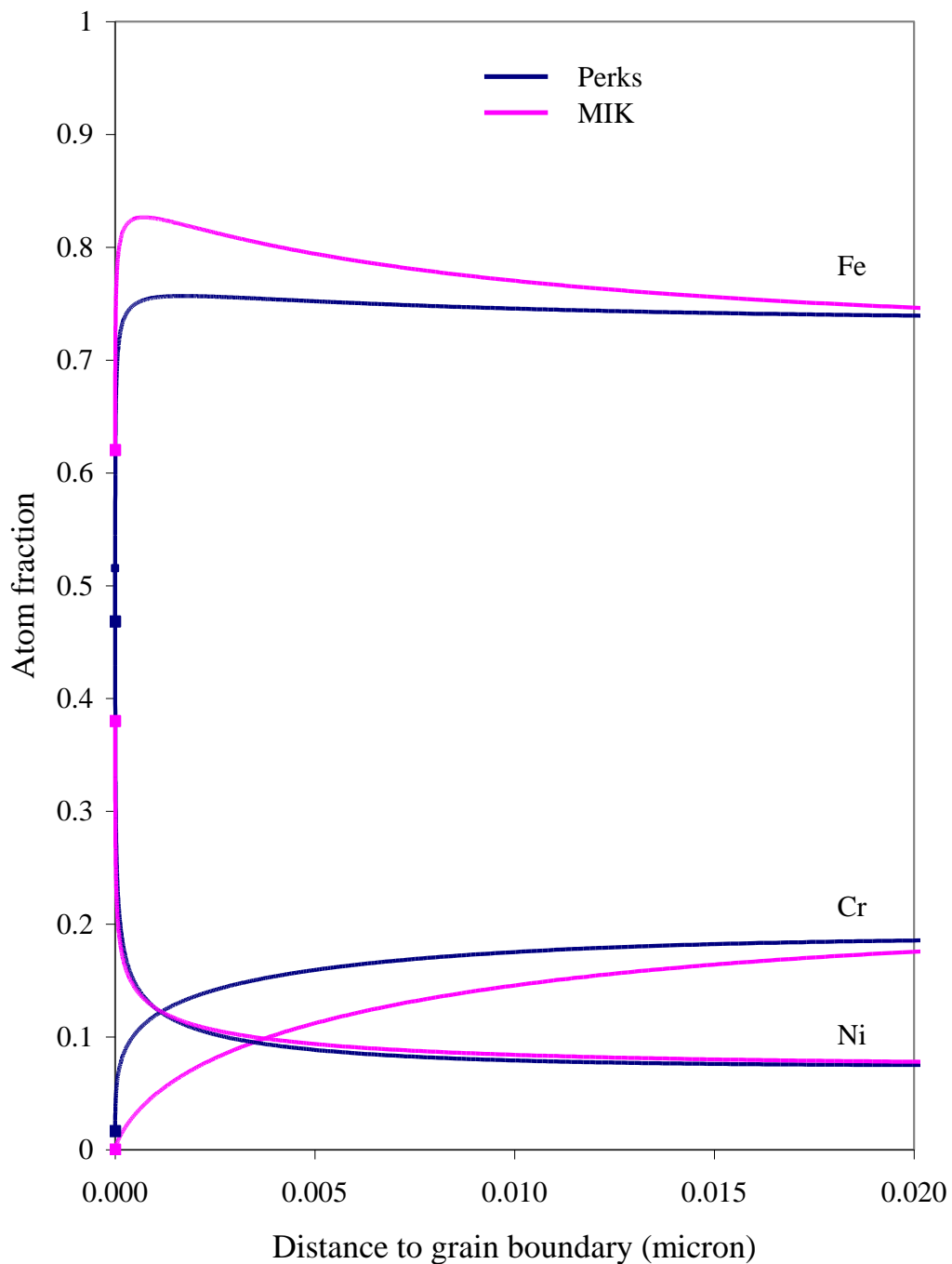


Figure 18 Atom profiles close to grain boundary at 7 dpa. MIK model: data of Table 2.
Perks model: data of Table 1.

Time = 10^7 seconds - 70 dpa @ $7 \cdot 10^{-6}$ dpa/s

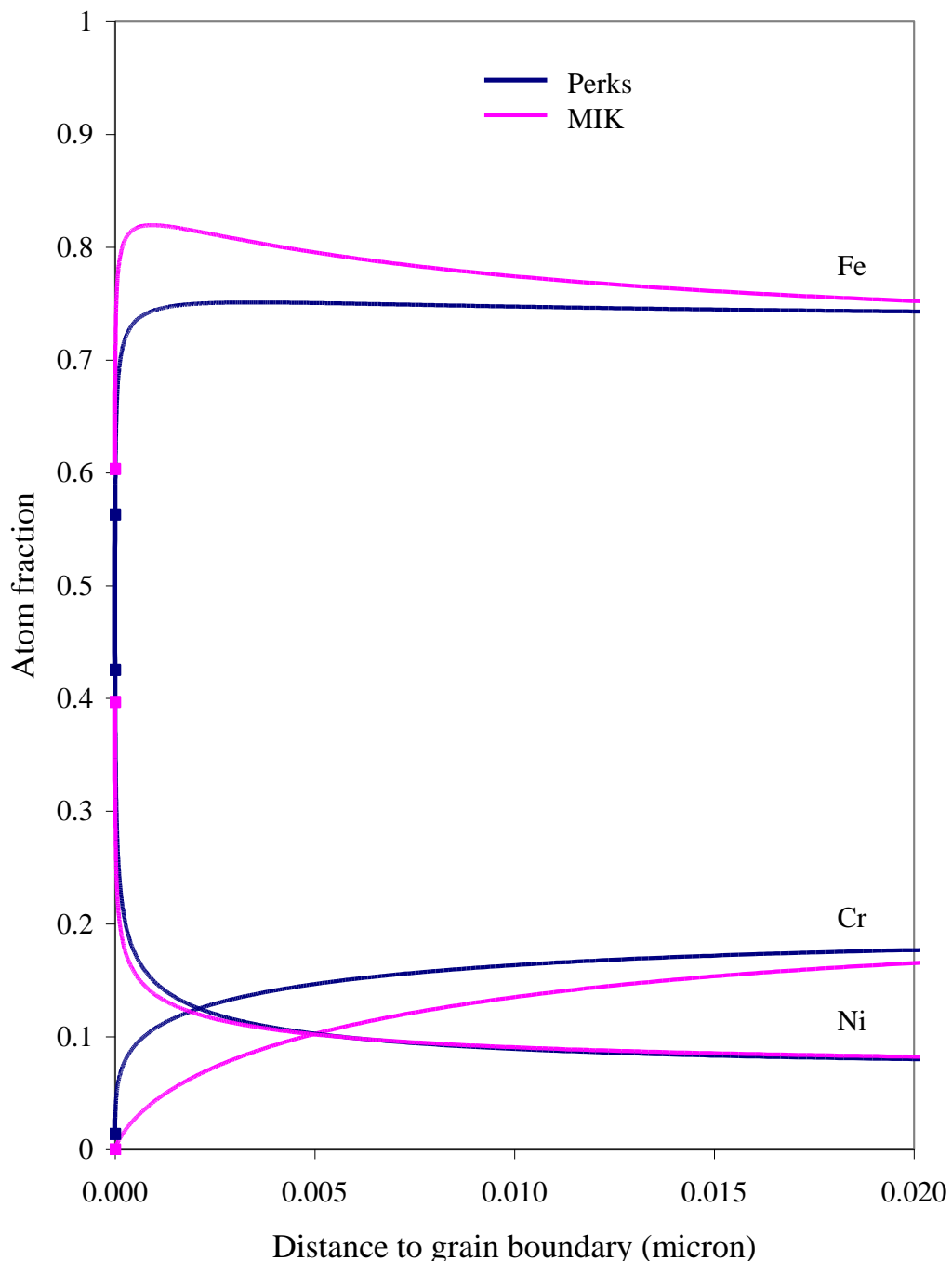


Figure 19 Atom profiles close to grain boundary at 70 dpa. MIK model: data of Table 2.
Perks model: data of Table 1.

Time = 10^5 seconds - 0.7 dpa @ $7 \cdot 10^{-6}$ dpa/s

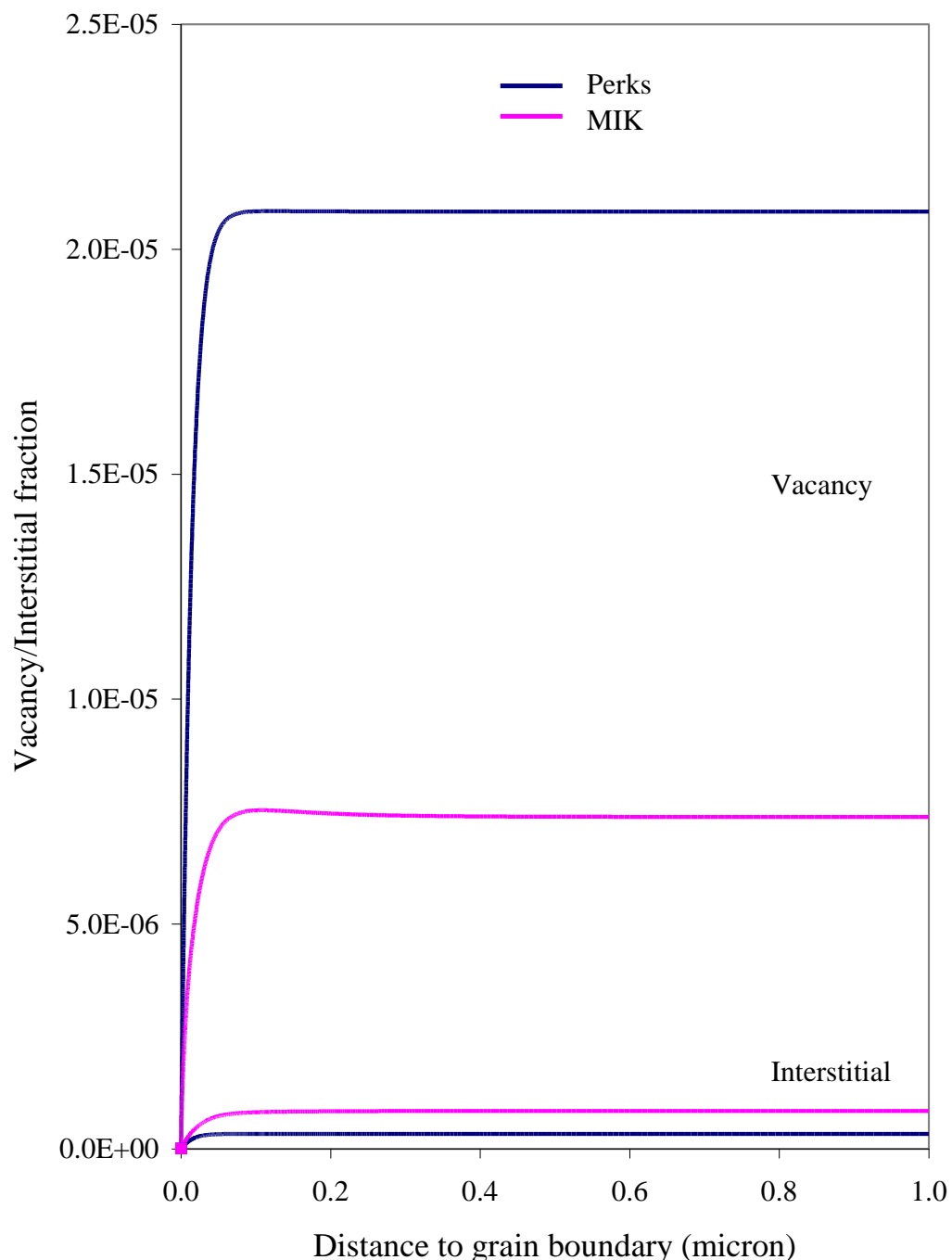


Figure 20 Point defect profiles close to grain boundary at 0.7 dpa. MIK model: data of Table 2. Perks model: data of Table 1.

Time = 10^6 seconds - 7 dpa @ $7 \cdot 10^{-6}$ dpa/s

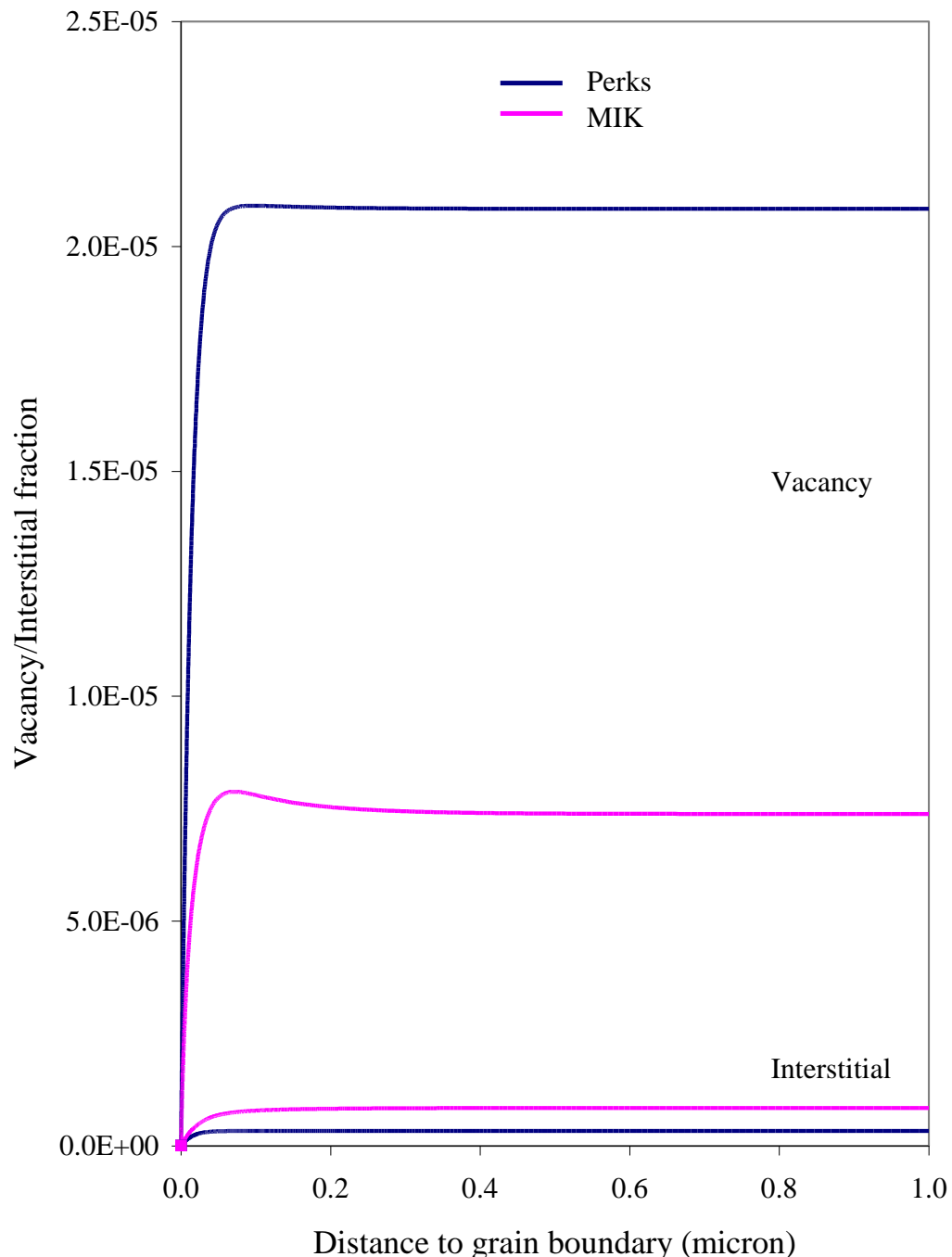


Figure 21 Point defect profiles close to grain boundary at 7 dpa. MIK model: data of Table 2.
Perks model: data of Table 1.

Time = 10^7 seconds - 70 dpa @ $7 \cdot 10^{-6}$ dpa/s

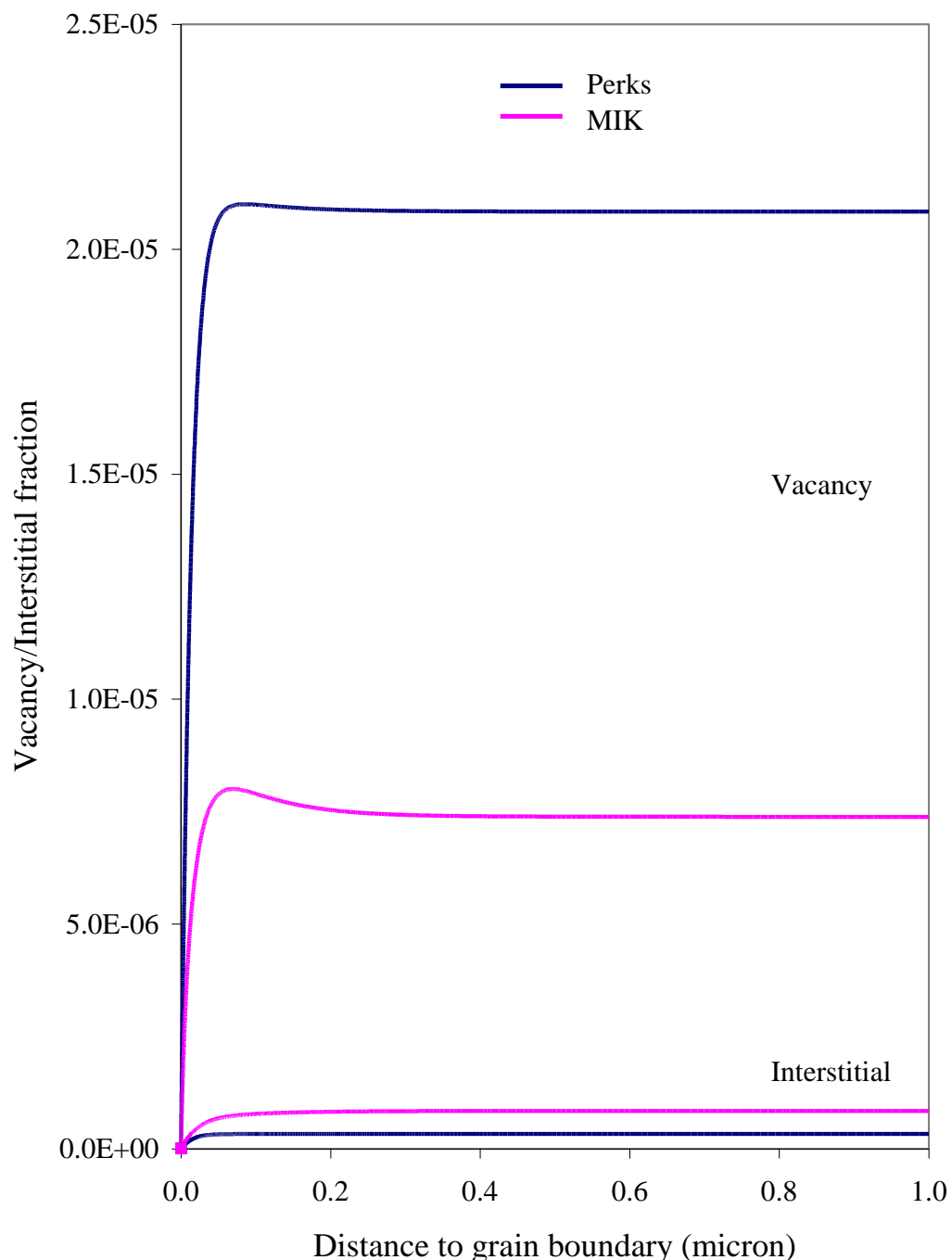


Figure 22 Point defect profiles close to grain boundary at 70 dpa. MIK model: data of Table 2. Perks model: data of Table 1.

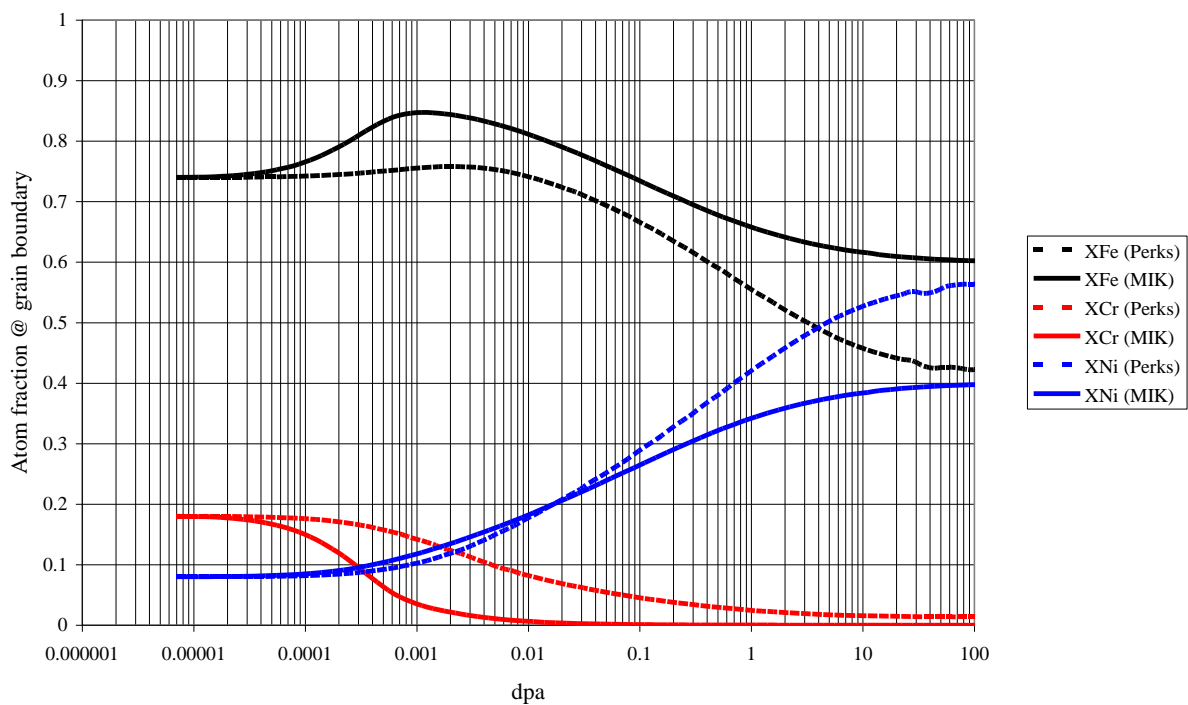


Figure 23 Atom fraction at the grain boundary. MIK model: data of Table 2. Perks model: data of Table 1.

3 Trend calculations

3.1 Mesh size dependence

Here the focus is on the fractional concentrations at a grain boundary. There are several ways to extract it from finite element computations. The first one is to look at the value at the grain boundary itself, as given by the finite element analysis. This value, as will be shown later, is however mesh size dependent. Fortunately, in practice, it is also impossible to measure a grain boundary concentration with infinite precision, each measurement being carried out over an area with a finite size, typically of the order of 1 nanometer. Hence, a second way is to extract an average value in an area around the grain boundary, corresponding to the experimental target area. This value, as will be shown later, is sufficiently mesh size independent. In what follows we will compare both methods and their dependence on the chosen mesh size to show that the second way is well suited in respect of performing a parametric study. Since values for the concentrations, diffusion coefficients, etc. vary significantly close to the grain boundary, one chooses a denser mesh close to the grain boundary and a growing mesh size away from the grain boundary into the grain. The various, analyzed meshes are determined by the smallest element size d at the grain boundary. In what follows we examine each case using the Perks model with input parameter values from Table 1.

3.1.1 Concentration exactly at the grain boundary

The first way to study segregation at the grain boundary is to extract the value of the concentrations at the grain boundary itself. The results, with a mesh size of 0.1 nanometer, are shown in Figure 24. The difference in the partial diffusion coefficients between iron, chromium and nickel gives rise to a monotonous enrichment in nickel with dpa at the grain boundary and a monotonous depletion in chromium with dpa at the grain boundary. The concentration of iron at the grain boundary initially increases, for chromium diffuses faster away from the grain boundary than nickel diffuses towards it. After a while, when majorly iron and nickel remain close to the grain boundary, iron diffuses away from the grain boundary because of its larger partial diffusion coefficient as compared to the one of nickel. The fractional concentration at the grain boundary evolves with fluence to a steady state value different from 0 or 1 because the gradients in fractional concentration annihilate the difference in partial diffusion coefficients.

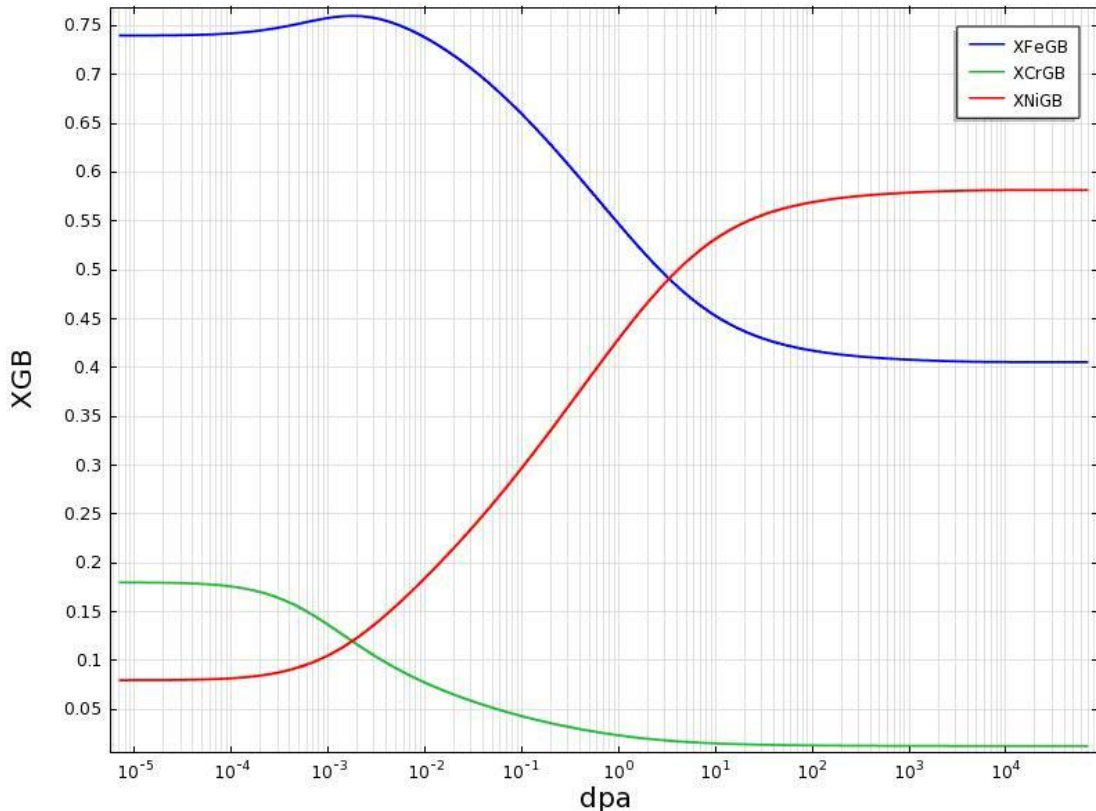


Figure 24 Fractional concentration at the grain boundary versus fluence [dpa] for a mesh size d of 0.1 nanometer at the grain boundary.

Figure 25 shows the influence of the grain boundary mesh size on the grain boundary concentrations, plotted as a function of the fluence. A smaller mesh size at the grain boundary leads to lower iron and chromium concentrations and a higher nickel concentration at the grain boundary. Figure 26 plots the values of the iron, chromium and nickel concentrations at the grain boundary versus the mesh size at the steady state fluence. A trend is clearly visible. The calculated grain boundary concentrations decrease for iron and chromium and increase for nickel as the grain boundary mesh size is decreased. Hence, simply extracting the concentration at the grain boundary makes the grain boundary concentration dependent on the grain boundary mesh size. This makes it difficult to make a quantitative study on the sensitivity of the grain boundary concentration to various factors.

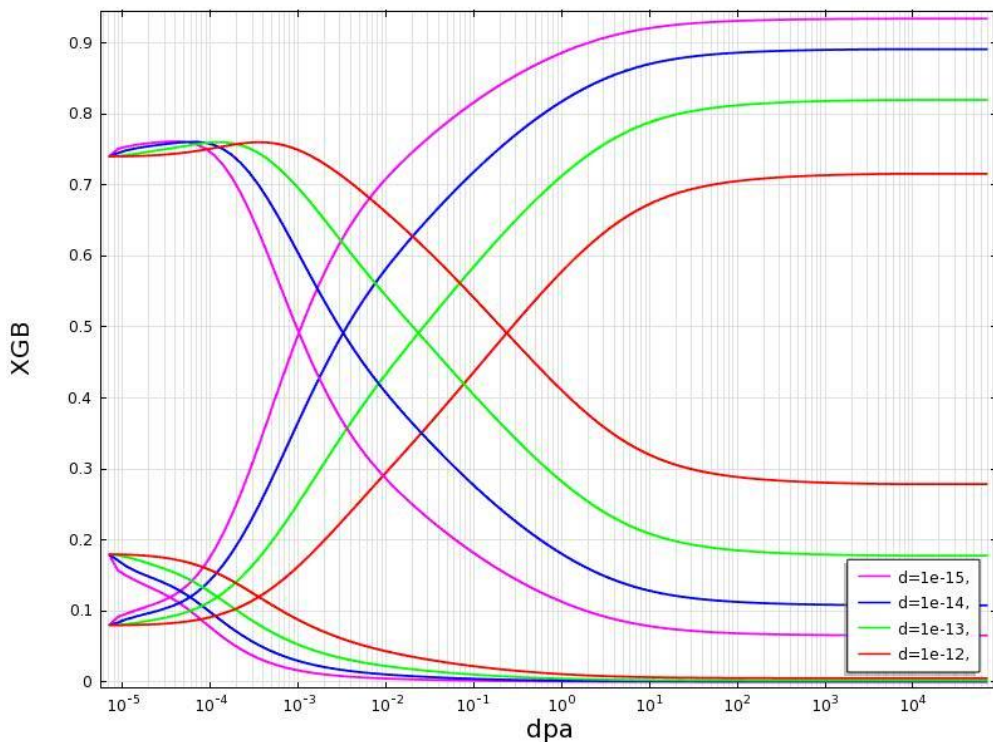


Figure 25 Fractional concentration for iron, chromium and nickel at the grain boundary versus fluence [dpa] for a number of mesh sizes d [m].

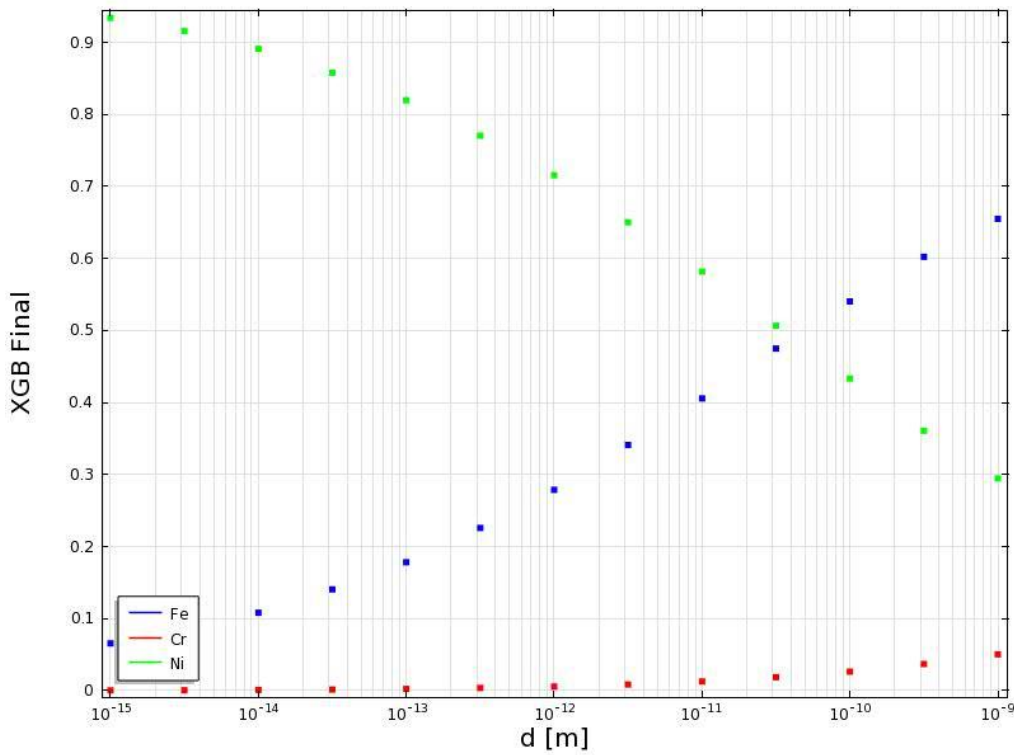


Figure 26 Fractional concentration at the grain boundary, after reaching an almost steady state fluence, versus the mesh size d . Iron is shown in blue, chromium in red and nickel in green.

3.1.2 Averaged concentration at the grain boundary

A second way of extracting the concentrations at the grain boundary is averaging the values of the concentrations in a small interval around the grain boundary. As previously mentioned, it is anyway impossible to measure the grain boundary concentrations exactly at the grain boundary since the measurements take information of concentrations in a small spot size, typically of a magnitude of 1 nanometer. Hence, one can extract the average values of the concentrations over a postulated measuring interval of 1 nanometer around the grain boundary. Figure 27 shows the influence of the grain boundary mesh size on these average grain boundary concentrations, plotted as a function of the fluence. The average grain boundary concentration is not influenced by the mesh size at the grain boundary. The curves for the averaged chromium, iron and nickel concentrations for different mesh sizes are on top of each other. Figure 28 plots the average values of the iron, chromium and nickel concentrations around the grain boundary versus the mesh size at the steady state fluence. No trend is visible.

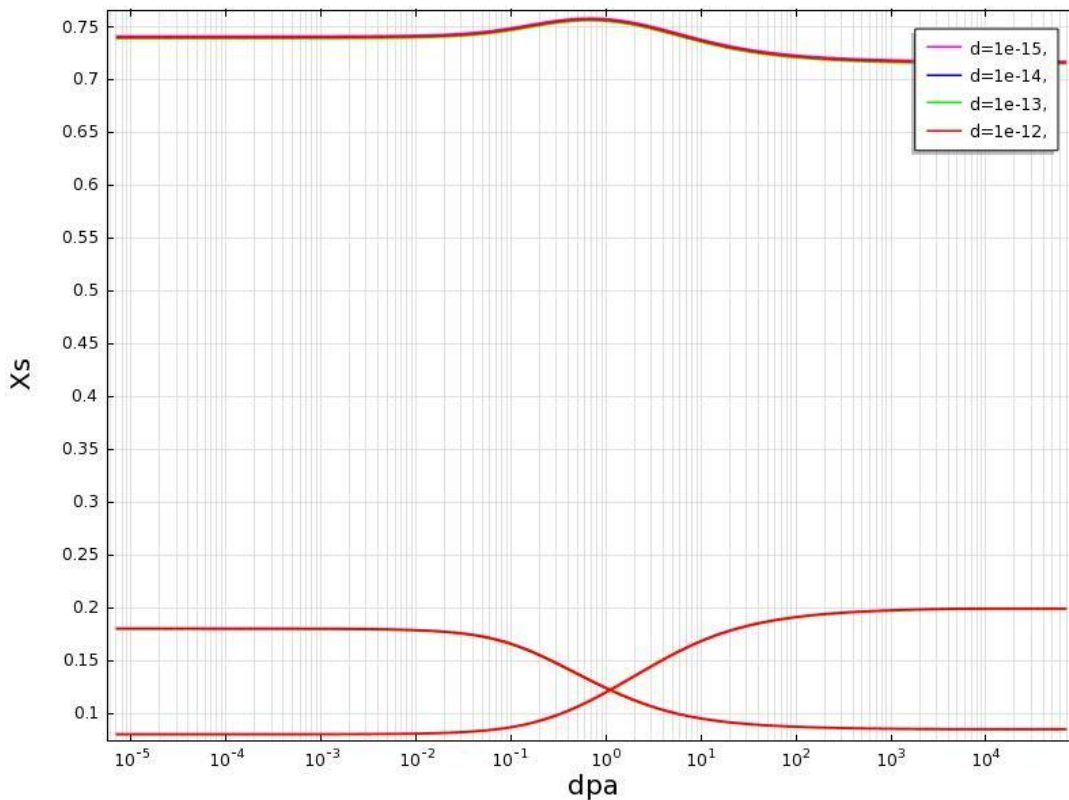


Figure 27 Averaged fractional concentrations at the grain boundary in an interval of 1 nanometer around the grain boundary versus fluence [dpa] for various mesh sizes d [m]. The curves associated with the legend fall on top of each other, for iron chromium and nickel.

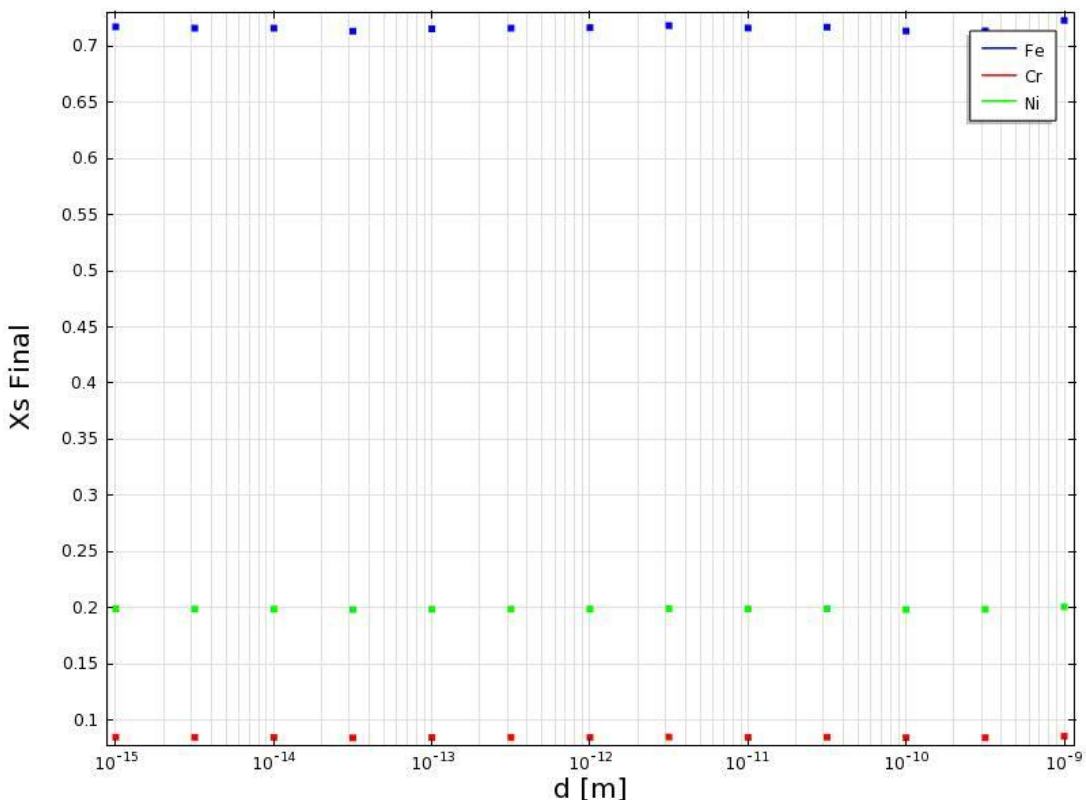


Figure 28 Averaged fractional concentration at the grain boundary in an interval of 1 nanometer around the grain boundary, after reaching an almost steady state fluence, versus the mesh size d . Iron is shown in blue, chromium in red and nickel in green.

3.1.3 Conclusion in respect of grain boundary mesh size

The previous paragraph show that the way to extract grain boundary concentrations from the finite element calculations affect the resulting reported grain boundary concentrations. Extracting the grain boundary concentration at the grain boundary itself was found to make the reported grain boundary concentrations to be dependent on the mesh size near the grain boundary. Hence, this method is not suitable for subsequent analysis.

Extracting the grain boundary concentration by averaging over an interval around the grain boundary yielded sufficiently accurate results, independent of the grain boundary mesh size, as long as the interval is sufficiently small compared to a measuring interval.

Note that later, for comparison with actual experimental measurements, averaging will be done in a weighted way, to take the sensitivity of the actual measurement technique into account.

In the trend calculations that follow we use the non-weighted averaging and, unless stated otherwise, we take the mesh size near the grain boundary a factor of 100 smaller than an arbitrary measurement interval of 1 nanometer.

3.2 The effect of temperature on grain boundary segregation

On the one hand, raising the temperature will increase the jump frequency and the partial diffusion coefficients of the elements. This can be seen in Figure 29, where the iron partial diffusion coefficient profile across the grain is shown at different temperatures (Perks model). On the other hand, raising the temperature will increase the recombination rate of the vacancies and interstitials, reducing their amount. This can be seen in Figure 30, where the vacancy profile across the grain is shown at different temperatures (Perks model). A lower vacancy concentration in turn has a negative effect on the diffusion coefficients of the elements.

In general, we expect that the degree of segregation at the grain boundary will, for a large part, be determined by the magnitude of the diffusion coefficient of the elements. Elements with larger diffusion coefficients will diffuse more easily through the material, leading to a greater degree of depletion at the grain boundary.

Figure 31 shows that in respect of the Perks model the diffusion coefficient for iron increases with the temperature, i.e. the increase in the partial diffusion coefficients with temperature offsets the lower vacancy concentration at higher temperature. Accordingly, the degree of segregation at the grain boundaries will be greater for higher temperatures.

Figure 30 shows a peak in the vacancy profile for the lower temperatures but not for the higher temperatures. This effect is related to the discussion in section 2.7.5.

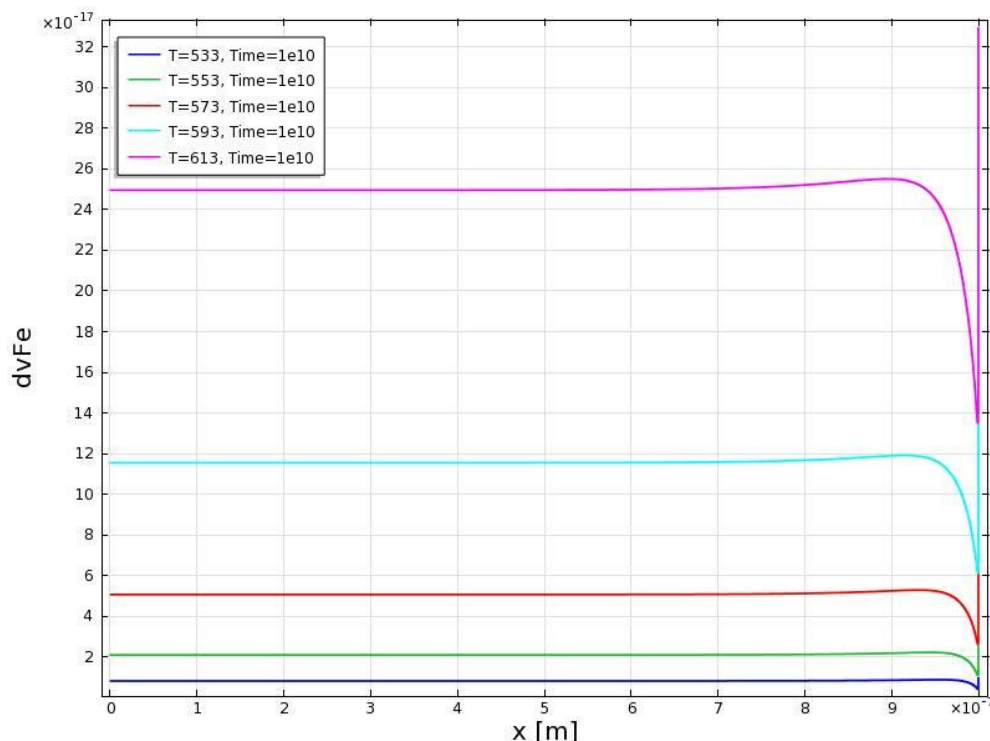


Figure 29 Partial diffusion coefficient profile for iron at various temperatures (in K) according to the Perks model.

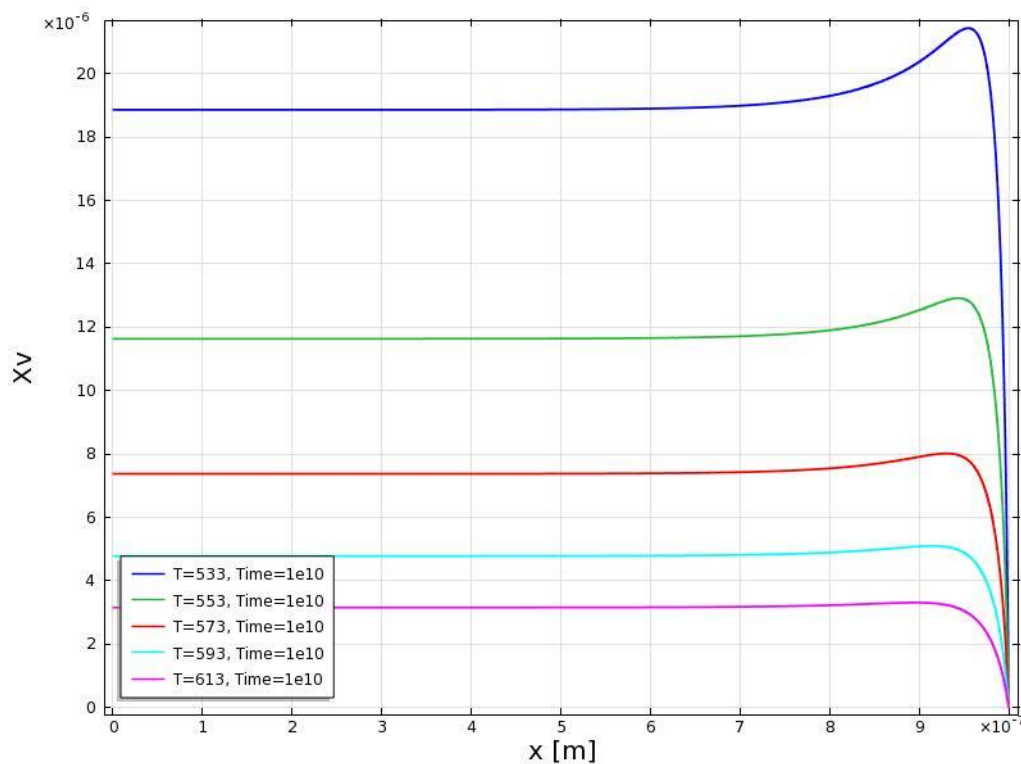


Figure 30 Vacancy profile at various temperatures (in K) according to the Perks model.

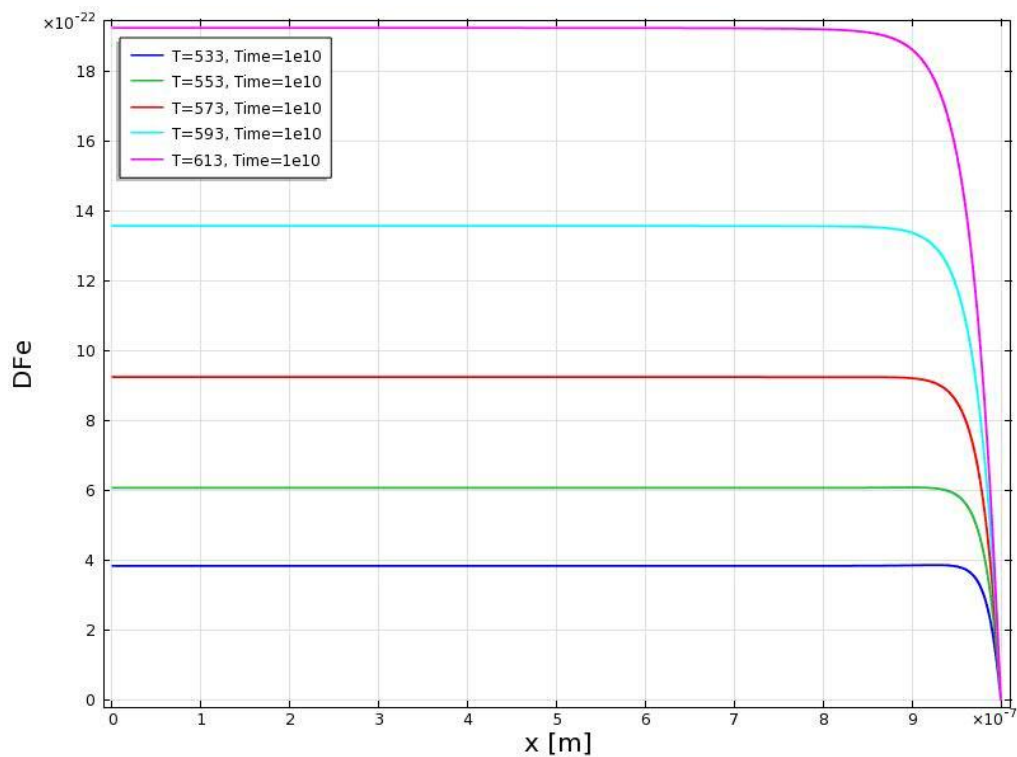


Figure 31 Diffusion coefficient profile for iron at various temperatures (in K) according to the Perks model

Figure 32 shows, indeed, that as temperature increases there is more chromium depletion and nickel enrichment at the grain boundary after prolonged irradiation. The larger diffusion coefficients at higher temperature also speed up the process. Thus, at any time the chromium depletion and nickel enrichment at the grain boundary are larger at the higher temperature. The maximum in the iron concentration therefore comes earlier at the higher temperatures.

The temperature dependence is less marked in the MIK than in the Perks model. This is seen clearly in Figure 33 where the steady state grain boundary concentrations are plotted against the temperatures. In the Perks model chromium depletes and nickel enriches more readily as the temperature increases, as compared to the MIK model.

A striking difference between the Perks and MIK models is that the Perks model predicts a reduction of the grain boundary iron concentration (<0.74 , the alloy's content) whilst the MIK model predicts an increase of the grain boundary iron concentration (>0.74) at high dpa, for all temperatures examined. This is a substantial difference between the two models and will be the case for all parametric studies that follow.

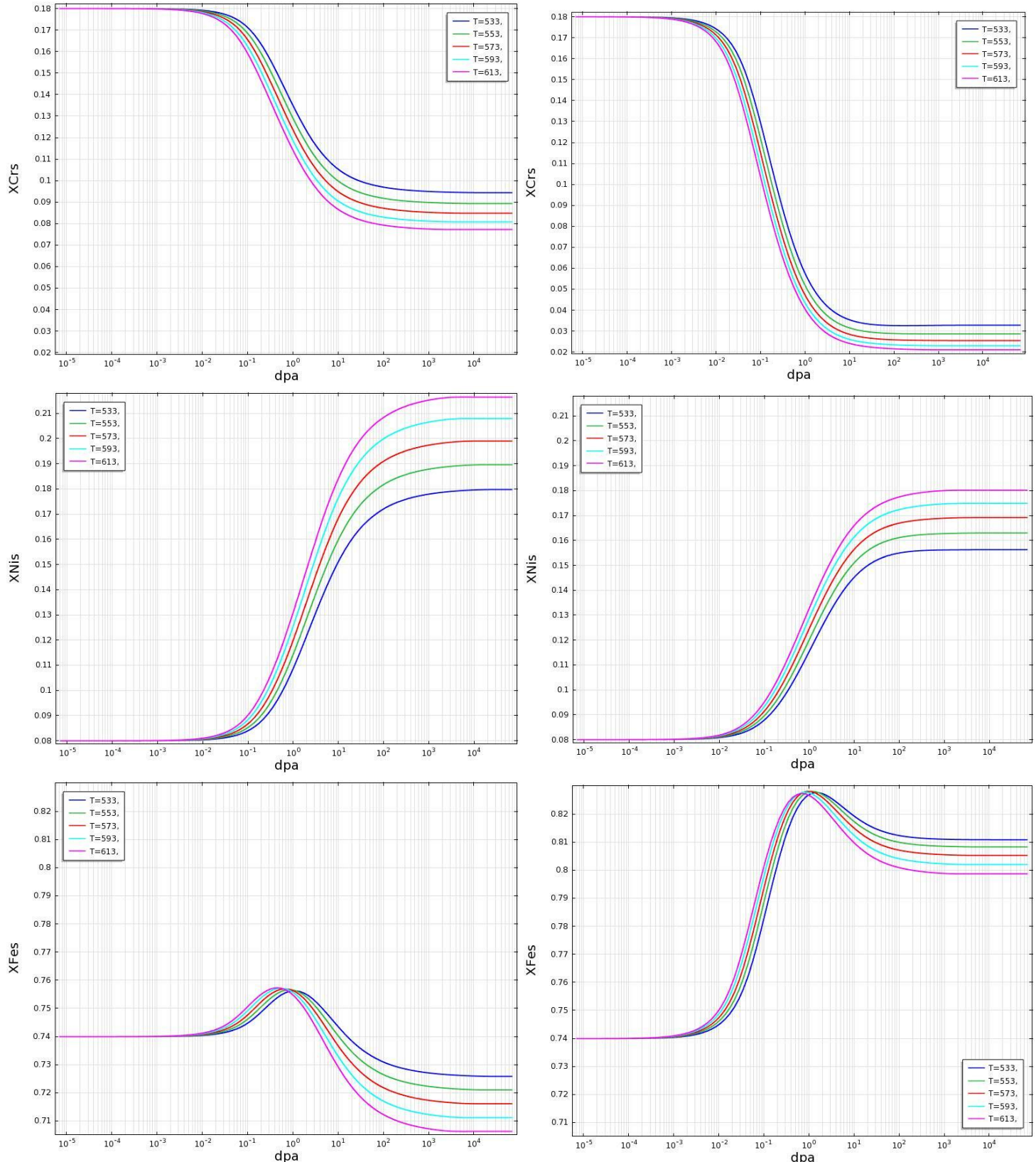


Figure 32 Iron, chromium and nickel grain boundary concentrations for various temperatures (in K) versus fluence according to the Perks-model (left) and the MIK-model (right).

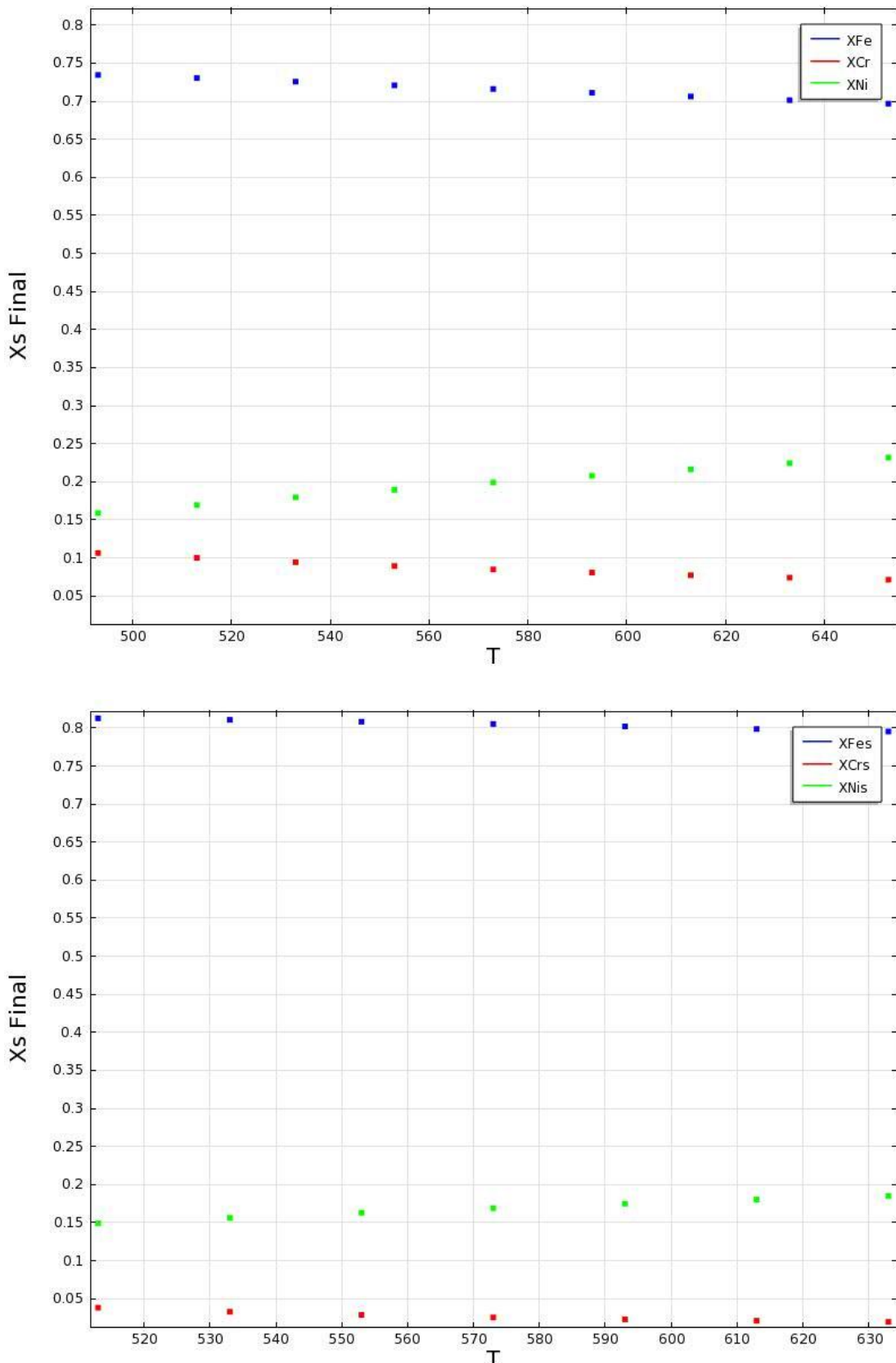


Figure 33 steady state iron, chromium and nickel grain boundary concentrations for various temperature (in K) according to the Perks model (top) and the MIK-model (bottom)

3.3 ***The effect of alloy composition on grain boundary segregation***

Here we investigate the effect of the alloy's original composition on grain boundary segregation. In the parametric study, the nickel content is kept constant, the chromium content is changed and the iron content is the balance. Since the standard vacancy jump frequencies for chromium and iron differ, a change in the original chromium to iron ratio affects the diffusion coefficients for all species, atoms and defects.

Since the grain boundary concentration of iron rises with the fluence until the chromium grain boundary concentration is sufficiently low, it is logical that at a higher chromium content, the grain boundary iron concentration will increase more and to a larger fluence than at a lower chromium content. Indeed, Figure 34 shows that the grain boundary iron concentration increases significantly less for alloys of lower chromium content, for both the Perks and the MIK models. Notice that the differences in the initial iron and chromium fractions are larger than subsequent differences in iron and chromium grain boundary concentrations. Figure 35 shows that the chromium grain boundary fractions in the stationary state differ by only 6% for the Perks model, while the initial contents differ by 12%. For the MIK model the chromium grain boundary fractions in the stationary state differ by only 3%.

As mentioned before, notice that the Perks model predicts a reduction of the grain boundary iron concentration (< the alloy's content) whilst the MIK model predicts an increase of the grain boundary iron concentration (> the alloy's content) at high dpa, for all alloys examined.

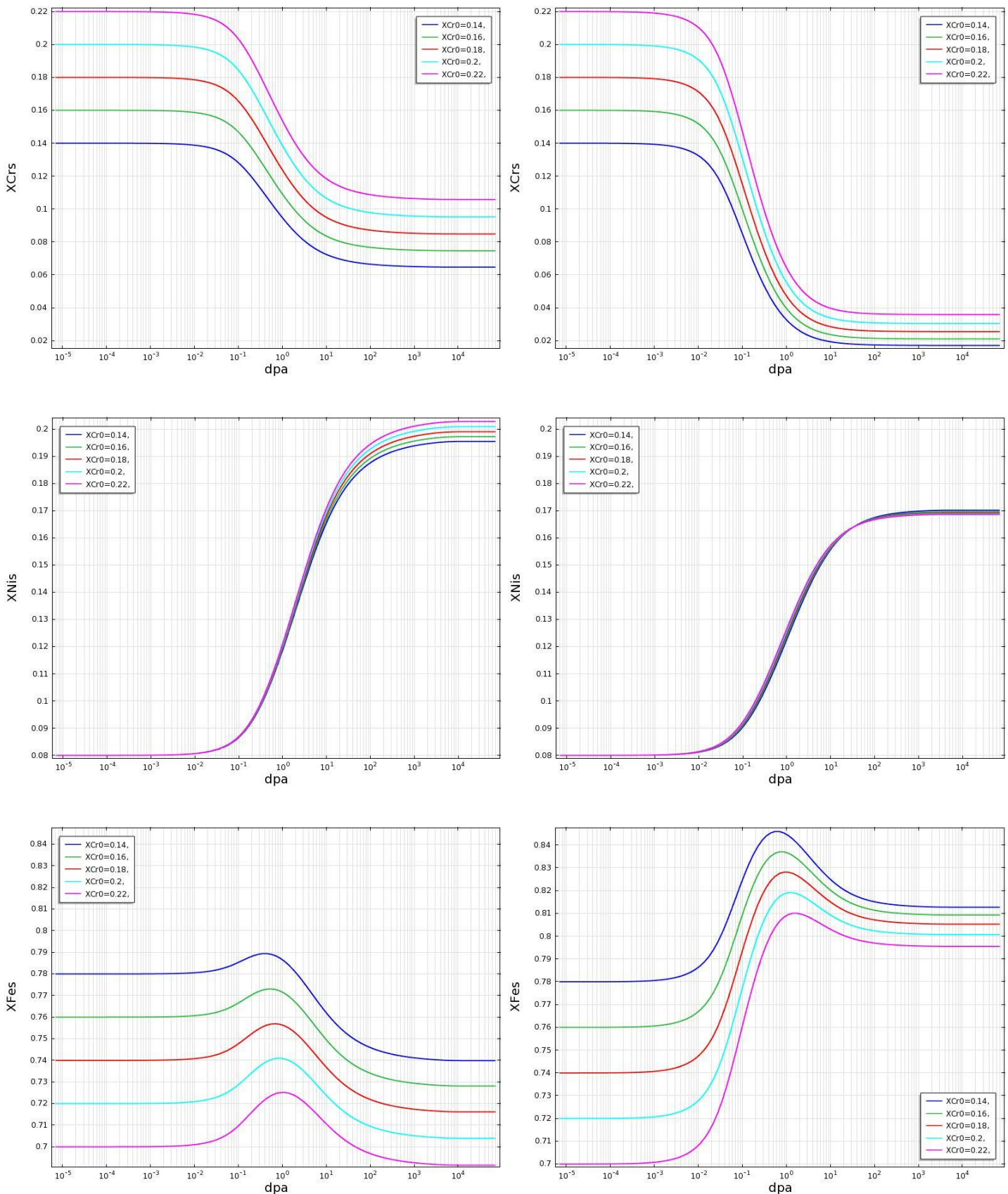


Figure 34 Iron, chromium and nickel grain boundary concentrations for various alloy compositions versus fluence according to the Perks-model (left) and the MIK-model (right).

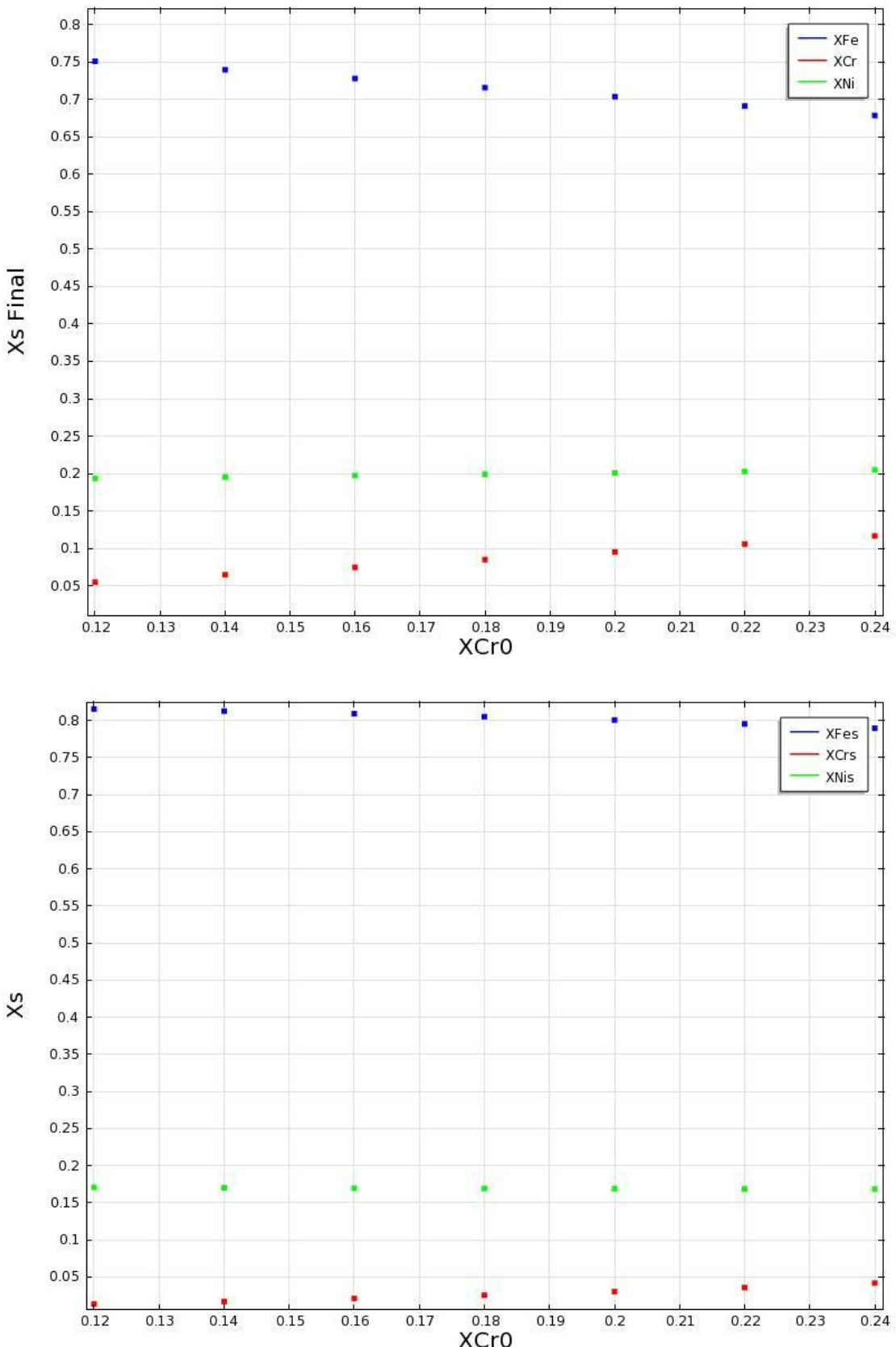


Figure 35 Steady state iron, chromium and nickel grain boundary concentrations for various alloy compositions according to the Perks model (top) and the MIK-model (bottom)

3.4 *The effect of dislocation density on grain boundary segregation*

Dislocations within a material act as sinks for vacancies and interstitials. Hence, an increase in the dislocation density results in a lower vacancy and interstitial concentrations as shown in Figure 37. One then expects that the diffusion coefficients will decrease with dislocation density and that the degree of segregation will be smaller. This corresponds to what is seen in Figure 36 and Figure 38.

Notice that the grain boundary segregation results do not vary greatly across different orders of magnitude for a dislocation density in the range $10^{12} /m^2$ to $10^{15} /m^2$ but vary significantly in the range $10^{16} /m^2$ to $10^{17} /m^2$. This is related to the more significant change in vacancy concentration for the latter range as shown in Figure 37.

Figure 37 shows a peak in the vacancy profile for some values of the dislocation density in the MIK model. At the same dislocation density values the chromium profile exhibits a minimum and the nickel profile a maximum versus the dislocation density as shown in Figure 36.

In Figure 38 one notices that the stationary iron grain boundary fractions slightly increases with dislocation density in the Perks model and slightly decreases in the MIK model.

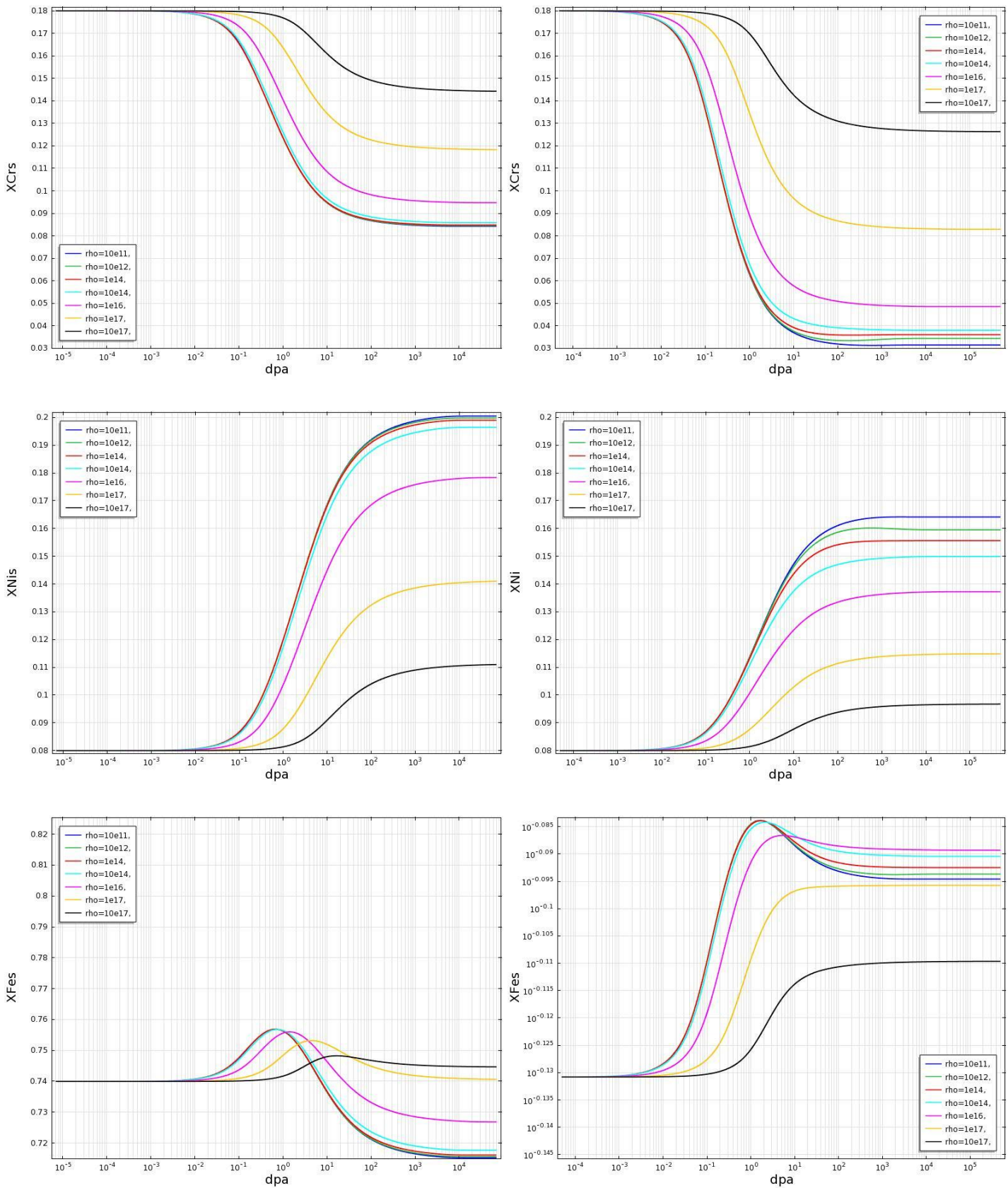


Figure 36 Iron, chromium and nickel grain boundary concentrations for various dislocation densities (in m^{-2}) versus fluence according to the Perks-model (left) and the MIK-model (right).

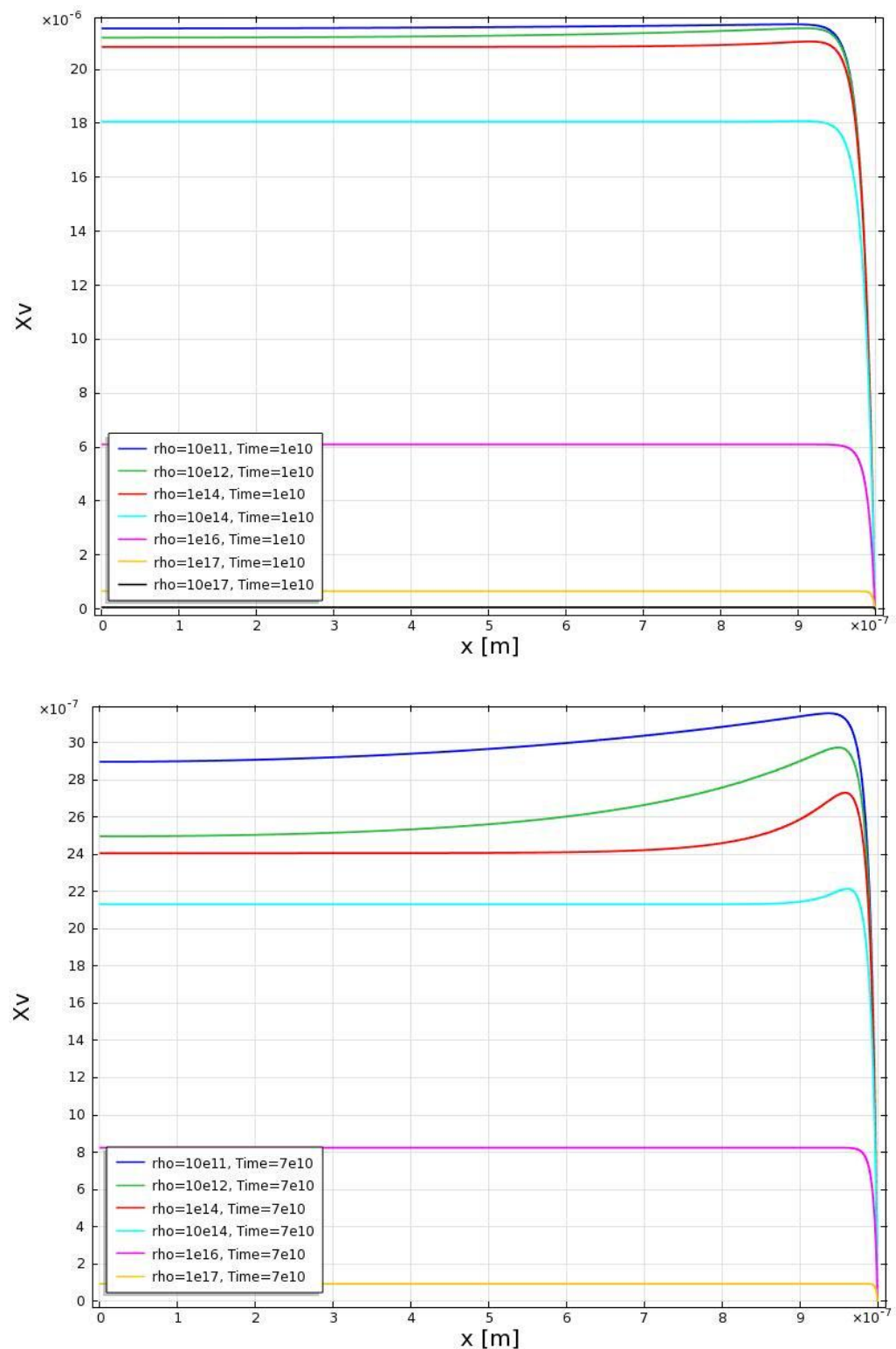


Figure 37 Vacancy profiles for various dislocation densities (in m^{-2}) according to the Perks model (top) and the MIK-model (bottom)

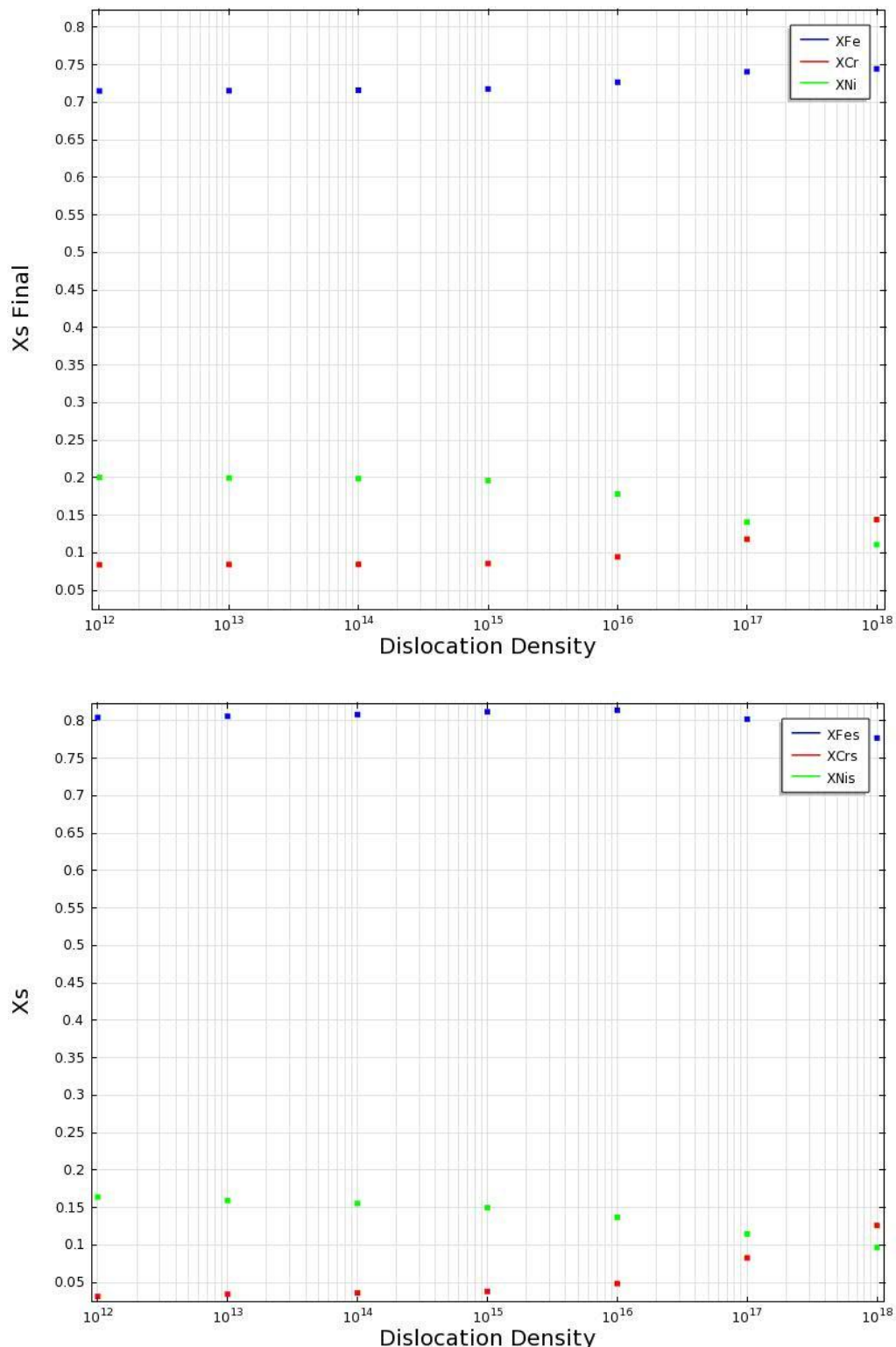


Figure 38 Steady state iron, chromium and nickel grain boundary concentrations for various dislocation densities (in m⁻²) according to the Perks model (top) and the MIK-model (bottom)

3.5 *The effect of neutron flux on grain boundary segregation*

A larger neutron flux through the material equals a higher rate of Frenkel pair creation and, hence, one expects a higher vacancy and interstitial density, in turn resulting in higher diffusion coefficients. Figure 39 plots the vacancy concentration profile and shows that for both the Perks and the MIK model the interstitial and vacancy concentrations increase with the neutron flux. Figure 40 shows how grain boundary segregation of the various elements takes place more quickly in time at higher flux than at lower flux. Figure 41 shows that at a fixed fluence, the segregation of the elements is more advanced for smaller fluxes than for larger fluxes. Thus, although the segregation will occur faster in time at higher fluxes, there is a larger fluence required to achieve the same degree of segregation. This is because the flux dependence of the segregation rate is less than linear. In other words, on doubling the flux the rate of segregation is increased but not doubled.

It is noteworthy that although the diffusion coefficients for the various elements increases with the flux, the final degree of segregation after prolonged irradiation is smaller. Apparently, it is not only the magnitude of the diffusion coefficients that determines the level of segregation, but also the magnitude of the defect concentrations.

As mentioned previously, the grain boundary fraction of iron initially increases and then decreases. The maximum in iron enrichment will be reached faster at a higher flux as shown in Figure 40 but at a larger fluence as shown in Figure 41.

Figure 42 shows that the grain boundary fraction of iron in the stationary state increases with increasing flux for the Perks model but that for the MIK model it first increases and then decreases.

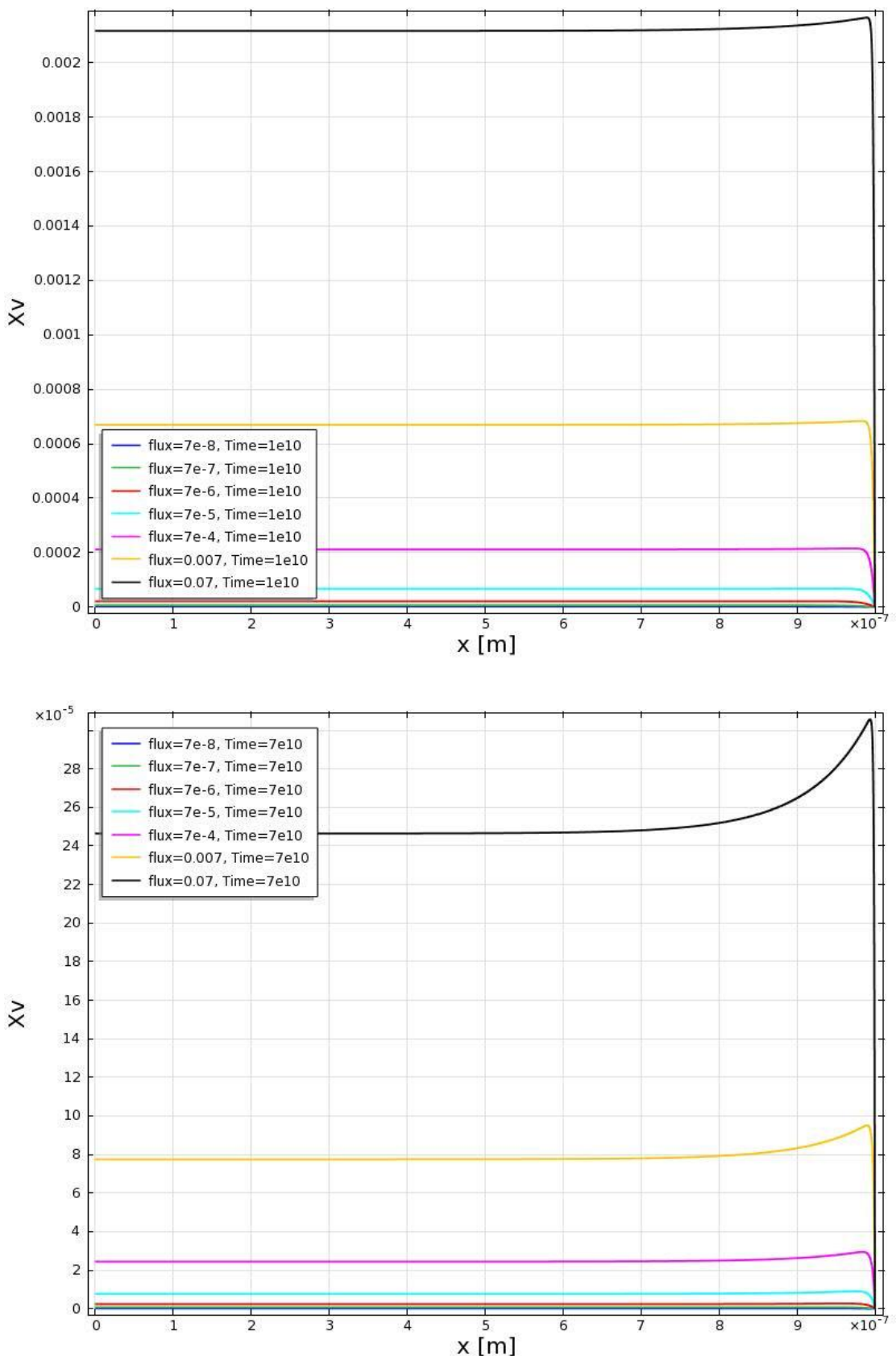


Figure 39 Vacancy profiles for various values of the neutron fluxes (in dpa/s) according to the Perks model (top) and the MIK-model (bottom)

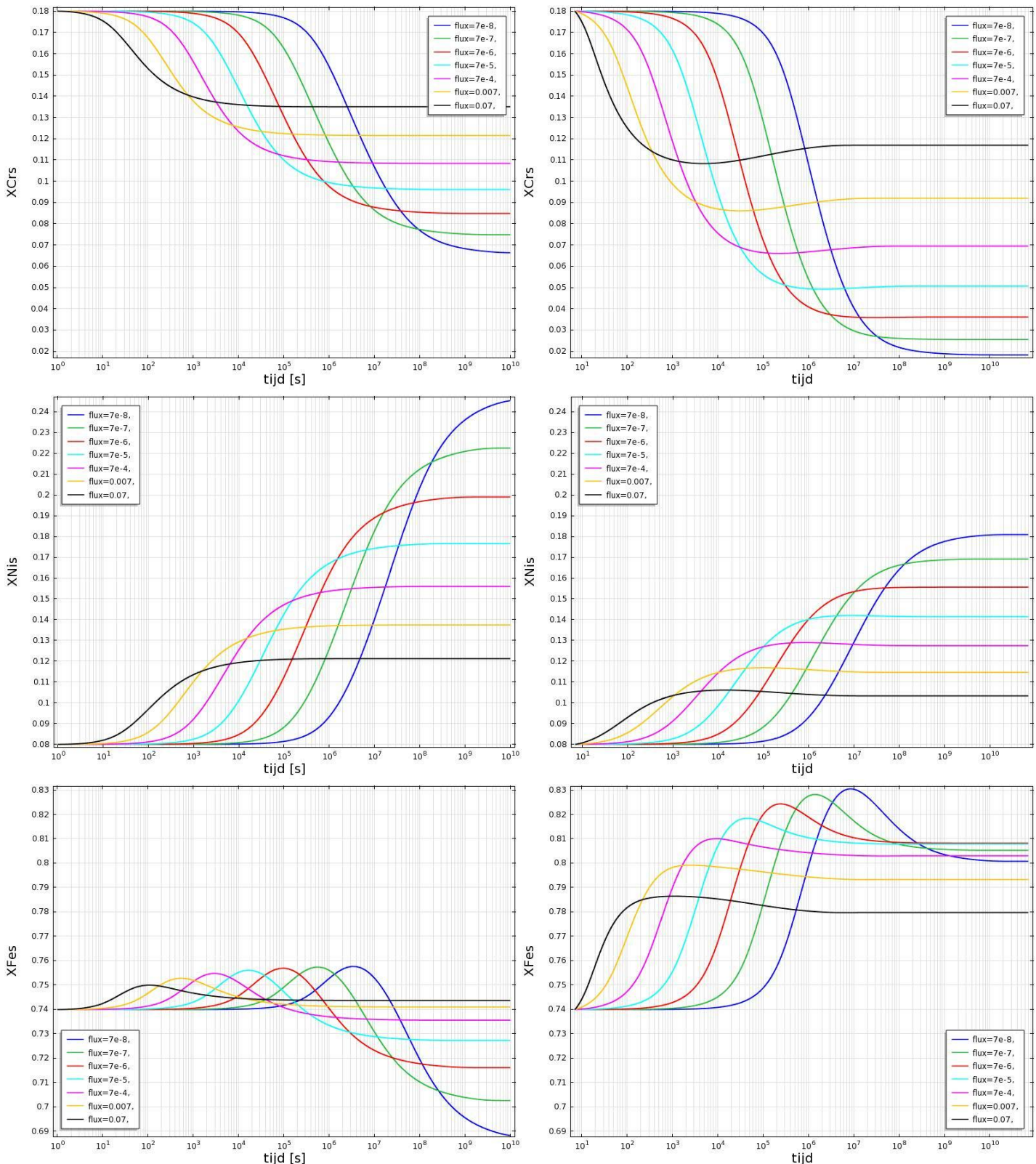


Figure 40 Iron, chromium and nickel grain boundary concentrations for various values of the neutron fluxes (in dpa/s) versus time according to the Perks-model (left) and the MIK-model (right).

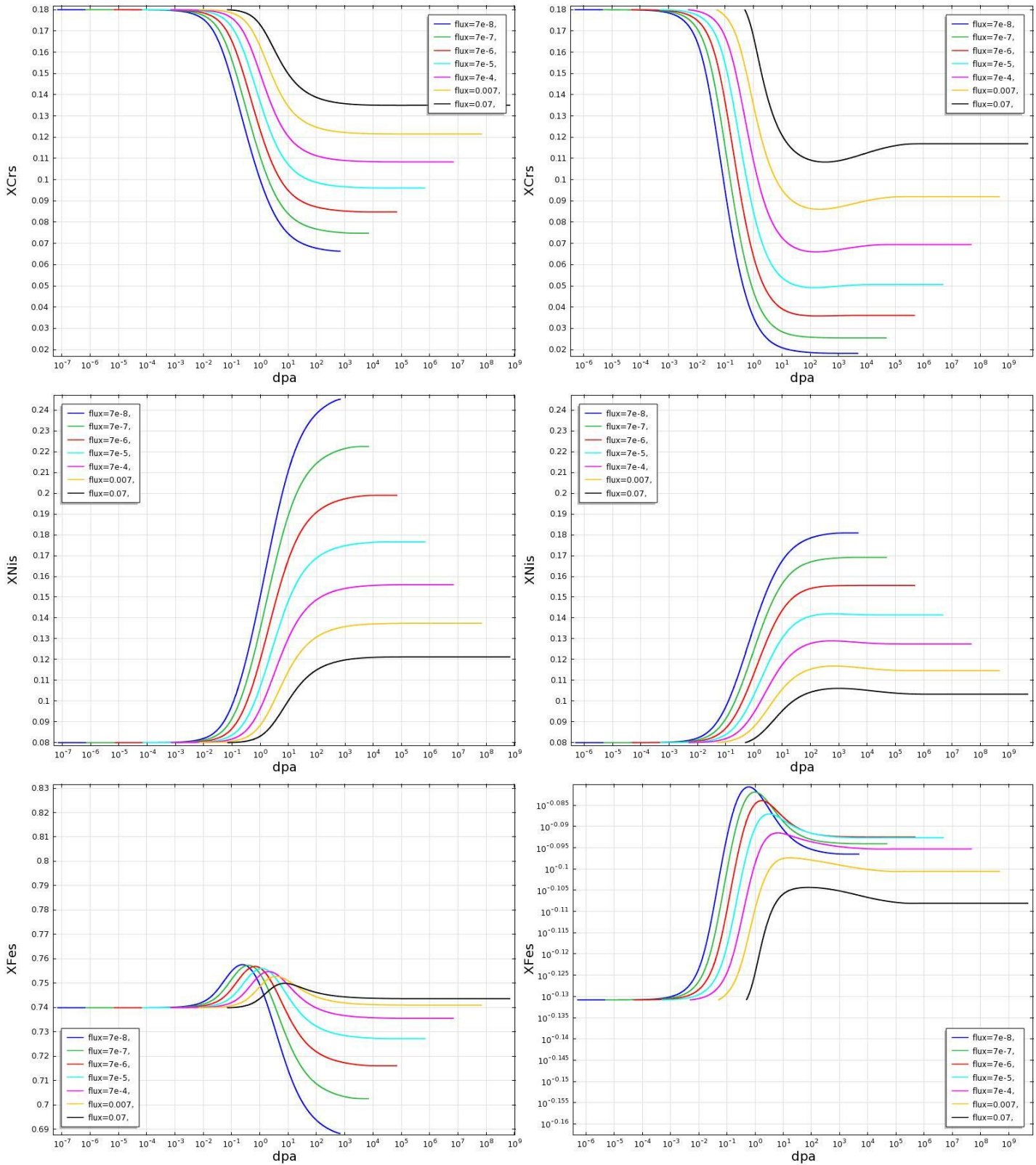


Figure 41 Iron, chromium and nickel grain boundary concentrations for various values of the neutron fluxes (in dpa/s) versus fluence according to the Perks-model (left) and the MIK-model (right).

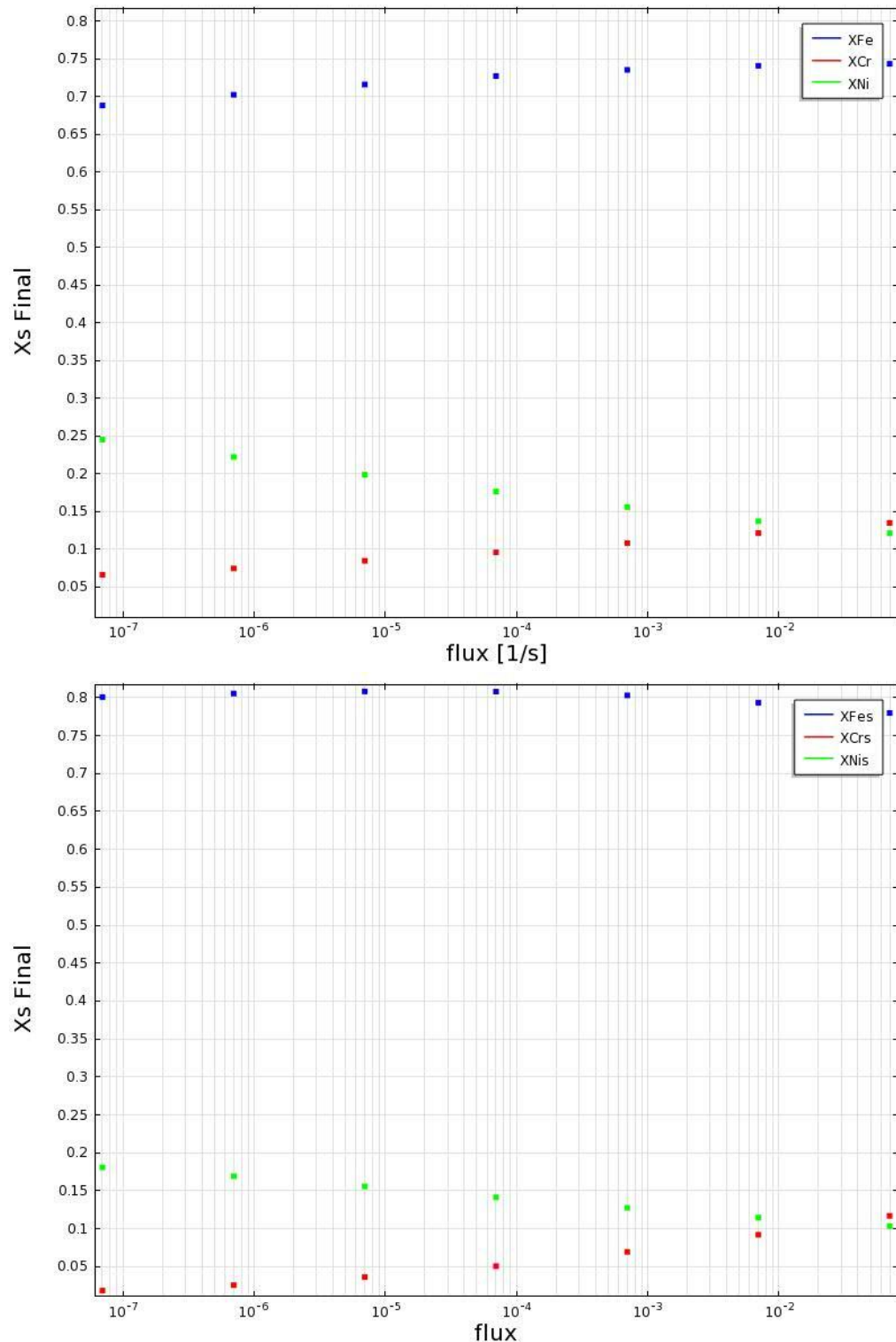


Figure 42 Steady state iron, chromium and nickel grain boundary concentrations for various values of the neutron fluxes (in dpa/s) according to the Perks model (top) and the MIK-model (bottom)

4 Comparison with literature

In the previous section on trend calculations we chose one area around the grain boundary over which we averaged the atom fractions and defect concentrations in order to make the results grain boundary mesh size independent. An additional argument for doing the averaging was that experimental measurements anyway cannot measure with infinite precision for they have a spot size from which they obtain information. However, averaging is but an approximation of the weighted averaging that happens in experimental measurements. Each measurement technique is in fact characterized by a so-called intensity profile derived from the X-ray beam or electron beam with which the measurement is carried out and this intensity profile is different for different measurement techniques. The intensity profile determines to what extent points around the grain boundary will contribute to the measured value. This is in fact proportional to the intensity of the beam at that location.

In what follows, we examine successively the intensity profiles for STEM measurements (Scanning Transmission Electron Microscopy) and for AES measurements (Auger Electron Spectroscopy) and determine how to weigh the calculated fractions close to the grain boundary in order to compare the result to experimental measurements. Next, we compare the calculated values with experimental values from [1].

4.1 Comparison with STEM measurements

The STEM measurement is accompanied by an intensity profile that in good approximation can be represented by a Gauss-profile with a full width at tenth maximum (FWTM) of 2.0 nm [5]. The expression is

$$g(x) = \frac{1}{N} e^{-\frac{(x-L)^2}{2\sigma^2}} \quad (57)$$

where N is a normalization factor and σ the standard deviation respectively given by

$$N = \int_0^L e^{-\frac{(x-L)^2}{2\sigma^2}} dx \quad (58)$$

$$\sigma = \frac{1}{\sqrt{2\ln(10)}} nm \quad (59)$$

Integration is performed over the grain with radius L, a distance also used in the normalization. The measured concentration of element i, C_i , will correspond to the convolution of the intensity profile with the actual concentration profile of element i, $c_i(x)$

$$C_i = \int_0^L c_i(x) g(x) dx \quad (60)$$

When one performs convolution on a calculated concentration profile, one should obtain a value that corresponds to the value from the STEM measurement.

4.2 Comparison with AES measurements

The intensity profile of an AES measurement is mainly determined by the depth resolution of the Auger electron escape depth, $\varepsilon_{D,i}$. This escape depth determines the slope of the exponential decay of the Auger electron intensity, and is expressed in a number of monolayers according to the empirically determined formula [6]:

$$\varepsilon_{D,i} = \left(\frac{538}{E_i^2} + 0,41\sqrt{aE_i} \right) \cdot \cos(\Theta) \quad (61)$$

E_i is the Auger electron energy of element i in eV, $\cos(\Theta)$ is a geometric factor relating to the electron escape angle and the angle of detection of the measuring instrument, and a the monolayer thickness. The escape depth for chromium is 3.6 monolayers and for nickel 4.2 monolayers, where the monolayer thickness is 0.225 nm [5]. On the basis of the Auger electron energies of chromium, nickel and iron, one can determine the escape depth of iron, using equation (61), to be 3.9 monolayers.

The intensity profile corresponding to an AES measurement of an element i , is given by

$$g_i(x) = e^{-\frac{L-x}{\varepsilon_{D,i}}} \quad (62)$$

The measured concentration of element i , C_i , will correspond to the convolution of the intensity profile with the actual concentration profile of element i , $c_i(x)$

$$C_i = \frac{1}{N} \frac{\int_0^L g_i(x)c_i(x)dx}{\int_0^L g_i(x)dx} \quad (63)$$

where N is a normalization factor which ensures that the sum of the measured fractions is 1

$$N = \sum_k \left[\frac{\int_0^L g_k(x)c_k(x)dx}{\int_0^L g_k(x)dx} \right] \quad (64)$$

4.3 Comparison with experimental data

Table 3 lists the compositions of the various alloys for which measured and calculated grain boundary concentration will be compared. Table 4 and Table 5 show the measured grain boundary concentration from either AES or STEM measurements, along with the concentrations as calculated according to MIK and Perks models. More information related to the description of the experiment can be found in [78].

Legering	Cr	Ni	Fe	Mn	Mo	Si	C	N	P	S
Fe-16Cr-24Ni	15,80	22,83	59,93	1,30	<0,02	0,12	0,02	-	<0,01	<0,01
	16,03	23,16	60,81							
Fe-20Cr-24Ni	20,07	23,24	55,49	1,16	0,02	<0,01	0,01	-	<0,01	<0,009
	20,31	23,52	56,17							
Fe-24Cr-24Ni	25,62	22,18	50,65	1,40	0,001	0,12	0,02	0,004	0,01	<0,009
	26,02	22,53	51,45							
Fe-24Cr-19Ni	26,29	17,49	54,85	1,22	<0,01	0,02	0,03	0,004	0,01	<0,009
	26,66	17,73	55,61							
Fe-20Cr-9Ni	20,72	8,88	69,16	1,11	<0,01	0,09	0,021	0,012	0,01	<0,009
	20,97	8,99	70,04							
Ni-18Cr	18,24	81,74	0	0	0,002	0	0,005	-	0,006	0,004
	18,24	81,76	0							
Ni-18Cr-9Fe	18,26	72,36	9,32	0,010	0,002	0,027	0,014	-	0,007	0,004
	18,26	72,40	9,33							

Table 3 Composition of the alloys from [7]. The second line gives the normalized values assuming Fe + Cr + Ni = 100%.

Meting	Legering	Temp [°C]	dpa	XFe	XCr	XNi	XFe MIK	XFe Perks	XCr MIK	XCr Perks	XNi MIK	XNi Perks
AES	Fe-20Cr-9Ni		0,0	0,687±0,003	0,232±0,004	0,081±0,001	0,7004	0,7004	0,1797	0,1797	0,0899	0,0899
AES	Fe-20Cr-9Ni	400	0,1	0,694±0,002	0,214±0,003	0,092±0,002	0,7541	0,7148	0,1211	0,1537	0,1046	0,1058
AES	Fe-20Cr-9Ni	400	1,0	0,703±0,002	0,170±0,002	0,127±0,002	0,7921	0,7170	0,0571	0,1106	0,1413	0,1540
AES	Fe-20Cr-9Ni	400	3,0	0,664±0,004	0,090±0,004	0,246±0,006	0,7899	0,7050	0,0424	0,0941	0,1607	0,1852
AES	Fe-20Cr-24Ni	200	1,0	0,535±0,008	0,208±0,006	0,258±0,008	0,6096	0,5602	0,1026	0,1755	0,2706	0,2643
AES	Fe-20Cr-24Ni	300	0,5	0,537±0,006	0,193±0,007	0,270±0,004	0,6170	0,5536	0,0788	0,1544	0,2190	0,2920
AES	Fe-20Cr-24Ni	400	0,5	0,520±0,010	0,136±0,003	0,345±0,010	0,6133	0,5368	0,0580	0,1284	0,3190	0,3348
AES	Fe-20Cr-24Ni	500	0,5	0,484±0,012	0,130±0,009	0,386±0,005	0,6039	0,5239	0,0499	0,1154	0,3378	0,3607
AES	Fe-20Cr-24Ni	600	0,5	0,552±0,004	0,179±0,003	0,268±0,005	0,5991	0,5231	0,0584	0,1144	0,3328	0,3625
AES	Fe-20Cr-24Ni	700	0,5	-	-	-	0,5773	0,5459	0,1331	0,1559	0,2673	0,2982
AES	Fe-20Cr-24Ni	400	0,1	0,552±0,003	0,180±0,002	0,269±0,003	0,6034	0,5596	0,1071	0,1681	0,2716	0,2724
AES	Fe-20Cr-24Ni	400	0,5	0,520±0,010	0,136±0,003	0,345±0,010	0,6133	0,5368	0,0580	0,1284	0,3190	0,3348
AES	Fe-20Cr-24Ni	400	1,0	0,519±0,007	0,121±0,004	0,360±0,008	0,6074	0,5189	0,0440	0,1121	0,3412	0,3690
AES	Fe-20Cr-24Ni	400	3,0	0,476±0,009	0,141±0,006	0,384±0,011	0,5926	0,4867	0,0313	0,0920	0,3709	0,4213
AES	Fe-16Cr-24Ni	400	1,0	0,505±0,007	0,107±0,004	0,389±0,010	0,6331	0,5536	0,0310	0,0745	0,3307	0,4020
AES	Fe-24Cr-24Ni	400	1,0	0,498±0,005	0,147±0,005	0,354±0,007	0,5868	0,4897	0,0664	0,1274	0,3358	0,3617
AES	Fe-24Cr-19Ni	400	1,0	0,571±0,004	0,172±0,007	0,129±0,003	0,6434	0,5487	0,0732	0,1362	0,2712	0,2924
STEM	Fe-20Cr-9Ni	-	0,0	0,687±0,001	0,211±0,001	0,091±0,001	0,7004	0,7004	0,2097	0,2097	0,0899	0,0899
STEM	Fe-20Cr-9Ni	400	0,1	0,699±0,001	0,199±0,001	0,095±0,001	0,7716	0,7179	0,1153	0,1663	0,1130	0,1158
STEM	Fe-20Cr-9Ni	400	0,5	0,700±0,002	0,189±0,002	0,103±0,002	0,7949	0,7161	0,0606	0,1275	0,1445	0,1564
STEM	Fe-20Cr-9Ni	400	1,0	0,715±0,010	0,171±0,002	0,110±0,002	0,7939	0,7085	0,0461	0,1128	0,1600	0,1787
STEM	Fe-20Cr-9Ni	400	3,0	0,703±0,008	0,138±0,003	0,155±0,008	0,7850	0,6901	0,0331	0,0948	0,1819	0,2151
STEM	Fe-20Cr-24Ni	-	0,0	0,554±0,001	0,201±0,001	0,233±0,001	0,5617	0,5617	0,2031	0,2031	0,2351	0,2352
STEM	Fe-20Cr-24Ni	400	0,5	0,523±0,005	0,140±0,003	0,326±0,007	0,5905	0,5157	0,0535	0,110	0,3559	0,3743
STEM	Fe-20Cr-24Ni	400	1,0	0,506±0,005	0,140±0,002	0,351±0,007	0,5793	0,4927	0,0408	0,0945	0,3799	0,4128
STEM	Fe-20Cr-24Ni	400	3,0	0,517±0,003	0,145±0,001	0,334±0,004	0,5597	0,4552	0,0291	0,0762	0,4113	0,4685

Table 4 Experimentally measured and calculated grain boundary concentrations for the iron-based alloys of [7] according to the Perks and MIK model. Proton irradiation with an energy of 3.2 MeV and a flux of 7×10^{-6} dpa/s.

Meting	Legering	Temp [°C]	dpa	XFe	XCr	XNi	XFe MIK	XFe Perks	XCr MIK	XCr Perks	XNi MIK	XNi Perks
AES	Ni-18Cr	200	0,5	-	0,146±0,002	0,854±0,002	-	-	0,0737	0,1339	0,9140	0,8438
AES	Ni-18Cr	300	0,5	-	0,115±0,002	0,885±0,002	-	-	0,0453	0,0966	0,9472	0,8873
AES	Ni-18Cr	400	0,5	-	0,101±0,002	0,899±0,002	-	-	0,0335	0,0724	0,9609	0,9156
AES	Ni-18Cr	500	0,5	-	0,129±0,005	0,871±0,005	-	-	0,0298	0,0598	0,9652	0,9302
AES	Ni-18Cr	600	0,5	-	-	-	-	-	0,0540	0,0576	0,9369	0,9327
AES	Ni-18Cr	700	0,5	-	-	-	-	-	0,1348	0,0945	0,8427	0,8897
AES	Ni-18Cr	400	0,0	-	0,171±0,002	0,829±0,002	-	-	0,1563	0,1563	0,8176	0,8176
AES	Ni-18Cr	400	0,1	-	0,134±0,003	0,866±0,003	-	-	0,0733	0,1119	0,9145	0,8695
AES	Ni-18Cr	400	0,3	-	0,118±0,002	0,882±0,002	-	-	0,0431	0,0724	0,9497	0,9156
AES	Ni-18Cr	400	0,5	-	0,101±0,002	0,899±0,002	-	-	0,0335	0,0592	0,9609	0,9310
AES	Ni-18Cr	400	1,0	-	0,106±0,003	0,894±0,003	-	-	0,0247	0,0450	0,9711	0,9476
STEM	Ni-18Cr	400	0,0	-	0,188±0,002	0,812±0,002	-	-	0,1824	0,1824	0,8176	0,8176
STEM	Ni-18Cr	400	0,1	-	0,157±0,002	0,843±0,002	-	-	0,0591	0,1104	0,9409	0,8896
STEM	Ni-18Cr	400	0,3	-	0,143±0,003	0,857±0,003	-	-	0,0315	0,0657	0,9685	0,9343
STEM	Ni-18Cr	400	0,5	-	0,130±0,003	0,870±0,003	-	-	0,0239	0,0528	0,9761	0,9472
STEM	Ni-18Cr	400	1,0	-	0,136±0,003	0,864±0,003	-	-	0,0173	0,0397	0,9827	0,9603
AES	Ni-18Cr-9Fe	200	0,5	0,067±0,005	0,157±0,002	0,776±0,005	0,1051	0,0895	0,0775	0,1356	0,8045	0,7523
AES	Ni-18Cr-9Fe	300	0,5	0,054±0,005	0,138±0,003	0,808±0,006	0,1054	0,0796	0,0474	0,1007	0,8393	0,8029
AES	Ni-18Cr-9Fe	400	0,5	0,058±0,003	0,135±0,002	0,807±0,005	0,1011	0,0700	0,0348	0,0762	0,8584	0,8411
AES	Ni-18Cr-9Fe	500	0,5	0,065±0,003	0,157±0,002	0,778±0,005	0,0963	0,0641	0,0306	0,0638	0,8679	0,8615
AES	Ni-18Cr-9Fe	600	0,5	-	-	-	0,0951	0,0632	0,0509	0,0619	0,8455	0,8646
AES	Ni-18Cr-9Fe	700	0,5	-	-	-	0,0938	0,0769	0,1318	0,0987	0,7525	0,8080
AES	Ni-18Cr-9Fe	400	0,0	0,094±0,003	0,180±0,004	0,726±0,005	0,0933	0,0933	0,1565	0,1565	0,7241	0,7241
AES	Ni-18Cr-9Fe	400	0,1	0,052±0,002	0,139±0,002	0,809±0,003	0,1014	0,0844	0,0752	0,1150	0,8109	0,7813
AES	Ni-18Cr-9Fe	400	0,3	0,049±0,003	0,139±0,004	0,811±0,004	0,1018	0,0700	0,0446	0,0762	0,8461	0,8411
AES	Ni-18Cr-9Fe	400	0,5	0,058±0,003	0,135±0,002	0,807±0,005	0,1011	0,0631	0,0348	0,0625	0,8584	0,8640
AES	Ni-18Cr-9Fe	400	1,0	0,055±0,003	0,138±0,003	0,807±0,006	0,0996	0,0541	0,0257	0,0481	0,8705	0,8898
STEM	Ni-18Cr-9Fe	400	0,0	0,092±0,001	0,179±0,002	0,728±0,002	0,0933	0,0933	0,1826	0,1826	0,7241	0,7241
STEM	Ni-18Cr-9Fe	400	0,1	0,066±0,001	0,160±0,002	0,774±0,003	0,1022	0,0787	0,0612	0,1150	0,8367	0,8063
STEM	Ni-18Cr-9Fe	400	0,3	0,058±0,001	0,154±0,002	0,787±0,002	0,1007	0,0615	0,0328	0,0701	0,8665	0,8684
STEM	Ni-18Cr-9Fe	400	0,5	0,054±0,001	0,144±0,002	0,802±0,003	0,0993	0,0546	0,0248	0,0565	0,8759	0,8889
STEM	Ni-18Cr-9Fe	400	1,0	0,058±0,002	0,153±0,002	0,787±0,003	0,0972	0,0463	0,0179	0,0429	0,8849	0,9108

Table 5 Experimentally measured and calculated grain boundary concentrations for the nickel-based alloys of [7] according to the Perks and MIK model.
 Proton irradiation with an energy of 3.2 MeV and a flux of 7×10^{-6} dpa/s.

Figure 43 and Figure 44 show a comparison between measured and predicted grain boundary fractions for the iron-based alloys Fe-20Cr-9Ni and Fe-20Cr-24Ni, respectively, after irradiation with protons at a flux of $7 \cdot 10^{-6}$ dpa/s and at a temperature of 400 °C. The predictions of both the Perks and MIK model are shown. Note that the Perks model predicts greater chromium and lower nickel grain boundary fractions. It agrees very well with AES measurements, especially at lower fluence. It agrees a little less well with STEM measurements. The Perks model agrees better with the AES and STEM measurements than the MIK model. The trends observed in the measurements are well reproduced in both models.

Figure 45 and Figure 46 show a comparison between measured and predicted grain boundary fractions for the nickel-based alloys Ni-18Cr and Ni-19Cr-9Fe I, respectively, after irradiation with protons at a flux of $7 \cdot 10^{-6}$ dpa/s and at a temperature of 400 °C. The predictions of both the Perks and MIK model are shown. Note that both models overestimate chromium depletion and nickel enrichment. There does not seem to be a trend with fluence in the measurement grain boundary fractions for the Ni-18Cr-9Fe alloy, apart from the fact that chromium always depletes and nickel always enriches. For the Ni-18Cr alloy the measurement grain boundary fractions, both AES and STEM, yield a chromium depletion and nickel enrichment trend with fluence. They are not well predicted by the models. However, also in the case of the nickel-based alloys, the Perks model matches more closely the measured values grain boundary fractions.

The predictions for the nickel-based alloys are worse than for the iron-based alloys.

Figure 47 shows the calculated versus the measured grain boundary fractions as listed in Table 4 and Table 5. There clearly is a systematic overestimation of chromium depletion for both the MIK and Perks model, be it a bit less for the latter. There is a slight overestimation of the iron grain boundary fraction for the MIK model. These conclusions hold in respect of both the STEM and AES measurements.

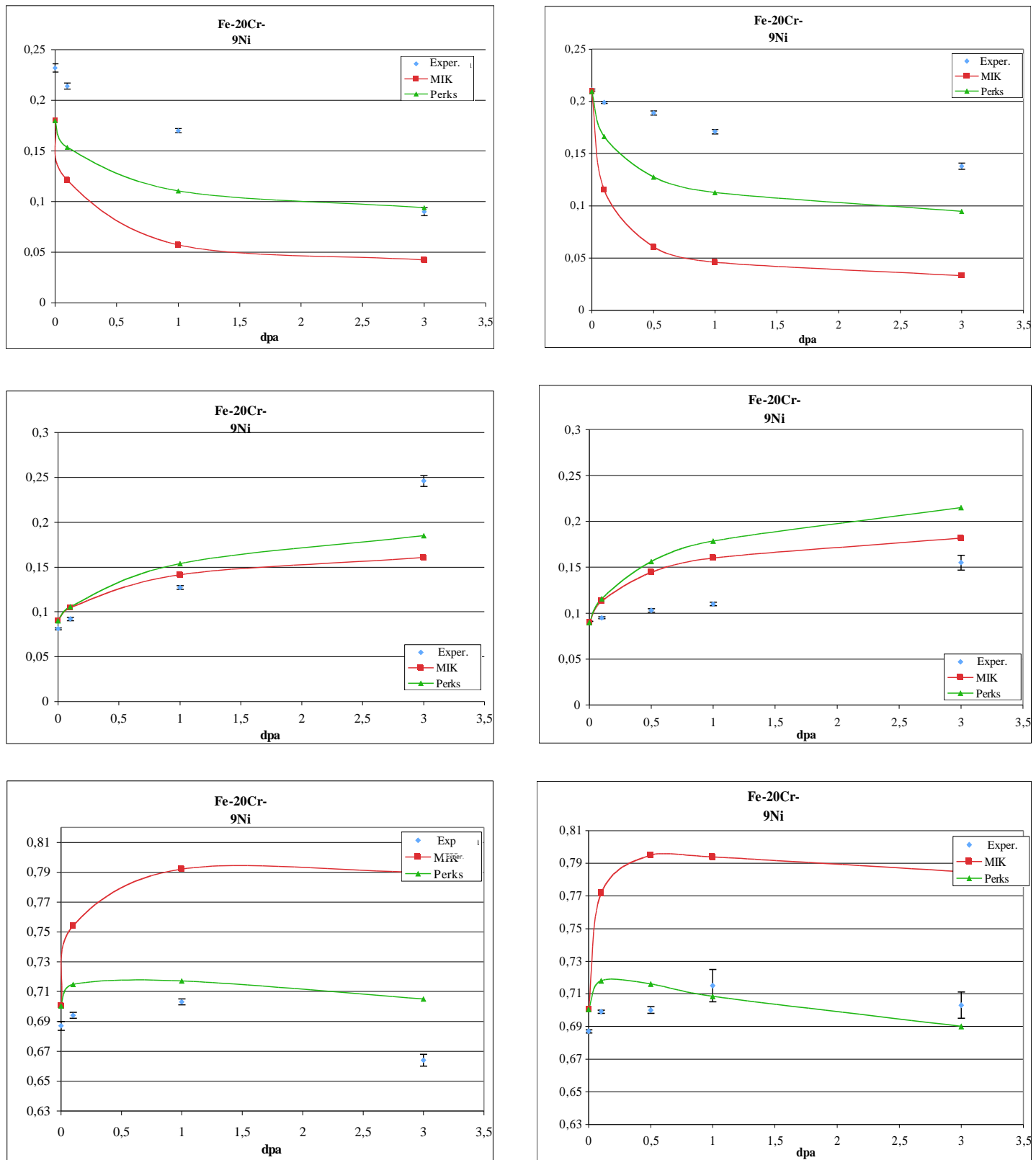


Figure 43 Comparison between measured and calculated grain boundary concentrations for chromium (top), nickel (middle) and iron (bottom) versus fluence for Fe-20Cr-9Ni; AES (left) (left) and STEM (right). Proton flux $7 \cdot 10^{-6}$ dpa/s at 400°C.

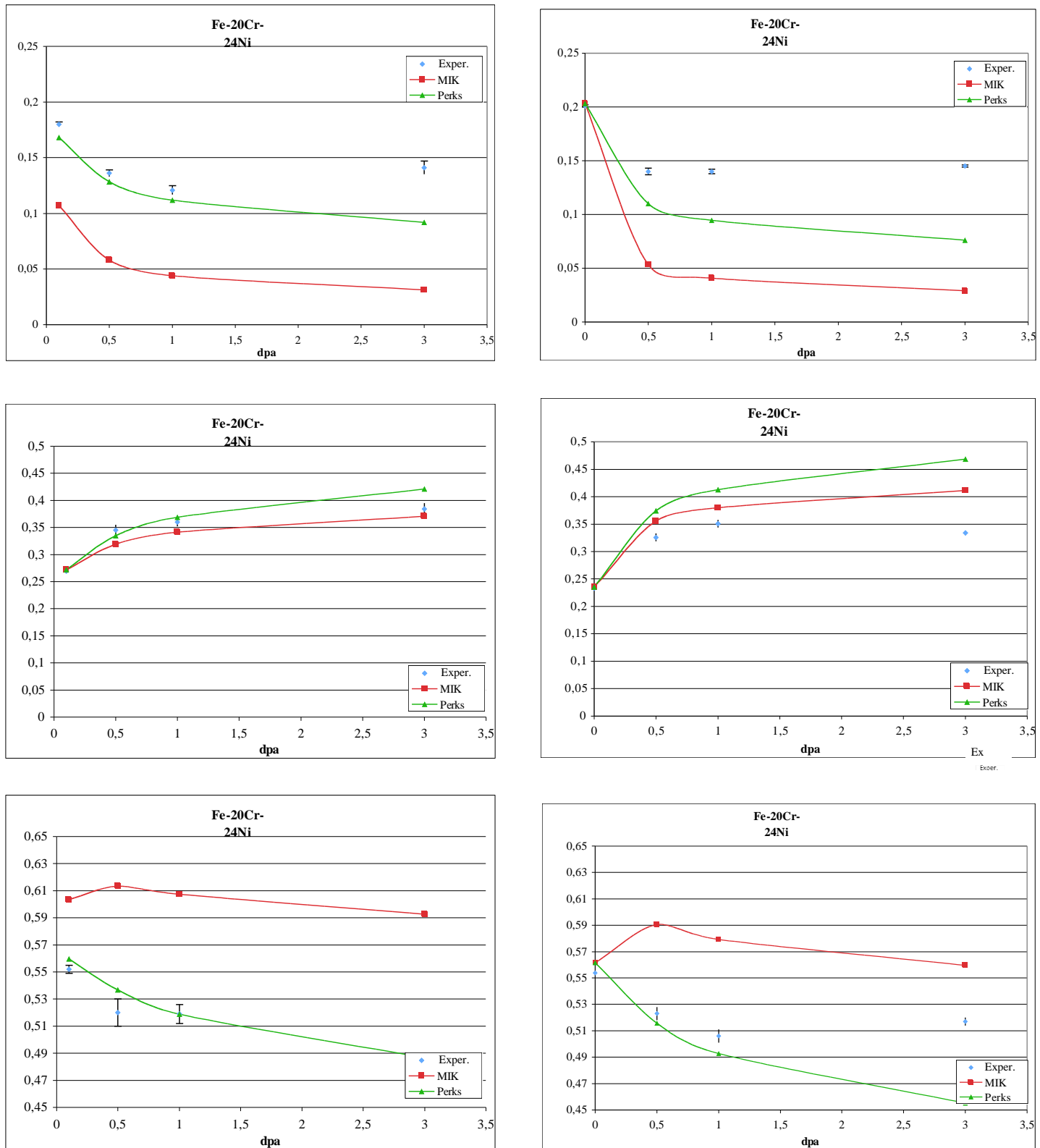


Figure 44 Comparison between measured and calculated grain boundary concentrations for chromium (top), nickel (middle) and iron (bottom) versus fluence for Fe-20Cr-24Ni; AES (left) (left) and STEM (right). Proton flux $7 \cdot 10^{-6}$ dpa/s at 400°C.

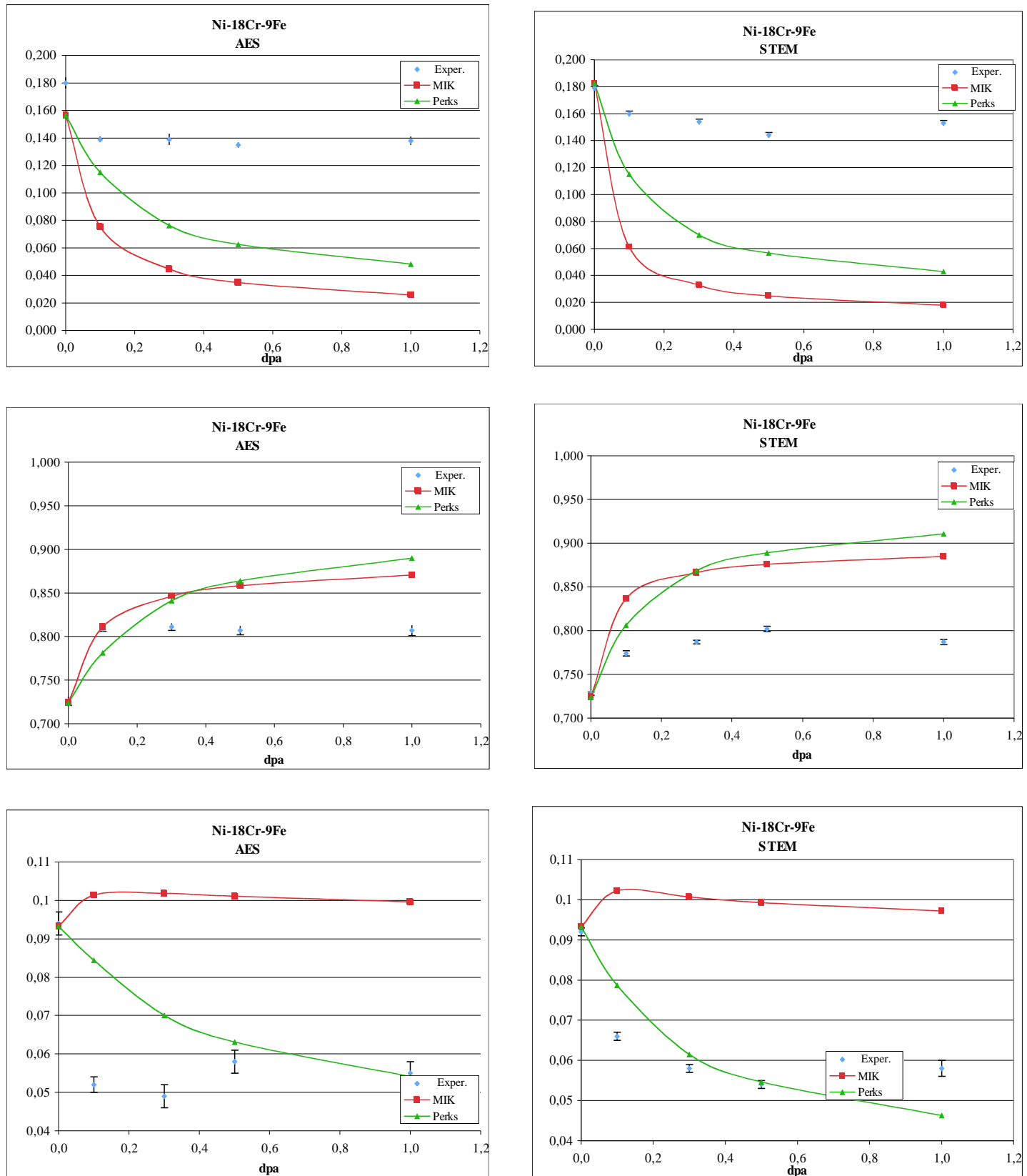


Figure 45 Comparison between measured and calculated grain boundary concentrations for chromium (top), nickel (middle) and iron (bottom) versus fluence for Ni-18Cr-9Fe; AES (left) (left) and STEM (right). Proton flux $7 \cdot 10^{-6}$ dpa/s at 400°C.

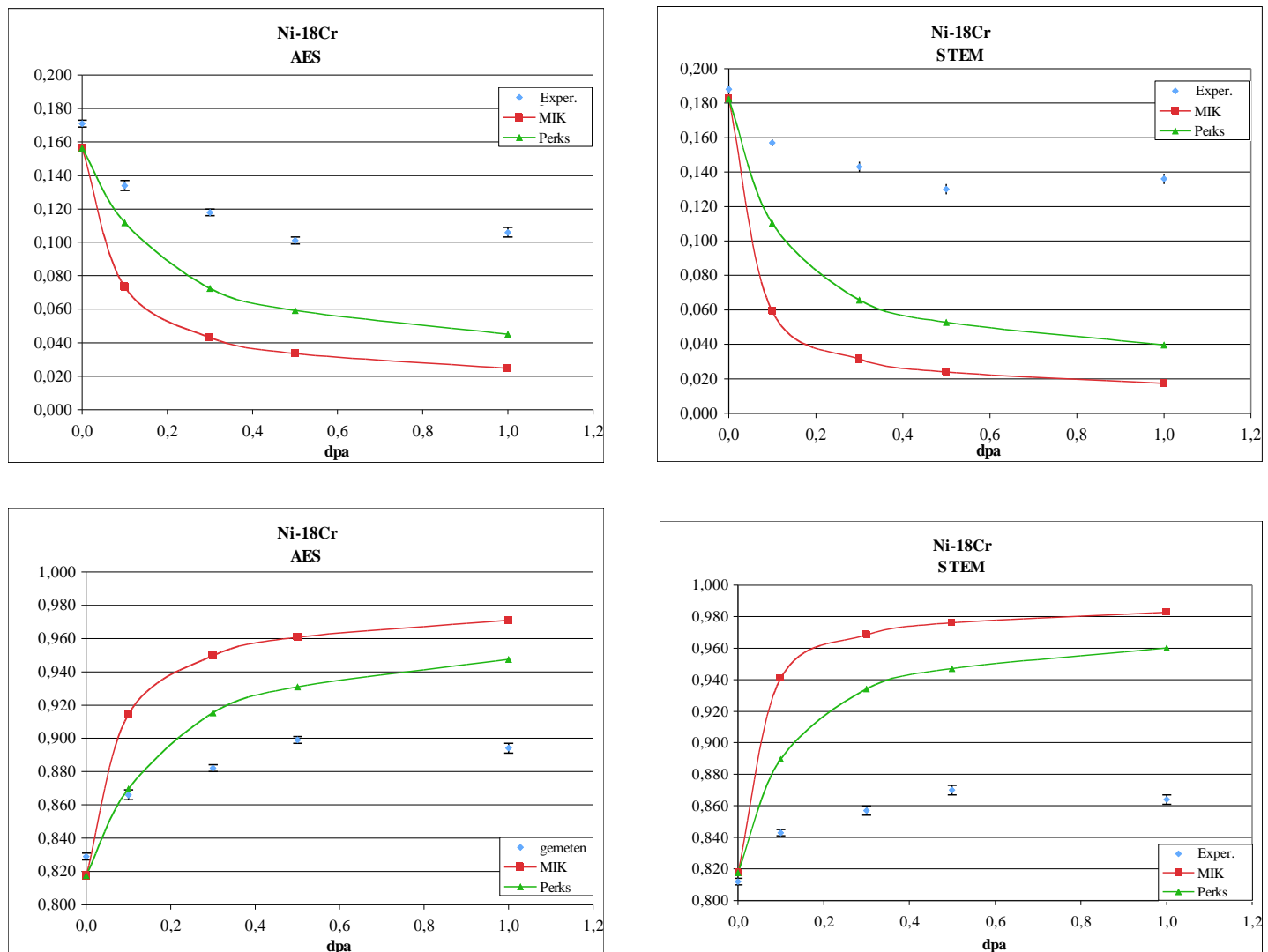


Figure 46 Comparison between measured and calculated grain boundary concentrations for chromium (top) and nickel (bottom) versus fluence for Ni-18Cr; AES (left) (left) and STEM (right). Proton flux $7 \cdot 10^{-6}$ dpa/s at 400°C.

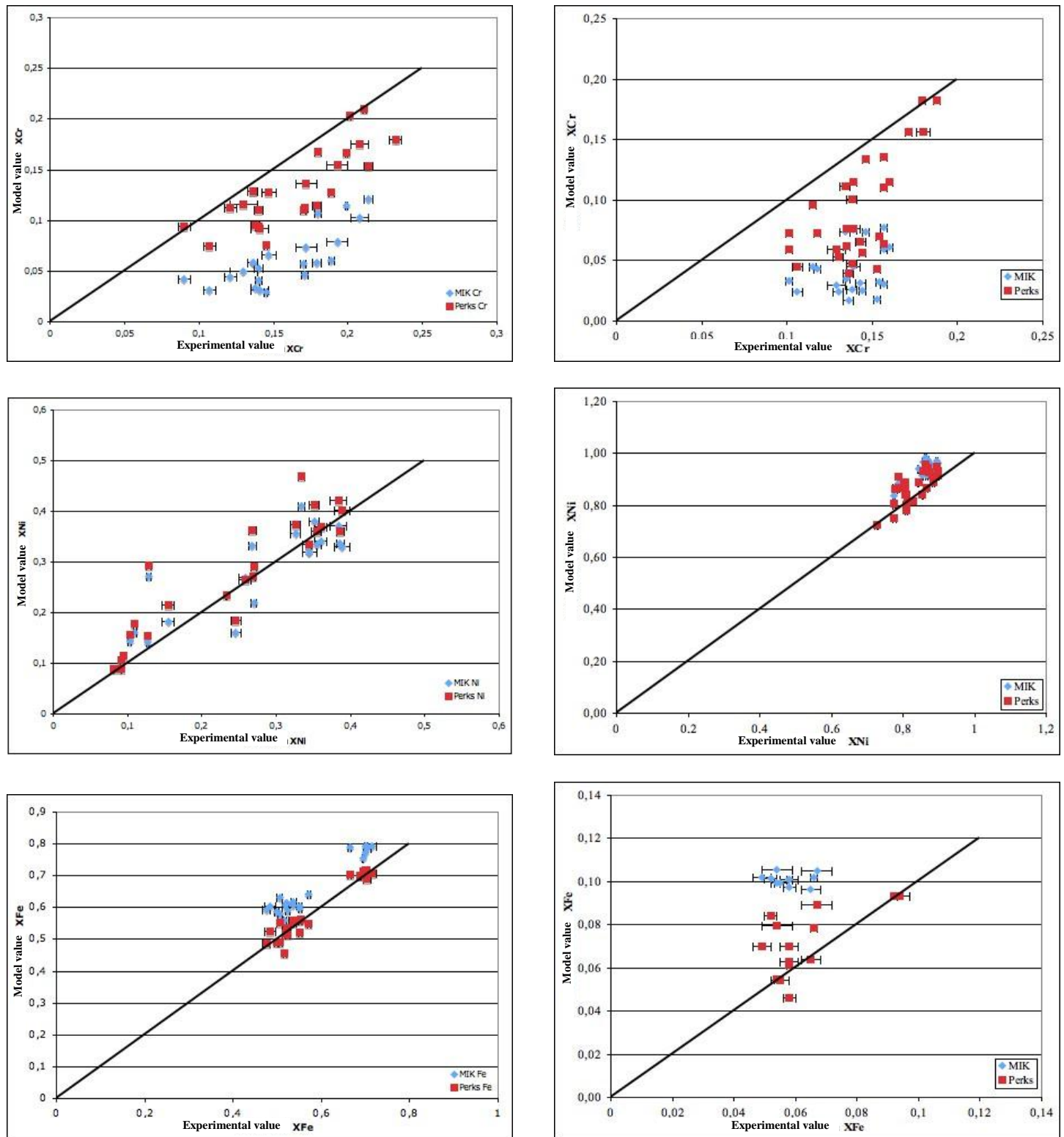


Figure 47 Calculated versus measured grain boundary fractions for chromium (top), nickel (middle) and iron (bottom) for the iron-based alloys (left) and the nickel-based alloys (right).
The one-to-one line is shown in black.

Figure 48 and Figure 49 show a comparison of AES-measured and predicted grain boundary fractions versus irradiation temperature for the Ni-18Cr, Ni-18Cr-9Fe and Fe-20Cr-24Ni alloys, after irradiations with proton at a flux of $7 \cdot 10^{-6}$ dpa/s to a fluence of 0.5 dpa. The predictions of both the Perks and MIK model are shown. The figures show a minimum in the grain boundary chromium fraction with temperature and a maximum in grain boundary nickel fraction with temperature for the AES-measured and the Perks- and MIK-calculated values. For the nickel-based alloy the extrema are predicted at higher temperatures than measured. For the iron-based alloys the extrema are predicted close to the same temperature as measured for both the Perks and MIK model. With the exception of the nickel concentration in the Fe-20Cr-24Ni alloy, the Perks model is always a better match to the measured values than the MIK model.

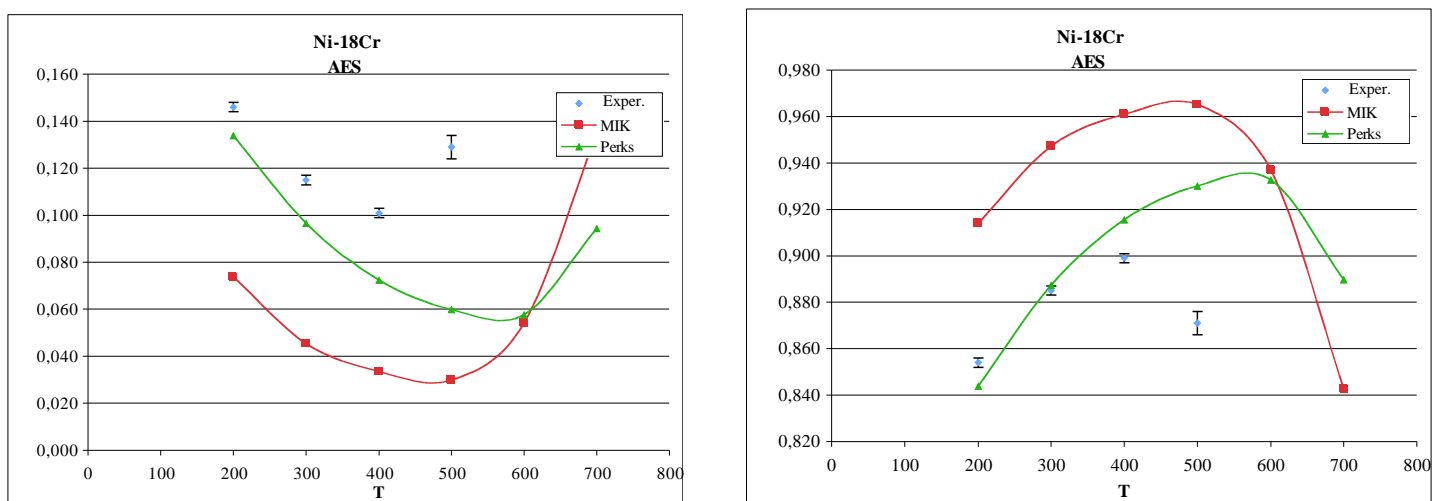


Figure 48 Comparison of measured and predicted grain boundary fractions for chromium and nickel versus temperature in °C for the Ni-18Cr alloy. Proton flux $7 \cdot 10^{-6}$ dpa/s at 400°C

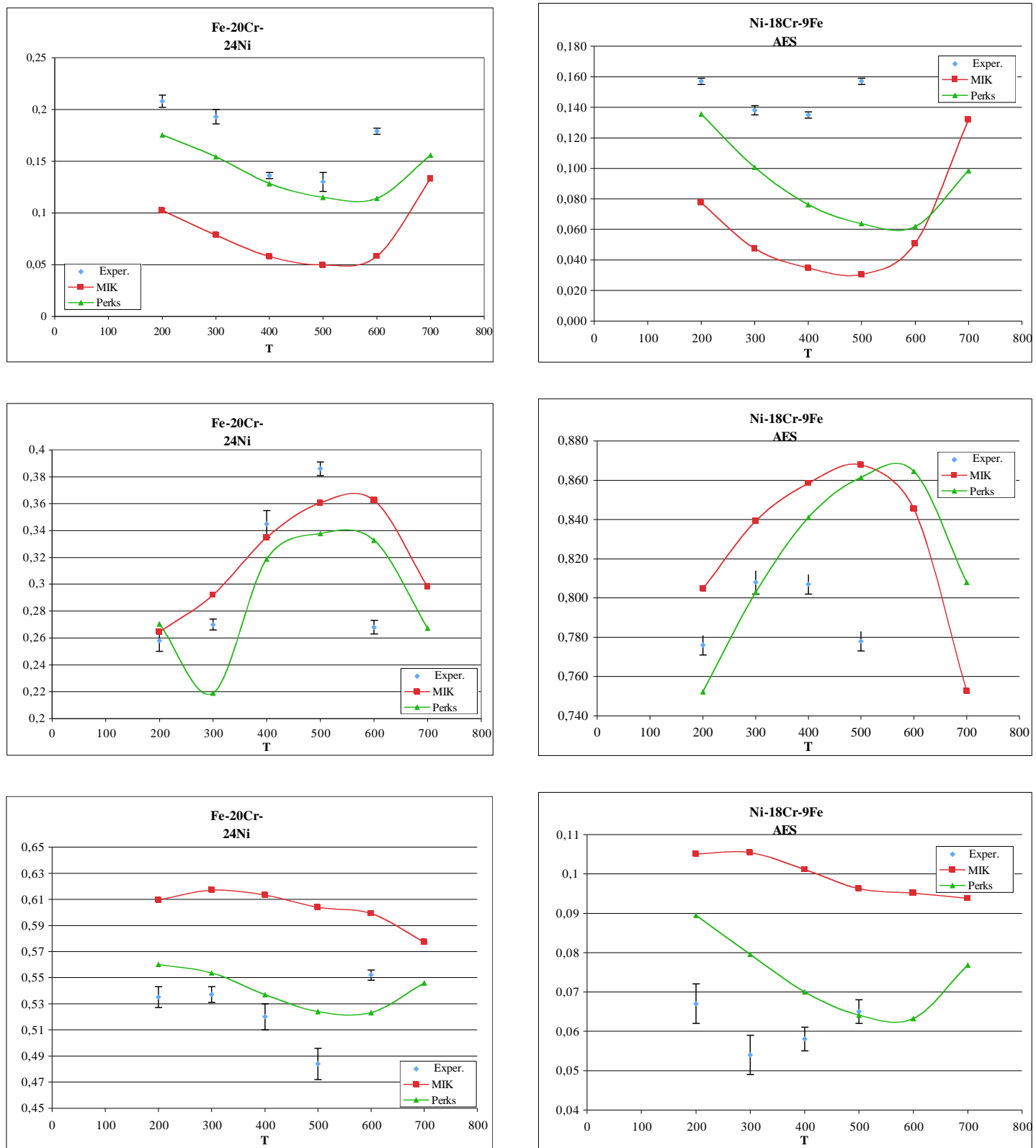


Figure 49 Comparison of measured and predicted grain boundary fractions for chromium, nickel and iron versus temperature in °C for the Fe-20Cr-24Ni alloys (left) and the Ni-18Cr-9Fe alloy (right). Proton flux $7 \cdot 10^{-6}$ dpa/s at 400°C.

4.4 Conclusion on literature comparison

In this section were compared the experimentally measured grain boundary fractions for iron, chromium and nickel with predictions from the MIK and the Perks model. The comparison showed that the trend with fluence, at a given temperature, and the trend with temperature, at a given fluence, are reasonably well reproduced. In general the Perks model matches the experimental measurements closer than the MIK model. This is in contradiction with what is reported in [4] where using the same input data one gets better correspondence with the MIK model. Moreover, our MIK-calculated results do not correspond to those published. This could be related to the damage efficiency factor. Since there is no mentioned of it in the article, we assumed the one as published for the Perks model, i.e. a value 0.1.

5 Two-dimensional calculations with the Perks model

5.1 The 1D Perks model

The derivation of the matrix notation for the Perks model is given in section 2.6 and the final partial differential equation is repeated below. The definition of the partial and total diffusion coefficients is given in section 2.2.4. The latter definition is not repeated here for we will not manipulate it in section 1, contrary to the partial differential equations. Similarly, the boundary conditions are those as given in section 2.5. The system of partial differential equations to be solved is given in equations (65) and (66) below

$$\frac{d\{X\}_{5x1}}{dt} = -\nabla\{J\}_{5x1} + \{S\}_{5x1} \quad (65)$$

$$\{J\}_{5x1} = -[C]_{5x5} \nabla\{X\}_{5x1} \quad (66)$$

Where

$$\{X\}_{5x1} = [X_{Fe} \ X_{Cr} \ X_{Ni} \ X_v \ X_i]^T \quad (67)$$

$$\{J\}_{5x1} = \Omega [J_{Fe} \ J_{Cr} \ J_{Ni} \ J_v \ J_i]^T \quad (68)$$

$$\{S\}_{5x1} = [0 \ 0 \ 0 \ (G_v - RX_v X_i) \ (G_i - RX_v X_i)]^T \quad (69)$$

$$[C]_{5x5} = \begin{bmatrix} \alpha D_{Fe} (1 - X_{Fe}) & -\alpha D_{Cr} X_{Fe} & -\alpha D_{Ni} X_{Fe} & (D_v - d_{Fe}^v) X_{Fe} & 0 \\ -\alpha D_{Fe} X_{Cr} & \alpha D_{Cr} (1 - X_{Cr}) & -\alpha D_{Ni} X_{Cr} & (D_v - d_{Cr}^v) X_{Cr} & 0 \\ -\alpha D_{Fe} X_{Ni} & -\alpha D_{Cr} X_{Ni} & \alpha D_{Ni} (1 - X_{Ni}) & (D_v - d_{Ni}^v) X_{Ni} & 0 \\ -\alpha d_{Fe}^v X_v & -\alpha d_{Cr}^v X_v & -\alpha d_{Ni}^v X_v & D_v & 0 \\ \alpha d_{Fe}^i X_i & \alpha d_{Cr}^i X_i & \alpha d_{Ni}^i X_i & 0 & D_i \end{bmatrix}^1 \quad (70)$$

¹ The zeros in the last column stem from the fact that in the Perks data $d_{Fe}^i = d_{Cr}^i = d_{Ni}^i = D_i$

5.2 The 1D reduced Perks model

The system of partial differential equations given by equations (65) and (66) can be reduced from a 5x5 system to a 4x4 system by eliminating one of the alloy fractions. Indeed,

$$X_{Fe} + X_{Cr} + X_{Ni} = 1 \quad \nabla X_{Fe} + \nabla X_{Cr} + \nabla X_{Ni} = 0 \quad (71)$$

This reduces the number of degrees of freedom of the system and, hence, decreases the calculation time, especially important for 2D calculations (see later). It turns out that the reduction also improves convergence, a welcome bonus.

By eliminating X_{Fe} the reduced system of partial differential equations to be solved is given in equations (72) and (73)

$$\frac{d\{X\}_{4x1}}{dt} = -\nabla\{J\}_{4x1} + \{S\}_{4x1} \quad (72)$$

$$\{J\}_{4x1} = -[C]_{4x4} \nabla\{X\}_{4x1} \quad (73)$$

where

$$\{X\}_{4x1} = [X_{Cr} \ X_{Ni} \ X_v \ X_i]^T \quad (74)$$

$$\{J\}_{4x1} = \Omega [J_{Cr} \ J_{Ni} \ J_v \ J_i]^T \quad (75)$$

$$\{S\}_{4x1} = [0 \ 0 \ (G_v - RX_v X_i) \ (G_i - RX_v X_i)]^T \quad (76)$$

$$[C]_{4x4} = \begin{bmatrix} \alpha D_{Cr} (1 - X_{Cr}) + \alpha D_{Fe} X_{Cr} & -\alpha D_{Ni} X_{Cr} + \alpha D_{Fe} X_{Cr} & (D_v - d_{Cr}^v) X_{Cr} & 0 \\ -\alpha D_{Cr} X_{Ni} + \alpha D_{Fe} X_{Ni} & \alpha D_{Ni} (1 - X_{Ni}) + \alpha D_{Fe} X_{Ni} & (D_v - d_{Ni}^v) X_{Ni} & 0 \\ \alpha (d_{Fe}^v - d_{Cr}^v) X_v & \alpha (d_{Fe}^v - d_{Ni}^v) X_v & D_v & 0 \\ 0 & 0 & 0 & D_i \end{bmatrix} \quad (77)$$

5.3 The 2D reduced Perks model

The 2D, reduced system of partial differential equations to be solved is essentially the same as the 1D, reduced system of partial differential equations as given in equations (72) and (73), apart from the fact that the flux equation has two components. Indeed, the algebraic variables $\{X\}_{4x1}$ and $\{S\}_{4x1}$ are unchanged but the vector quantities $\vec{\nabla}$ and $\{\vec{J}\}_{4x1}$ obtain an x- and y-component. The 2D, reduced system of partial differential equations then reads

$$\frac{d\{X\}_{4x1}}{dt} = -\vec{\nabla}\{\vec{J}\}_{4x1} + \{S\}_{4x1} \quad (78)$$

$$\{\vec{J}\}_{4x1} = -[C]_{4x4} \vec{\nabla}\{X\}_{4x1} \quad (79)$$

where

$$\{\vec{J}\}_{4x1} = \Omega [\vec{J}_{Cr} \ \vec{J}_{Ni} \ \vec{J}_v \ \vec{J}_i]^T \quad (80)$$

5.4 Results with the 2D reduced Perks model

Figure 50 shows the geometry of the 2D model. The horizontal boundaries and the left, vertical boundary are considered to be grain boundaries and the boundary conditions are zero atom flux for iron, chromium and nickel and equilibrium concentrations for vacancies and interstitials. The right, vertical boundary is considered a symmetry boundary with zero fluxes for point defects and atoms. This boundary will in future calculations be interfaced with an oxide film model and the boundary conditions will then be altered. Figure 51 shows a mesh containing 76708 DOF (degrees of freedom).

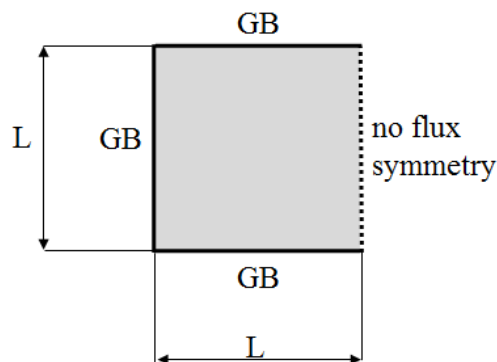


Figure 50 Geometry.

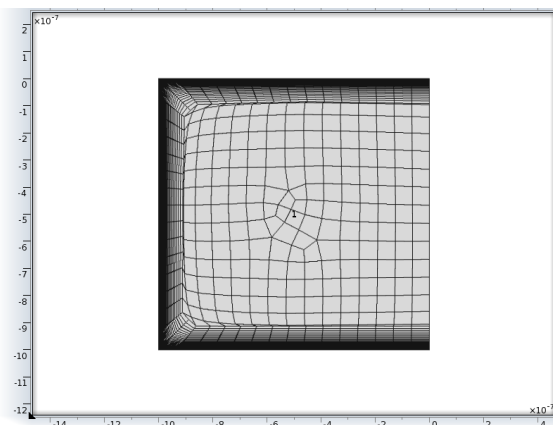


Figure 51 Mesh with 100 boundary layers. Mesh with first element size 10^{-11} m and increment factor 1.1.

In Figure 52 six surface plots are shown. In these surface plots the magnitude of the fraction is represented by the colour and the z-direction. From left to right the images respectively represent surface plots for the fraction of iron, chromium and nickel throughout the square domain. The top row shows three surface plots for a time of 10^5 seconds, which corresponds to an accumulated fluence of 0.7 dpa, since the flux is $7 \cdot 10^{-6}$ dpa/s. The bottom row shows three surface plots for a time of 10^7 seconds, which corresponds to an accumulated fluence of 70 dpa. At the three grain boundaries one gets a depletion of chromium and iron and an enrichment of nickel at both dpa levels. The lowest iron fraction at 0.7 dpa is 0.64 and occurs along the grain boundary. At 70 dpa it is 0.51 and occurs at the junction between two grain boundaries. The lowest chromium fraction at 0.7 dpa is 0.04 and occurs along the grain boundary. At 70 dpa it is 0.02 and occurs at the junction between two grain boundaries. The highest nickel fraction at 0.7 dpa is 0.32 and occurs along the grain boundary. At 70 dpa it is 0.47 and occurs at the junction between two grain boundaries. However, as shown in section 3, the actual values of fractions at the grain boundary depend on the mesh size away from the grain boundary and, hence, cannot be taken as exact. The values further away from the grain boundary and into the square domain are exact. The issue is solved when considering that calculated values have to be compared to measured values. Measurements (e.g. STEM or AES) have a spot size and performing the convolution of the beam profile with the calculated fractions yields good correspondence as shown in section 3.

In Figure 53 six images with profiles are shown. From left to right the images respectively represent profiles for the fraction of iron, chromium and nickel along cut-lines through the square domain. The top row shows three images with profiles for a time of 10^5 seconds, which corresponds to an accumulated fluence of 0.7 dpa, since the flux is $7 \cdot 10^{-6}$ dpa/s. The bottom row shows three images with profiles for a time of 10^7 seconds, which corresponds to an accumulated fluence of 70 dpa. In each image there are profiles along four cut-lines through the square domain: the first cutline is at the bottom edge of the square domain ($y=0$), the second parallel with it at 0.01 micrometer ($y=0.01\text{e-}6$), the third one at 0.1 micrometer ($y=0.1\text{e-}6$) and the fourth one at 0.5 micrometer ($y=0.5\text{e-}6$). The chromium profiles show an almost constant and large depletion at the bottom edge ($y=0$). As one moves away from the bottom edge ($y=0.01\text{e-}6$, $0.1\text{e-}6$ and $0.5\text{e-}6$) the large chromium depletion is only visible at the left grain boundary and to compensate there is a maximum in the chromium fraction close to the left grain boundary. The nickel profiles show an almost constant and large enrichment at the bottom edge ($y=0$). As one moves away from the bottom edge ($y=0.01\text{e-}6$, $0.1\text{e-}6$ and $0.5\text{e-}6$) the large nickel enrichment is only visible at the left grain boundary and to compensate there is a minimum in the nickel fraction close to the left grain boundary.

In Figure 54 three images with profiles are shown. From left to right the images respectively represent profiles for the fraction of iron, chromium and nickel along the left, vertical grain boundary. In each image there are four profiles: the first at a fluence of 0.07 dpa (10000), the second at 0.7 dpa (1e5), the third at 7 dpa (10e5) and the fourth at 70 dpa (1e7). The chromium profiles show an increasing depletion with accumulated fluence and an almost constant depletion along the vertical grain boundary, except close to the intersection with the horizontal grain boundaries. The nickel profiles show an increasing enrichment with accumulated fluence and an almost constant enrichment along the vertical grain boundary, except close to the intersection with the horizontal grain boundaries.

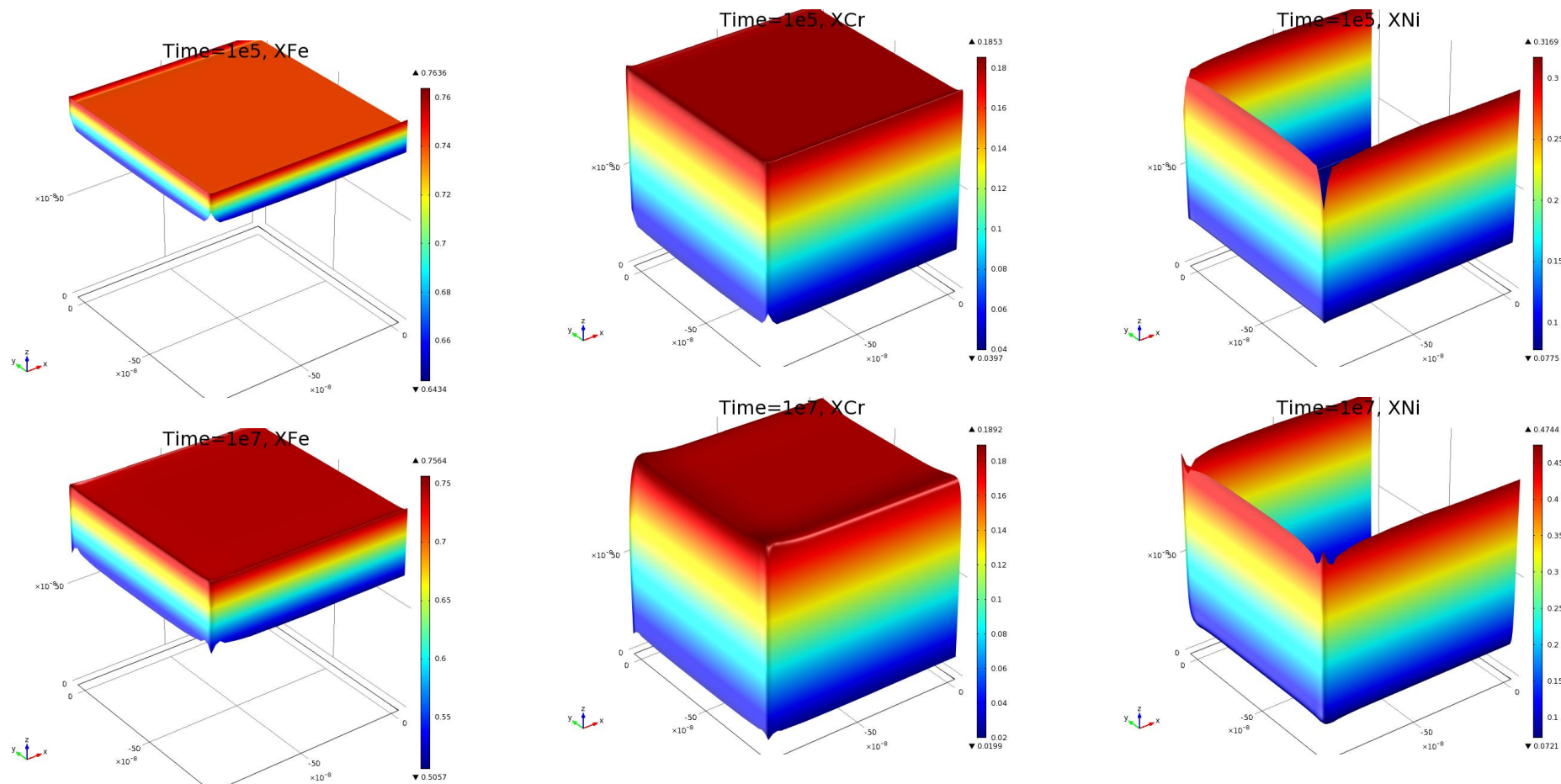


Figure 52 Surface plots for Fe (left), Cr (middle) and Ni (right) fractions at a time of 10^5 s (0.7 dpa, top) and 10^7 s (70 dpa, bottom).

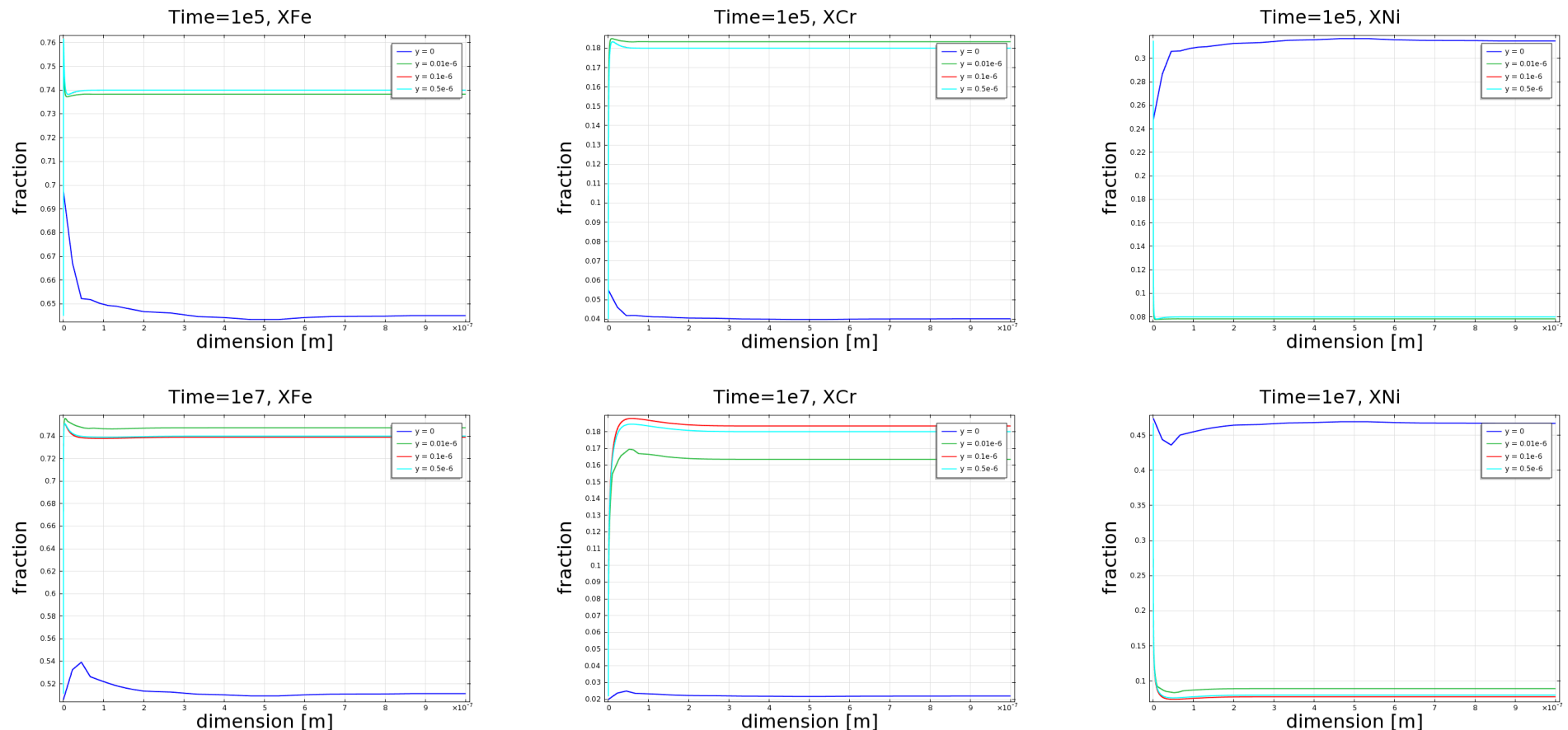


Figure 53 x-profiles for Fe (left), Cr (middle) and Ni (right) fractions at a time of 10^5 s (0.7 dpa, top) and 10^7 s (70 dpa, bottom). The values of y (0, 0.01e-6, 0.1e-6, 0.5e-6) respectively correspond to 0, 0.01, 0.1, 0.5 μm from the bottom horizontal grain boundary.

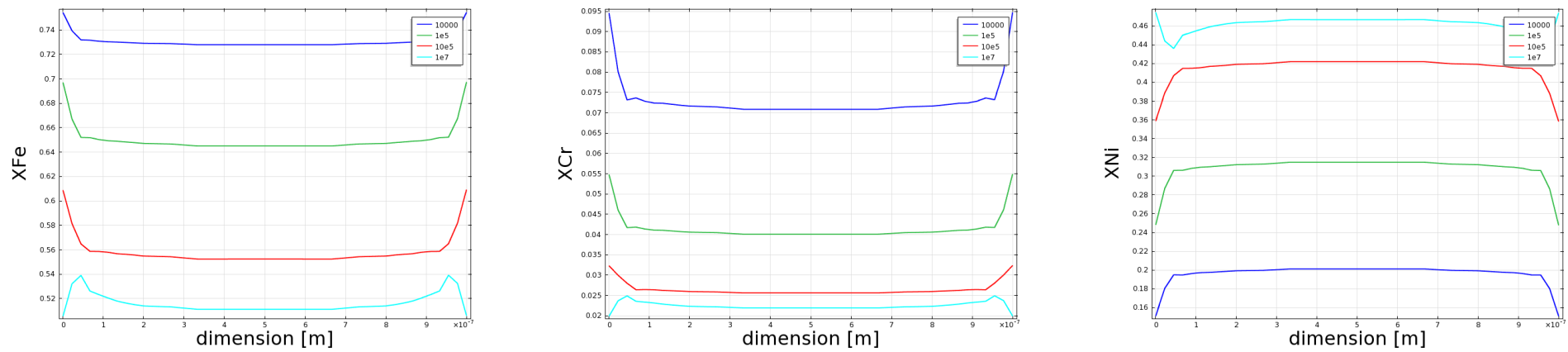


Figure 54 y-profiles for Fe (left), Cr (middle) and Ni (right) fractions at a time of 10^4 s (0.07 dpa), 10^5 s (0.7 dpa), 10^6 s (7 dpa) and 10^7 s (70 dpa) along the left vertical grain boundary.

6 Conclusions

The mathematical descriptions for radiation induced segregation in a ternary iron-chromium-nickel alloy for both the Perks and Modified Inverse Kirkendall (MIK) models have been documented.

Both models have successfully been implemented in a finite element code, Comsol Multiphysics.

Grain boundary fractions of iron, chromium and nickel can be calculated as a function of fluence.

The grain boundary fractions calculated exactly at the grain boundary are sensitive to the mesh size in the vicinity of the grain boundary. However, a convolution with sensitivity profiles for AES or STEM measurements made the calculations mesh size independent as long as the smallest element is of the order of one hundredth of the spot size.

Parametric studies have been performed in respect of flux, temperature, dislocation density and alloy composition. Grain boundary segregation increases with temperature and decreases with dislocation density and flux at a given fluence.

A comparison of measured and calculated grain boundary fraction showed that depletion of chromium and enrichment of nickel with fluence are reproduced, be it better by the Perks than by the MIK model. Nickel enrichment is very well reproduced. Chromium depletion is overestimated. A slight modification to the partial diffusion coefficients for iron, chromium and nickel might resolve this issue. The extremes in grain boundary fraction with temperature were well reproduced, be it sometimes at a slightly different temperature. The prediction are generally better for the iron-based than for the nickel-based alloys.

The results have been obtained with a reduced set of coupled partial differentials equations by eliminating the equation for iron on the basis that elemental fractions must add up to one. This made the calculations more stable.

A two-dimensional implementation has been performed and the results correspond to those of the one-dimensional implementation. This makes it feasible to couple the model to other microstructure evolution processes at the matrix-grain boundary-oxide junction.

7 Nomenclature

$C_{Fe/Cr/Ni/v/i}$	/m ³	defect/atom concentration
$X_{Fe/Cr/Ni/v/i}$	-	defect/atom fraction
N	/m ³	number of atoms unit volume
Ω	m ³	atomic volume
$J_{Fe/Cr/Ni/v/i}$	/m ² /s	defect/atom flux
$G_{v/i}$	/s	defect production rate per atom
$D_{Fe/Cr/Ni/v/i}$	m ² /s	diffusion coefficient
$d_{Fe/Cr/Ni}^{i/v}$	m ² /s	diffusivity
$v_{Fe/Cr/Ni}^v$	/s	atom-vacancy jump frequency
$v_{Fe/Cr/Ni}^i$	/s	interstitial jump frequency
$v_{Fe/Cr/Ni}^{v,0}$	/s	standard atom-vacancy jump frequency
$v_{Fe/Cr/Ni}^{i,0}$	/s	standard interstitial jump frequency
$f_{Fe/Cr/Ni}^{v/i}$	-	atom-defect correlation factor
$E_{Fe/Cr/Ni}^{v,m}$	eV	vacancy migration energy for Fe, Cr or Ni
$E^{i,m}$	eV	interstitial migration energy
λ_a^v	m	atom-vacancy jump distance
λ_a^i	m	atom-interstitial jump distance
λ	m	unit cell size
Z	-	recombination volume (# 1 st nearest neighbours)
ϕ	dpa/s	neutron flux
η	/dpa	damage efficiency (# of vacancies/interstitials generated per atom and per dpa)
ρ	/m ²	dislocation density
k_b	eV/K	Boltzmann's constant (1.38066 10 ⁻²³ J/K or 8.6174 10 ⁻⁵ eV/K)

9 Acknowledgements

The author likes to acknowledge the contribution of Roeland Juchtmans for performing the trend calculations and the comparison with literature values.

10 References

1. T.R. Allen, G.S. Was, E.A. Kenik, The effect of alloy composition on radiation-induced segregation in Fe-Cr-Ni alloys, *Journal of Nuclear Materials* 244 (1997) 278-294.
2. J.M. Perks, A.D. Marwick, C.A. English, A computer code to calculate radiation-induced segregation in concentrated ternary alloys, *AERE Report R 12121* (1986).
3. A.D. Marwick, R.C. Piller, M.E. Horton, Radiation-induced segregation in ternary alloys, *AERE Report R 10895* (1983).
4. T.R. Allen, G.S. Was, Modelling radiation-induced segregation in austenitic Fe-Cr-Ni alloys, *Acta mater.*, Vol. 46, No. 10, pp. 3679-3691, 1998.
5. R.D. Carter, D.L. Damcott, M. Atzmon, G.S. Was, Quantitative analysis of radiation-induced grain-boundary segregation measurements, *Journal of Nuclear Materials* 211 (1994) 70-84.
6. M.P. Seah, W.A. Dench, Quantitative electron Spectroscopy of Surfaces, *Surface and Interface Analysis*, VOL. 1, NO.1, (1979) 2-11.
7. T.R. Allen, J.T. Busby, G.S. Was, E.A. Kenik, On the mechanism of radiation-induced segregation in austenitic Fe-Cr-Ni alloys, *Journal of Nuclear Materials* 255 (1998) 44-58.